SYNTHESIS & CHARACTERIZATION OF GOLD NANOPARTICLES

A Report
Submitted In Partial Fulfillment of the
Requirement for the Degree of

Master of Engineering

in the Faculty of Engineering

by

Surya Prakash Rao Daliparthi

Department of Chemical Engineering
Indian Institute of Science
Bangalore
June 2006

TABLE OF CONTENTS

LIST OF TABLES

LIST OF FIGURES

Figure **Page**

Figure **Page**

Figure **Page**

APPENDIX FIGURES

Figure **Page**

dedicated to my...

Parents
(Suryanarayana & Satyavathi)

&

Brother
(Venky)

Acknowledgements

I am grateful to my Parents and family members who have been working so hard to keep me happy. I owe my success to their unconditional love and support.

I would like to thank Dr. Venugopal S for his wonderful guidance in a friendly atmosphere. I am grateful to him for all the time he spent for me. He inspired me in several ways. I am very fortunate to be his student for the past one year.

I would also like to thank Prof. Sanjeev K Gupta for his kind assistance. I would like to thank all the faculty members of Department of Chemical Engineering for the knowledge they have transferred to me.

I am thankful to Mr. Prakash for his technical support throughout my project. I am thankful to Miss Girija for her help and support. I am thankful to Mr Patil for his help regarding AFM images. I am thankful to Miss Aarthi, and Mr. Mahesh Varma for their help with UV-Visible Spectrophotometer.

I am thankful to all of my friends here, specially Bhanu, Mahesh, Subbarao, Ravi, Siva, Vijay, Gopal, Krishna, and all for entertaining me for the past two years. I am thankful to Mr Ramana and Mr Jayantha for their helpful discussions with me.

Specially, I am thankful to Mr. Hanumantha Rao for his support and encouragement towards me and I would like to thank all my B.Tech classmates who encouraged me by keep on asking the status of my work.

Finally, I would like to thank the staff of Department of Chemical Engineering, IISc for their warm interaction with me.

…….. ***Surya Prakash***

ABSTRACT

Metal nanoparticles are attractive nanoscale building blocks for research because of their size and shape dependent properties such as catalytic, electrical, optical and magnetic properties that lead to a wide variety of potential applications. This includes applications in the areas of nano-electronics, magnetic memory, catalysis, bio-medical applications, sensors, interconnects etc. Synthesis recipes for producing nanoparticles are well established in the literature. However, control of nanoparticle size distribution is still a challenge as many potential applications require monodispersed nanoparticles. Monodispersed nanoparticles can be obtained only under optimal conditions of nucleation and growth. In order to optimize and control nanoparticle manufacturing processes rapid and accurate particle size distribution measurement techniques are needed. Direct characterization techniques, such as TEM and SEM, are both labour intensive and sensitive to sample preparation techniques. In this regard dynamic light scattering(DLS) technique being rapid, accurate and reliable is one of the best techniques available. The objective of this project is to implement solution based gold nanoparticle synthesis techniques, namely, reverse micellar synthesis and to study the utility of dynamic light scattering for accurate nanoparticle size analysis. In this project, the effects of various parameters such as injection time, temperature, aging of the reagent solutions, and concentration of co-surfactant on the mean particle size of gold nanoparticles synthesized in reverse micelles are studied. Finally, a few attempts were made to model the system to capture the experimentally observed trends.

Chapter 1
INTRODUCTION

Nanometre refers to one billionth of a meter (10^{-9} m). Nanotechnology deals with the synthesis, properties and applications of nanoscale materials. Any material that has at least one of its dimensions falling within the 1-100 nm range can be classified as a nanoscale material. Although nanotechnology as a field of scientific pursuit is only about two decades old, it is now known that in the fourth-century A.D. Roman glassmakers were fabricating glasses containing metal nanoparticles. An artifact from this period called the Lycurgus cup is on display in the British Museum in London [1]. The reason for the current interest in nanotechnology is mainly driven by developments in instrumentation that are capable of measuring, and even manipulating nanoscale objects.

Metal nanoparticles are attractive candidates for research because of their size and shape dependent physical and chemical properties such as catalytic, electrical, optical and magnetic properties that can potentially give rise to a wide spectrum of devices and technologies. These include biomedical applications such as drug and gene delivery, detection of proteins, probing of DNA structure, tissue engineering [2]; catalytic applications like hydrogenation of olefins, hydrogenation of acrylonitrile, photo-induced hydrogen generation from water [3]; and opto-electronic applications like, low threshold lasers, optical fibres, sensors, transistors, magnetic memory, interconnects etc [3].

The aim of the current project is to adapt and implement solution based synthesis methods, namely reverse micelle technique [4], available in literature for producing monodisperse molecularly protected nanoparticles (MPNs) of gold and to evaluate the utility of dynamic light scattering (DLS) instrument available in our department for rapid characterization of the particle size distribution of metal nanoparticles in solution. A related objective is to develop detailed protocols and operating instructions for using the DLS instrument.

1.1 Outline

This report consists of three chapters. The first chapter is a brief introduction to nanotechnology and its applications followed by the objective of this study and an outline of the report. The second chapter discusses the various characterization techniques that are used in this work to characterize gold nanoparticles, namely dynamic light scattering (DLS) and UV-visible spectroscopy. The various nuances associated with these instruments are discussed along with experimental evidence to analyze their utility for accurate nanoparticle size analysis. It begins with an introduction to dynamic light scattering followed by characterization results for latex sphere standards and gold nanoparticle solutions. This is followed by a brief introduction to the principle of surface plasmon resonance. The third chapter begins with a literature review of different gold nanoparticle synthesis methods followed by a description of the synthesis of gold nanoparticles using reverse micelle technique along with experimental results and discussion. Some important principles of light scattering, Brownian motion, spectral analysis of DLS, operating instructions for DLS, and some preliminary characterization using atomic force microscopy (AFM) are presented in the Appendix.

1.2 References

[1] Christine M, Astruc D, "Gold nanoparticle assembly, supramolecular chemistry, quantum size related properties and applications", Chem. Rev., **104**, 293-346(2004).

[2] Panyam J, Labhasetwar V, "Biodegradable nanoparticles for drug and gene delivery to cells and tissue", Adv. Drug Deliv. Rev., **55**, 329-347(2003).

[3] Naoki T , Jetsu Y, "Bimetallic nanoparticles-novel materials for chemical and physical applications", New J. Chem., **22**, 1179-1201(1998).

[4] Li-Chiang C, "Controlled growth of gold nanoparticles in AOT/ Iso-octane/$C_{12}E_4$ mixed reverse micelles", J. of Colloid. & Interface., **239,** 334-341(2001).

Chapter 2
CHARACTERIZATION OF NANOPARTICLES

2.1 Introduction

In the context of nanoparticle characterization, the most relevant measurements are those of average size, particle size distribution, shape, and crystal structure. Many characterization techniques are available for this purpose and there are some associated advantages and disadvantages with every technique. For example DLS can provide information about mean particle size and particle size distribution by assuming spherical particles. It cannot provide any information about shape and structure of the particles. There are other techniques like Scanning electron Microscopy (SEM), Transmission Electron Microscopy (TEM) that can provide information about shape and structure also along with particle size and distribution. However, they are time consuming, expensive and sensitive to sample preparation techniques. Choosing a proper particle sizer for a specific task completely depends on the information of interest.

As described in the literature review (Chapter 3), manufacture and synthesis of nanoparticles is well established now, however manufacturing with a control of nanoparticle size distribution is still a formidable challenge. Monodispersed particles of desired size can be obtained, only under optimal conditions of nucleation and growth. In order to optimize and control nanoparticle manufacturing process for producing monodisperse particles, rapid and accurate particle size distribution measurement techniques are needed. In comparison to direct characterization techniques such as TEM, AFM, and SEM, dynamic light scattering (DLS) is attractive for measurement of slightly polydisperse nanoparticle samples as it is a rapid and reliable characterization technique that relies on ensemble averaging. Another characterization tool for metal nanoparticles is UV-Visible Spectroscopy. It relies on surface plasmon resonance phenomenon. In the following sections principles of DLS

and UV-Visible spectroscopy are discussed and their ability for measuring nanoscale particles verified using latex and gold nanoparticles.

2.2 Dynamic Light Scattering

Dynamic light scattering is a technique with which the dynamical properties of a system can be studied by analyzing the temporal variations in the scattered light intensity. For example in colloidal systems, colloidal particles are always moving in the solution due to Brownian motion. As a result the 3-D configuration of the particles in the solution varies with time. When such a system is irradiated by a laser beam, every particle within the irradiated volume gives rise to scattered light or electromagnetic waves. The scattered waves can constructively or destructively interfere depending on their pathlength difference that in turn depends upon the configuration of the colloidal particles. This configuration varies with time and thus results in the temporal variation of the total signal strength measured by the detector. The crux of the technique lies in obtaining the dynamical information (in this case it is the diffusion coefficient of the colloidal particles) by analyzing the temporal fluctuations of the scattered light intensity. Earlier, spectrum analyzers were used for this purpose. Of late, they have been replaced by digital auto-correlators because of which this technique is also sometimes referred to as photon correlation spectroscopy (PCS). Dynamic light scattering is also known as quasi-elastic light scattering (QELS) because of the fact that the doppler frequency shift in the scattered light is much smaller than the actual frequency of the incident light [1]. It is an ensemble averaging technique (EA), i.e. the signal from the sample is a sum of the contributions from all particles in solution. DLS gives rapid measurements albeit at lower resolution when compared to TEM and AFM.

Dynamic Light Scattering is based on the principles of Brownian motion and light scattering. These principles are elaborated further in appendix A1 and appendix A2. Briefly, when a monochromatic, coherent light beam is incident on very small particles in a colloidal solution, the light beam will scatter in all directions. If the particles are very small compared to the wavelength of the light, then the intensity of

the scattered light is uniform in all directions (Rayleigh scatterers). For bigger particles, scattered light intensity depends on the angle of scattering (Mie scattering). The scattered light intensity is measured with the help of a detector and it is proportional to the square of the scattered electric field amplitude, which is a function of the distance between the particle and the detector [2]. In the sample solution, the particles are under constant Brownian motion, so the distance between the particle and detector fluctuates around a mean distance and hence the electric field amplitude and scattered light intensity also fluctuate accordingly [3]. These temporal fluctuations in the scattered light intensity can be correlated to derive a self diffusion coefficient. This self diffusion coefficient is related to the hydrodynamic diameter through Stokes- Einstein equation as described in appendix A2.

2.2.1 DLS Experimental Set-up

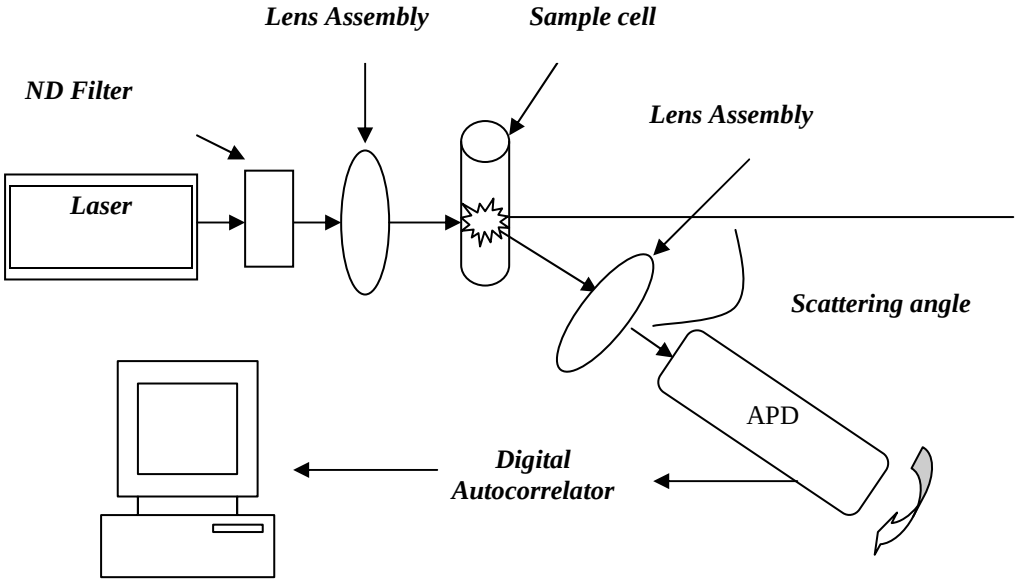

Figure 2.1: Schematic of a DLS experimental set-up.

The schematic of a DLS setup is shown in figure 2.1. It consists of a laser that produces a monochromatic, coherent beam, which passes through a neutral density filter (ND filter) and lens assembly before it impinges on the sample cell assembly. The neutral density filter helps to vary the power of the laser beam. The steering lens

assembly focuses the laser beam onto the central part of the sample cell such that scattering volume will be sufficiently far away from the wall. This ensures unrestricted Brownian motion in all directions. The sample cell assembly consists of a cylindrical sample holder placed in a vat which is filled with decalin (vat liquid). Decalin, an index matching liquid with sample cell, prevents scattered radiation from the vat and sample cell surfaces and other stray radiation reaching the detector. In the sample, the laser light gets scattered in all directions and a small portion of the scattered light from the sample passes through another lens and interference filter before it reaches the detector, typically a photo multiplier tube (PMT) or an avalanche photo detector (APD). The interference filter prevents stray background radiation reaching the detector [4]. The time variation of the intensity of the detected signal is processed by a digital autocorrelator, to derive the translational diffusion coefficient that is then processed to yield particle size. Some important aspects regarding stability of laser and alignment of the instrument are presented in appendix A3. A detailed instruction manual to operate DLS is presented in appendix A4.

2.2.2 Processing of Raw Information

The output, n(t), of the DLS instrument is the variation of scattered light intensity with time (number of photons observed by the detector per unit time). An example of such an output is shown in figure 2.2. Based on this information, the second order autocorrelating function (ACF) which is defined as the average of the product of scattered light intensity at any time t and the intensity at a time t delayed by time τ, can be calculated as [3],

$$C(\tau) = \langle n(t)n(t-\tau)\rangle \tag{2.1}$$

where,

n(t) → number of photons counted over a sampling interval $\Delta\tau$ centered at time t.

n(t-τ)→ number of photons counted over $\Delta\tau$ but delayed in time by τ.

The physical significance of this auto-correlating function is that for very small delay times the positions of the particle and the scattered light intensity are highly correlated and hence the numerical magnitude for this function would be large. For higher delay times, the particle positions are not well correlated as a result the magnitude of the correlating function decreases as shown in the figure 2.3 [1].

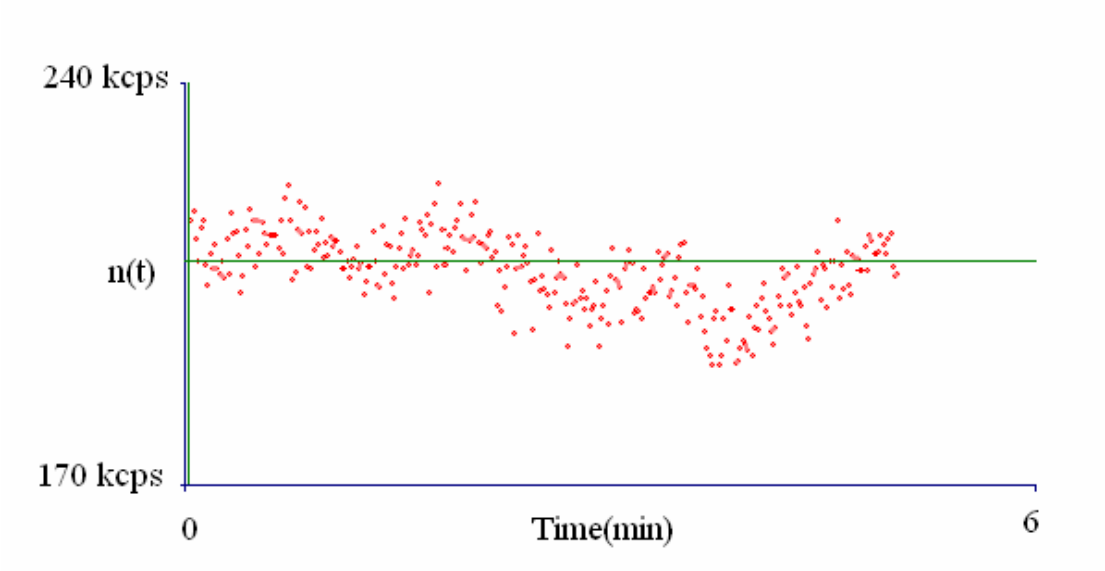

Figure 2.2: A typical Snapshot from DLS software of the temporal variation of number of photons(kilo counts per second, kcps) measured by DLS instrument.

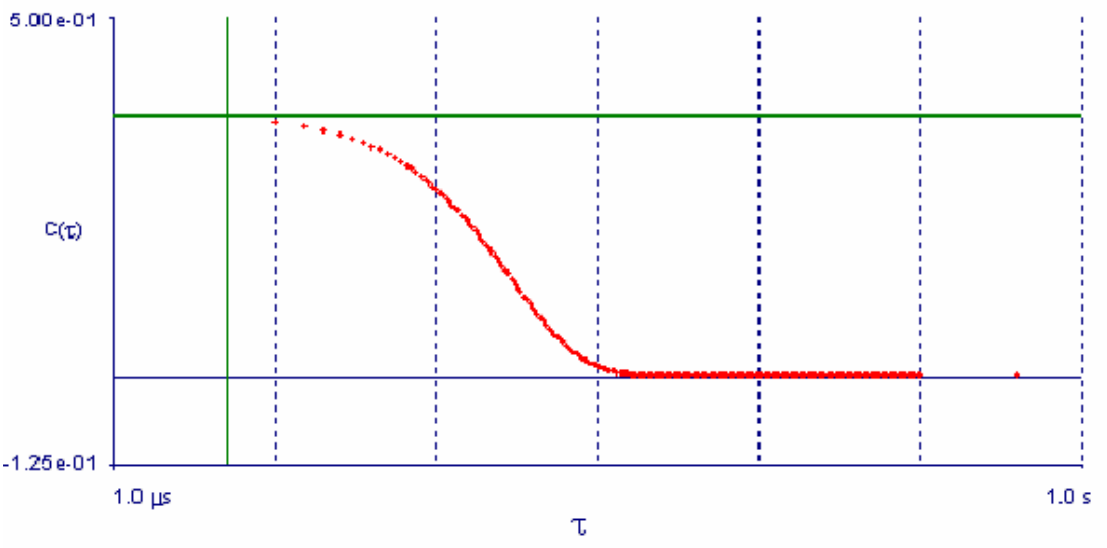

Figure 2.3: An example snapshot of the variation of correlating function($1/sec^2$) with delay time(sec). This data is for 90 nm standard latex particles.

For dilute, rigid, spherical particles the ACF is given by [3],

$$C(\tau) = B\left\{1 + f\left|g^1(\tau)\right|^2\right\} \tag{2.2}$$

where,

B is base line constant
f is instrumental constant

When the sample is monodispersed, the first order autocorrelating function, $g^1(\tau)$, is given by

$$\left|g^1(\tau)\right| = \exp\left[-\Gamma\tau\right] \tag{2.3}$$

where,

Γ is line width, which is the half width at half height of the frequency broadened distribution of the scattered light. This frequency broadening is briefly discussed in appendix A5.

Equations 2.2 and 2.3, which are based on scattering theory, along with the experimentally determined ACF are used to obtain the parameter Γ. This parameter is related to the translational self diffusion coefficient D_T by,

$$\Gamma = D_T q^2 \tag{2.4}$$

where, 'q' is the amplitude of the scattering wave vector,

$$q = 4\pi n_o \sin(\theta/2)/\lambda_o \tag{2.5}$$

where,

n_0 → refractive index of the liquid

λ_0 → wavelength of the laser in vacuum

θ → scattering angle.

The equation which relates the diffusion coefficient to the hydrodynamic diameter is called Stokes-Einstein equation [1], which gives the effective diameter for the sample under observation as,

$$D_T = k_B T / (3\pi\eta d_H) \tag{2.6}$$

where,

k_B → Boltzmann constant

η → viscosity of the liquid

T → absolute temperature

d_H → hydrodynamic diameter

For a polydisperse sample, the first order autocorrelating function is a weighted sum over the exponential decays from each of the contributing particles. So it is given by,

$$\left|g^1(\tau)\right| = \int_0^\infty G(\Gamma)\exp(-\Gamma\tau)d\Gamma \tag{2.7}$$

where, G(Γ) is the relative intensity corresponding to a particle of line width Γ.

The method of cumulants is used to calculate particle size distribution (PSD) from measured ACF. In this method the exponential term is expanded and each and every term is integrated term by term. This results in a form such as,

$$\ln\left|g^1(\tau)\right| = -\bar{\Gamma}\tau + \frac{\mu_2\tau^2}{2!} - \frac{\mu_3\tau^3}{3!} + \ldots \tag{2.8}$$

where,

$\bar{\Gamma}$ → average line width of all the particles from which an average particle size can be calculated.

$\mu_2/\ \bar{\Gamma}^2$ → polydispersity. For monodispersed particles it approaches zero.

Experimentally, the observed $g^1(\tau)$ is fit with the form of equation 2.8 to obtain parameters Γ and μ_2. From these parameters, the effective diameter and polydispersity are calculated as described above . But, these calculations do not yield complete description of the shape of the particle size distribution. The complete particle size distribution can be obtained by using optional commercial software packages like NNLS [5] and CONTIN[6] that rely on scattering theory to predict the variation of intensity with diameter.

2.2.3 Characterization Results & Discussion

In this section characterization results of standard latex particles supplied by Duke Scientific Corporation are presented. To gain a clear insight on the nuances of characterization with DLS, 90 nm and 20 nm monodispersed polystyrene latex particles are investigated. A mixture of 90 nm and 20 nm latex particle samples is also characterized using DLS to evaluate the performance of DLS for bimodal distributions and polydispersed samples.

2.2.3.1 Sample Preparation

Sample preparation consists of three steps namely, solvent purification, suspension preparation and sample cell cleaning. Sample cells were put in a concentrated (98%$_v$) sulphuric acid bath for about 10 hours and then rinsed with tap water. Then, they were gently cleaned with detergent to avoid scratches on the cell surface. The sample cells are then rinsed with tap water, followed by distilled water and finally dried in an oven. De-ionized water from Millipore unit was directly used as the solvent and a 10 mM KCl solution was prepared with this de-ionized water.

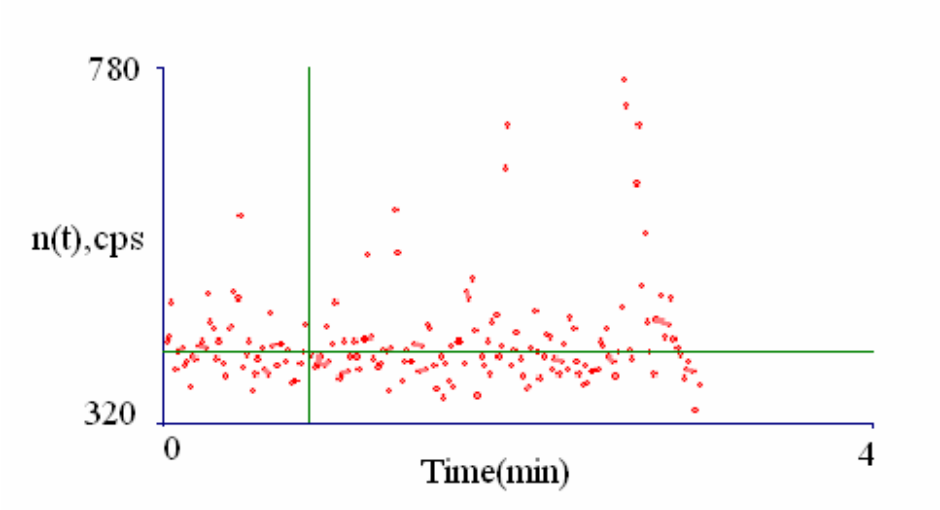

Figure 2.4: A typical DLS histogram showing count rate history(counts per second, cps as a function of time) for de-ionized water from Millipore unit.

The quality of de-ionized water from Millipore unit was verified by DLS and was found to be useful for scattering experiments. The average count rate for DI water is 425 cps (typical dark count rate for the detector is 370 cps, dark count is defined as number of photons observed by the detector due to thermionic emission) and the count rate history for a period of 4 minutes, shown in figure 2.4, does not show large deviations. A suspension of latex particles was prepared by adding latex particles supplied by Duke Scientific Corporation (CAT NO. 3090A) to 10 mM KCl solution. Syringe filters of 200 nm pore size were used to remove dust from the suspension. This suspension was then transferred to a clean sample cell, which is then placed inside the DLS sample cell assembly for measurements.

2.2.3.2 90 nm Latex Sphere Standards

A suspension of 90nm latex particles was prepared as described in the sample preparation section (5 drops of 90 nm particle solution in 20 ml of 10 mM KCl solution) and characterized by DLS. The average particle diameter (APD) and polydispersity(PD) values are in good agreement with the specifications given by Duke Scientific Corporation (92±3.7 nm APD and 0.025 PD) As DLS cannot provide the complete PSD, it was calculated using two commercial software algorithms CONTIN and NNLS.

Serial Number	Scattering Angle (degrees)	APD in nm (DLS)	Polydisp-ersity (DLS)	APD in nm (NNLS)	APD in nm (CONTIN)
1	30	94.2	0.054	89.2	88.6
2	60	92.7	0.047	115.8	86.1
3	90	92.9	0.046	88.8	88.6
4	120	94.8	0.020	89.7	90.8
5	150	94.8	0.025	95.8	92.7

Table 2.1: The values of average particle diameter (APD) and Polydispersity at various angles of detection for polymer latex nanosphere standards (Specified size 92±3.7 nm).

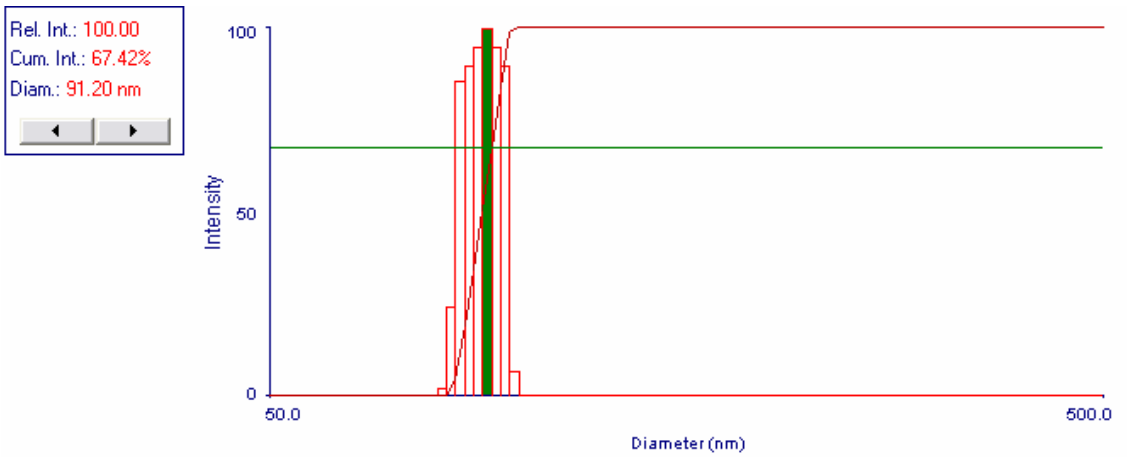

Figure 2.5: A snapshot from Brookhaven DLS software of a typical histogram and cumulative distribution function of particle size distribution using CONTIN with relative scattered light intensity as weight (90 nm latex particles at 90 degree scattering angle).

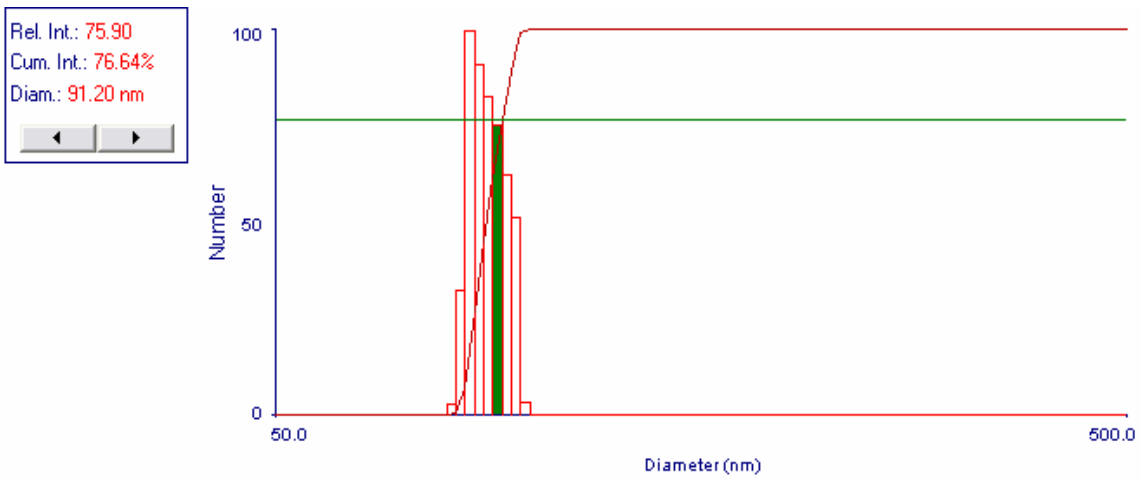

Figure 2.6: A snapshot from Brookhaven DLS software of a typical histogram and cumulative distribution function of particle size distribution using CONTIN with number of particles as weight (90 nm latex particles at 90 degree scattering angle).

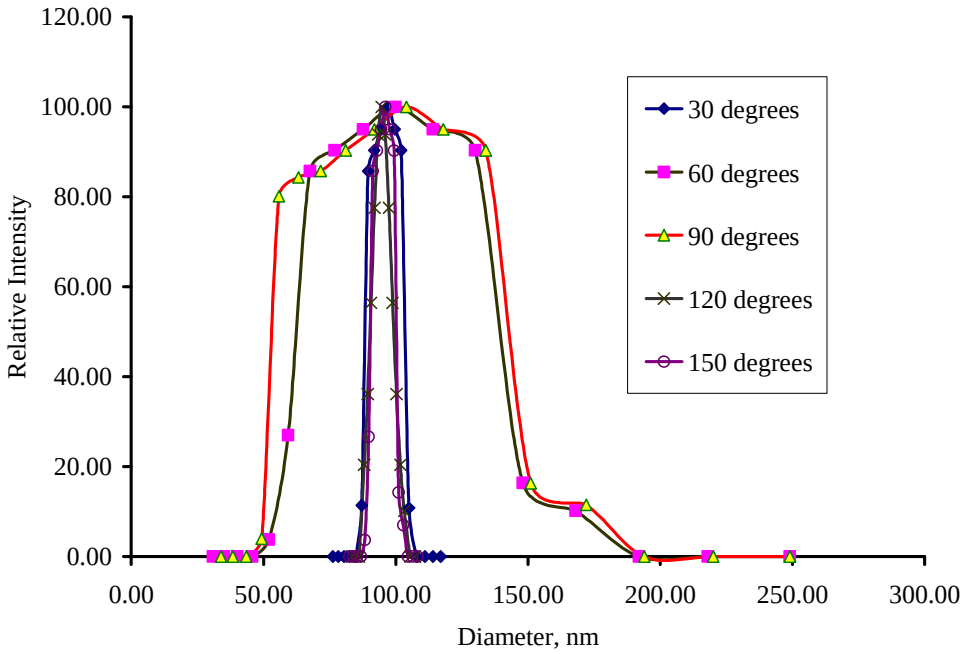

Figure 2.7: Particle size distribution of 90 nm latex sphere standards at different scattering angles (CONTIN)

Figure 2.5 shows the particle size distribution determined by CONTIN algorithm with relative intensity on the ordinate. The total scattered light intensity given by each class of particles is scaled with the maximum total scattered light intensity and termed as relative intensity. The variation of average particle diameter and polydispersity with scattering angle is shown in the table 2.1 for 90 nm latex particles. From the table, it is clear that as the detector is moving from forward scattering angles (< 90) to backward scattering angles polydispersity values are improving. The reason for this observation is that dust particles scatter more in the forward direction when compared to backward directions. Figure 2.6 shows the particle size distribution, for the same measurement shown in figure 2.5, obtained using CONTIN algorithm with number of particles as weight on the ordinate. Figure 2.7, shows the particle size distribution of 90 nm standard latex spheres at different scattering angles namely; 30, 60, 90, 120, and 150 degree. The shape of PSD is observed to be uncorrelated with scattering angle.

2.2.3.3 20 nm Latex Sphere Standards

A suspension of 20 nm particles was prepared similar to the procedure for 90 nm particles (6-8 drops of 20 nm particles in 20 ml of 10 mM KCl solution) and measured with DLS. The effective diameter and polydispersity values for 20 nm latex sample at different scattering angles are reported in table 2.2. From this table, it is clear that the effective diameter is in good agreement with the specifications given by Duke Scientific Corporation (21±1.5) and the polydispersity values are within acceptable range (<0.05), except at a scattering angle of 150^{o}.

Serial Number	Scattering Angle (degrees)	APD in nm (DLS)	Polydispersity (DLS)	APD in nm (NNLS)	APD in nm (CONTIN)
1	30	20.5	0.069	21.1	24.7
2	60	20.1	0.072	21.3	23.1
3	90	20.4	0.051	19.6	18.9
4	120	21.3	0.032	20.9	19.1
5	150	20.8	0.105	22.5	22.9

Table 2.2: The values of average particle diameter (APD) and Polydispersity at various angles of detection for polymer latex nanosphere standards (Specified size 21±1.5 nm.).

In principle, the value at 150 degree must be better when compared to forward scattering angles such as 30 and 60, as the effect of dust is more pronounced at forward scattering angles. This anomaly may be due to a dusty vat surface at 150 deg or due to the presence of scratches. The shape of the particle size distribution was evaluated with commercial software (CONTIN) and the results are shown for different scattering angles in figure 2.8. The shape of PSD is observed to be uncorrelated with scattering angle.

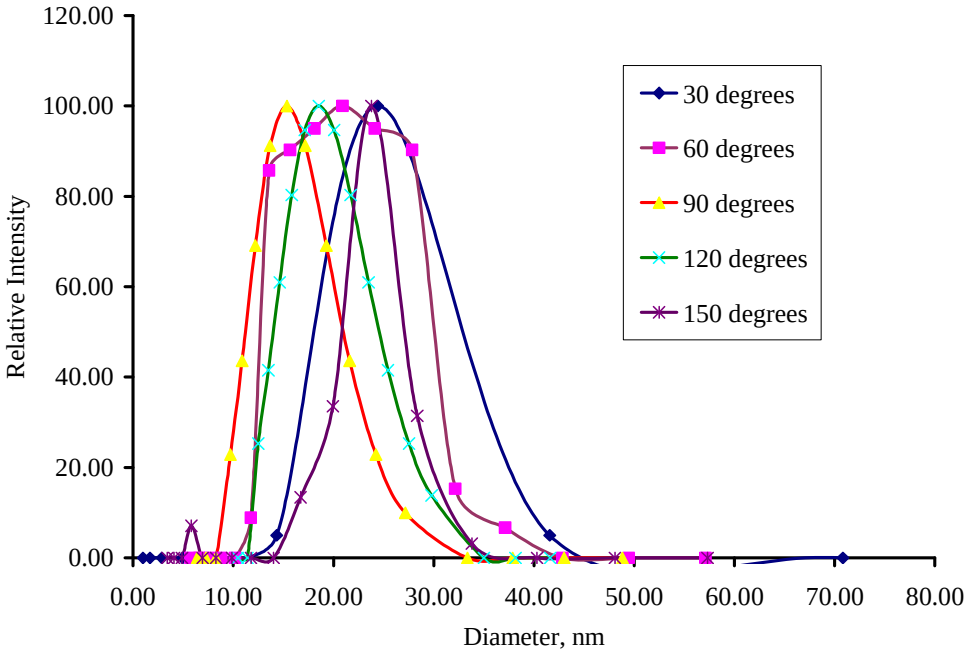

Figure 2.8: Particle size distribution of 20 nm latex sphere standards at different scattering angles(CONTIN).

2.2.3.4 Mixtures of 90 nm & 20 nm Latex Spheres

A suspension containing both 90 nm and 20 nm latex standard spheres was prepared to verify whether bimodal distributions could be measured with DLS. This sample was prepared as follows. First, 50 ml solutions of 10 mM KCl were prepared in two conical flasks (each 50 ml). Then, a 90 nm latex particle sample was prepared by adding 5 drops of 90 nm particles to the first conical flask. A 20 nm latex particle sample was prepared by adding 10 drops of 20 nm particles to the second conical flask**.** A mixture of 90 nm and 20 nm latex particle sample was prepared by adding 1 drop of suspension from the first conical flask (90 nm particle suspension) to 10 ml of suspension from the second flask (20 nm particle suspension) in a sample cell. This sample was characterized with DLS and the result is shown in the figures 2.9.

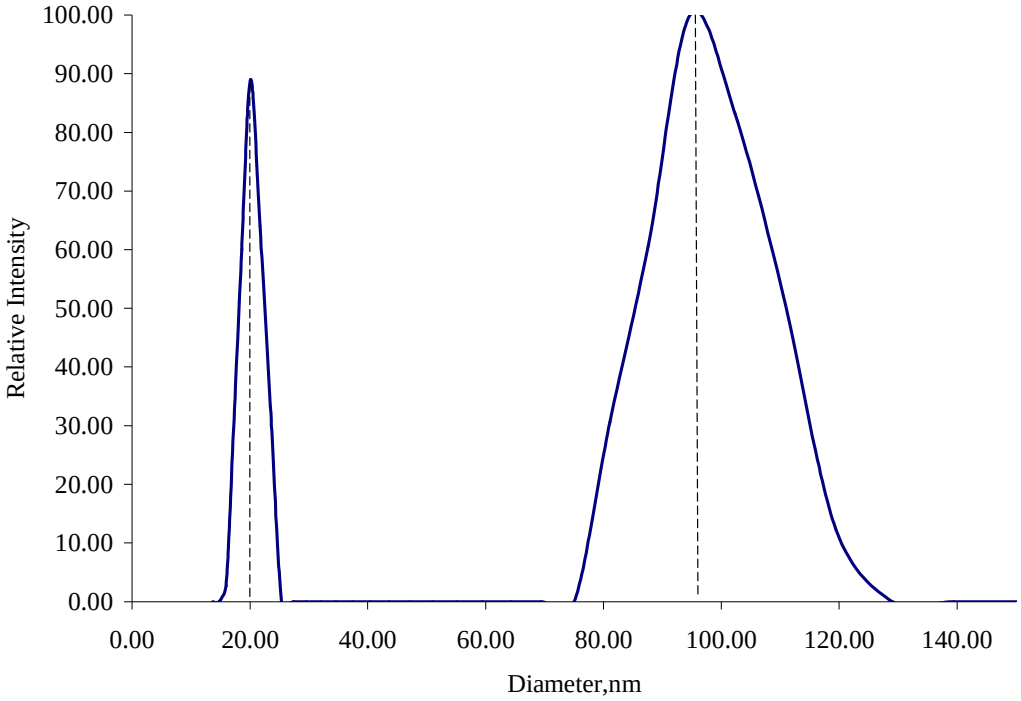

Figure 2.9: A typical histogram of particle size distribution (weighted by relative intensity) for a mixture of 90 nm and 20 nm latex standard spheres showing two peaks at 20 nm and 94 nm (NNLS).

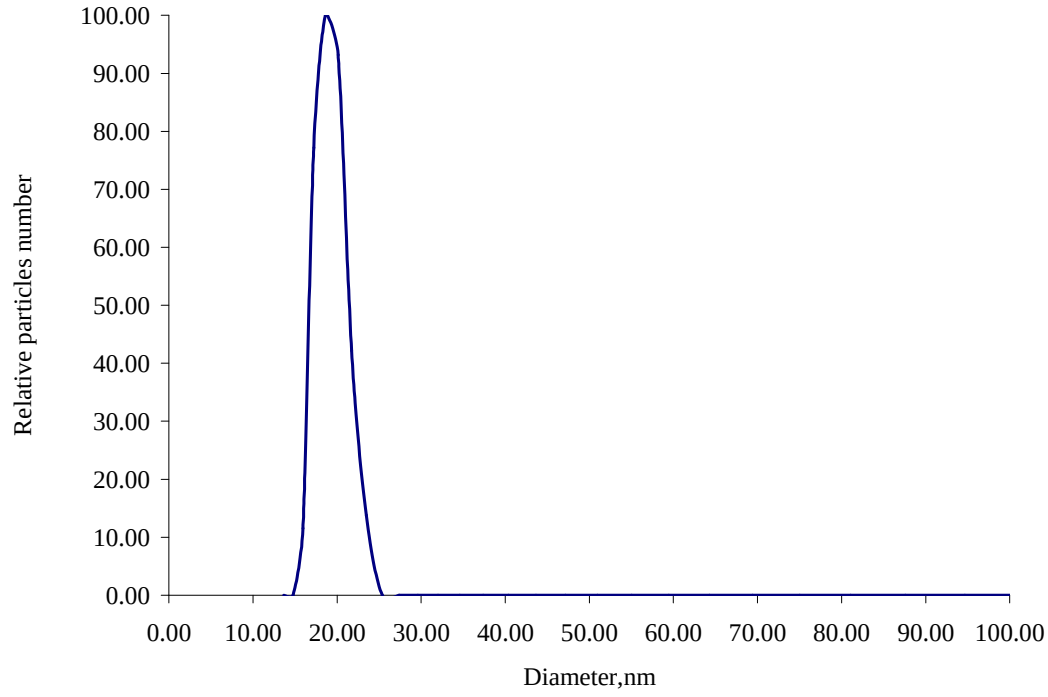

Figure 2.10: A typical histogram of particle size distribution for a mixture of 90 nm and 20 nm latex sphere standards with relative number density as the weight on the ordinate(NNLS).

Based on the sample preparation conditions, the concentration of 90 nm particles is expected to be negligible when compared to that of 20 nm particles, However, the result plotted as shown in fig. 2.9 is misleading at first sight. The reason being that scattered light intensity has a strong dependence on particle size ($I \alpha d^6$) as explained in Appendix 2.1. A more accurate picture can be obtained by plotting the number of particles against diameter as shown in figure 2.10. This plot shows that there is hardly any 90 nm particles.

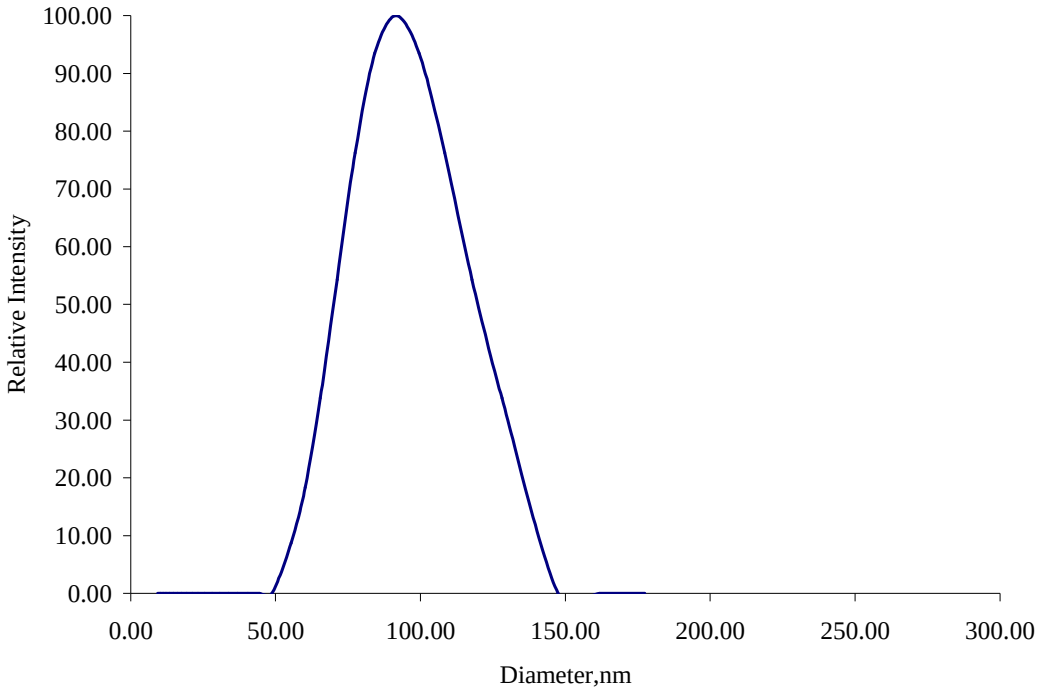

Figure 2.11: A typical histogram that shows the particle size distribution (weighted by relative intensity) for a 1:1 mixture of 90 nm and 20 nm particles[NNLS].

As a part of the exercise to verify whether DLS could be used for bimodal distributions, half of the sample cell was filled with 90 nm particles and the remaining half with 20 nm particles. The results are shown in the figure 2.11. It shows that the scattering signal from smaller particles is overwhelmed by those of the larger particles. These results indicate that DLS plots must be carefully scrutinized and PSD should be plotted with both relative intensity and calculated number density as weights, if bimodal distributions are expected. Also, the ability to resolve a bimodal distribution is severely constrained, whenever the size difference of the two peaks is

large or when the concentration of the larger particles is comparable with that of the smaller ones.

2.2.4 Critical Issues in DLS Characterization

In this section some important issues regarding characterization are briefly presented with experimental observations. These include dispersion of particles in the solvent, multiple scattering from the sample, statistical fluctuations, colloidal particle interactions, first delay time (first observation time window set to capture the motion of particles) etc. Dynamic light scattering is based on Brownian motion, so the particles should be well dispersed in the solvent. To ensure better dispersion of the particles, the selection of solvent and dispersing agent should be done such that particles do not agglomerate and sediment and also they should not form any physical or chemical bonds with the solvent or dispersing agent [1].

2.2.4.1 Effect of First Delay Time

To evaluate the second order auto-correlating function from the count rate history, which is nothing but a temporal variation of the scattered light intensity that is recorded by the detector, the detected signal is correlated with a delayed version of the same signal. The period of delay is denoted as delay time and a plot of the second order correlation as a function of delay time is used to obtain PSD information The first delay time is a characteristic parameter as the remaining delay time values depend on it. This delay time can be interpreted as the observation time window used to capture information about particles with similar time scales for diffusion. Thus at smaller delay times, information about the movement of smaller particles dominate, while at larger delay times the contribution from larger particles dominate the temporal variation of the scattered signal intensity. Table 2.3 and figure 2.12 present the effect of first delay time on the calculated average particle size for a reverse micellar solution of AOT/water in isooctane.

It is seen that as the first delay time increases the calculated size also increases and that there is an improved agreement among the sizes predicted by different algorithms. The reason being that the reverse micellar system consists of many individual surfactant molecules, unswollen reverse micelles along with reverse micelles of interest. These surfactant molecules and unswollen micelles can diffuse.

Serial Number	First delay time (µs)	Diameter (DLS, nm)	Diameter (NNLS, nm)	Diameter (CONTIN, nm)
1	0.1	0.7	3.9	1.2
2	1	2.4	4.6	5.2
3	2	4.3	4.6	5.8
4	5	5.6	6.4	6.4
5	10	Not stable	Not stable	Not stable

Table 2.3: This table shows the effect of first delay time on the calculated APD for a reverse micellar solution of AOT/water in isooctane (DLS, NNLS, CONTIN).

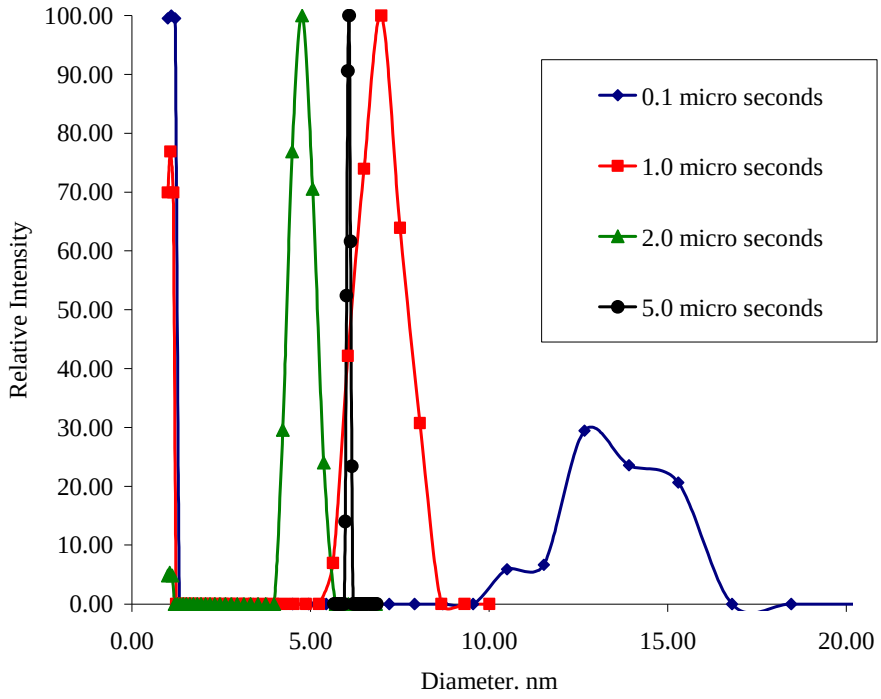

Figure 2.12: The effect of first delay time on calculated PSD for a reverse micellar solution of AOT/water/isooctane (CONTIN).

rapidly when compared to the swollen reverse micelles. When the first delay time is very small, it captures information about surfactant molecules and unswollen micelles also. As first delay time increases, the relative contribution from the smaller surfactant molecules and unswollen micelles decreases leading to an increase in the calculated size (i.e it approaches the swollen reverse micelle size of 5.6 nm [7]).

2.2.4.2 Effect of Inter-particle Interactions

An important requirement in dynamic light scattering is that “particles must scatter independently” [1]. There are two situations in which this requirement is violated. They occur due to the presence of inter-particle interactions and multiple scattering. The multiple scattering effect sets an upper limit for the concentration of particles in the colloidal solution and will be discussed in the following section. The inter-particle interactions are Van der Waals attraction, hard sphere repulsion due to electron cloud overlapping, electrostatic interactions, and steric interactions. The diffusion coefficient is altered due to the effect of inter-particle interactions. Repulsive interactions like hard sphere repulsion, electrostatic repulsion, and steric repulsion results in higher diffusion coefficient whereas the Van der Waals attraction results in lower diffusion coefficient when compared to the true Brownian diffusion coefficient. This is shown in the figure 2.13. The cooperative diffusion coefficient in the presence of interaction forces is plotted against particle concentration in the same figure to show the effect of inter-particle interactions on the diffusion coefficient. The effect of interactions is directly proportional to the average inter-particle distance and hence it depends on the particle concentration [1]. Hence, the particle concentration should be chosen to minimize such interaction effects. For the same volume concentration, the effect of inter-particle interactions is more pronounced for smaller particles when compared to that for bigger particles, as the average inter particle distance is smaller in the case of smaller particles [1].

This effect of inter-particle interactions (PI) on diffusion coefficient can be explained as follows. The driving force for diffusion which is thermal kinetic energy of a single particle in infinite medium gets altered by the particle interactions [1]. In addition, as

the particle concentration increases, it results in increased friction for the particles to move due to hydrodynamic interactions. While characterizing gold nanoparticles synthesized by the reverse micellar route, the effect of inter-particle interactions on mean particle size is observed to be very significant. These results are presented for sample DSP30 in table 2.4.

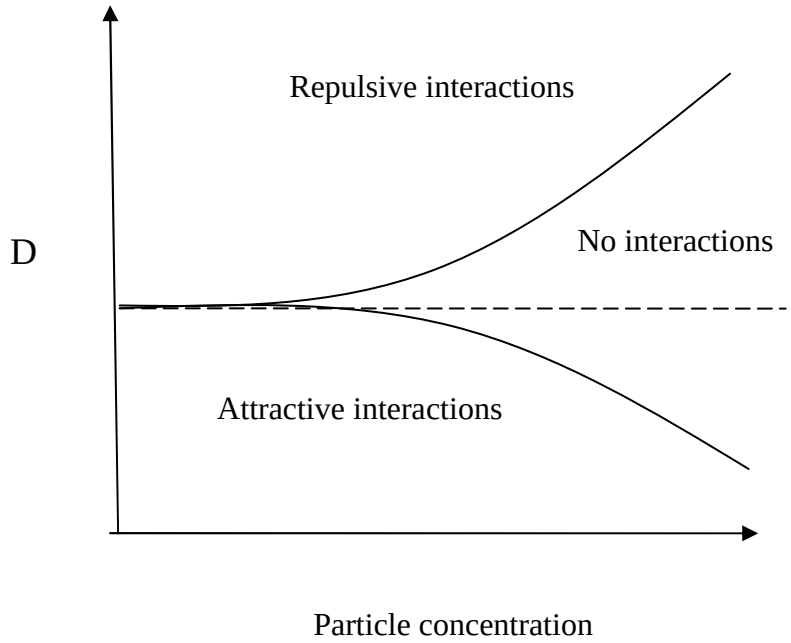

Figure 2.13: The effect of inter-particle interactions on diffusion coefficient [1].

Serial Number	Relative Concentration(%)	Diameter (DLS, nm)	Signal strength (kcps)	Comment
1	100	30.7	303.4	-
2	85	27.4	272	PI
3	75	22.4	226	PI
4	67	28	180	Aggregation
5	60	36	194	Aggregation

Table 2.4: The effect of particle interactions and aggregation on mean particle size (Sample DSP30).

The concentrations of the sample are approximate and these concentrations are relative to original sample. From the table it is seen that initially the signal strength decreases with dilution as expected. The particle size is also seen to decrease with dilution indicating the presence of attractive interactions. At 67 % relative concentration there is jump in particle size indicating the onset of aggregation. The mean particle size corresponding to 75% concentration is chosen as the best estimate.

2.2.4.3 Effect of Multiple Scattering

Multiple scattering refers to the fact that scattered radiation from one particle is further scattered by another particle before it reaches the detector. Due to multiple scattering, the signal strength becomes weaker as the multiply scattered waves destructively interfere with the singly scattered wave. This is another important factor that has to be taken into account during measurements of gold nanoparticle solutions. As a result of multiple scattering, the second order auto-correlating function decays more rapidly and as result it under-estimates the particle size [1]. When compared to the smaller particles, the multiple scattering effects are more pronounced in the case of bigger particles due to the strong dependency of scattered light intensity with the diameter [1]. The effect of multiple scattering and particle interactions is shown in table 2.5. When the relative concentration of a gold nanoparticle reverse micellar solution (sample DSP29) is reduced from 100 % to 75 %, the signal strength increases indicating the presence of multiple scattering. As discussed earlier, the presence of multiple scattering should show an increase in particle size with dilution. On the contrary, it is seen to be decreasing indicating the competing presence of inter-particle interactions. There is a small window of concentration (around 50% relative concentration), for this particular sample, at which both multiple scattering(MS) and particle interaction(PI) effects are minimized and it is taken to be the best estimate of the actual particle size.

Serial Number	Relative Concentration(%)	Diameter (DLS, nm)	Signal strength (kcps)	Comment
1	100	32.9	177	-
2	75	28.2	196	MS & PI
3	60	26.7	210	MS & PI
4	50	**25.7**	219	MS & PI
5	43	26.7	217	No MS
6	27	33.4	232	Aggregation
7	27	41.6	260	Aggregation

Table 2.5: The effect of multiple scattering and inter particle interactions on the mean particle size (sample DSP29).

In this example, the effect of particle interaction could not be eliminated due to the onset of aggregation with further dilution. The onset of aggregation can be identified by the rapid increase, with dilution, of the particle size along with a sudden increase of the signal strength. It can also be identified by observing an increase of the signal strength from the count rate history as shown in the figure 2.14.

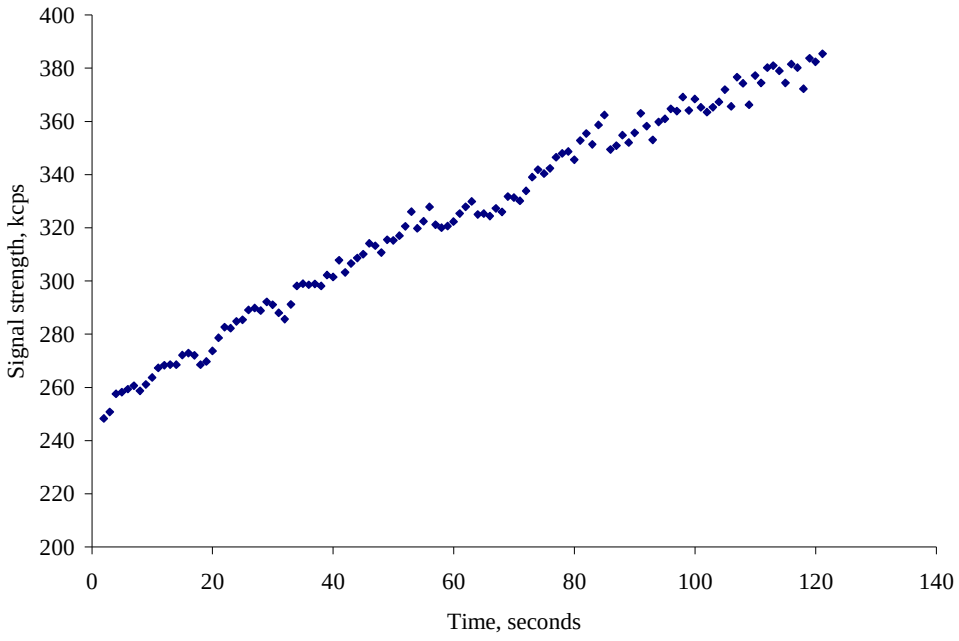

Figure 2.14: A snapshot of the count rate history that shows an increase of the signal strength due to the effect of particle aggregation for the sample DSP29.

2.2.4.4 Number Fluctuations

In dynamic light scattering, it is assumed that the temporal variation in the scattered light intensity arises solely due to the particle movement within the scattering volume while neglecting the particle movement into and out of the scattering volume. But in practice, a few particles will always move in and out of the scattering volume leading to temporal fluctuations in the total number of particles within the scattering volume. At very low concentrations, these number fluctuations can be significant and result in additional fluctuations of the scattered light intensity that is observed by the detector. Usually the time scale for these fluctuations is smaller than the time scale of motion of particles and this results in an overestimation of particle size. In order to minimise this effect, the scattering volume should contain at least a few thousand particles and this sets another lower limit on the concentration of the solution[1].

2.2.5 Summary

The various aspects regarding the characterization of nanoscale colloidal solutions using DLS are summarized below.

- DLS is based on the principle of light scattering and Brownian motion. The PSD is estimated using Stokes-Einstein relationship and Mie/Rayleigh scattering.

- Multiple angle scattering measurements can be used to provide a better estimate of PSD in the case of polydisperse samples. However, the deconvolution of data requires complex optimization routines.

- In the case of bimodal distributions, plots of intensity and number distribution should be used in conjunction to verify the presence and estimate the relative amounts of smaller and larger particles.

- The first delay time is a critical parameter that needs to be optimized to obtain information about species of interest in a reverse micellar solution.

- In the case of nanoparticle laden reverse micellar solutions, the effects of multiple scattering, inter-particle interactions and number fluctuations constrain the concentration range in which an accurate estimate of the nanoparticle size can be obtained. This implies that the concentration variation of signal strength and calculated average particle size should be monitored carefully to eliminate spurious results.

2.3 UV-Visible Spectroscopy – Surface Plasmon Resonance

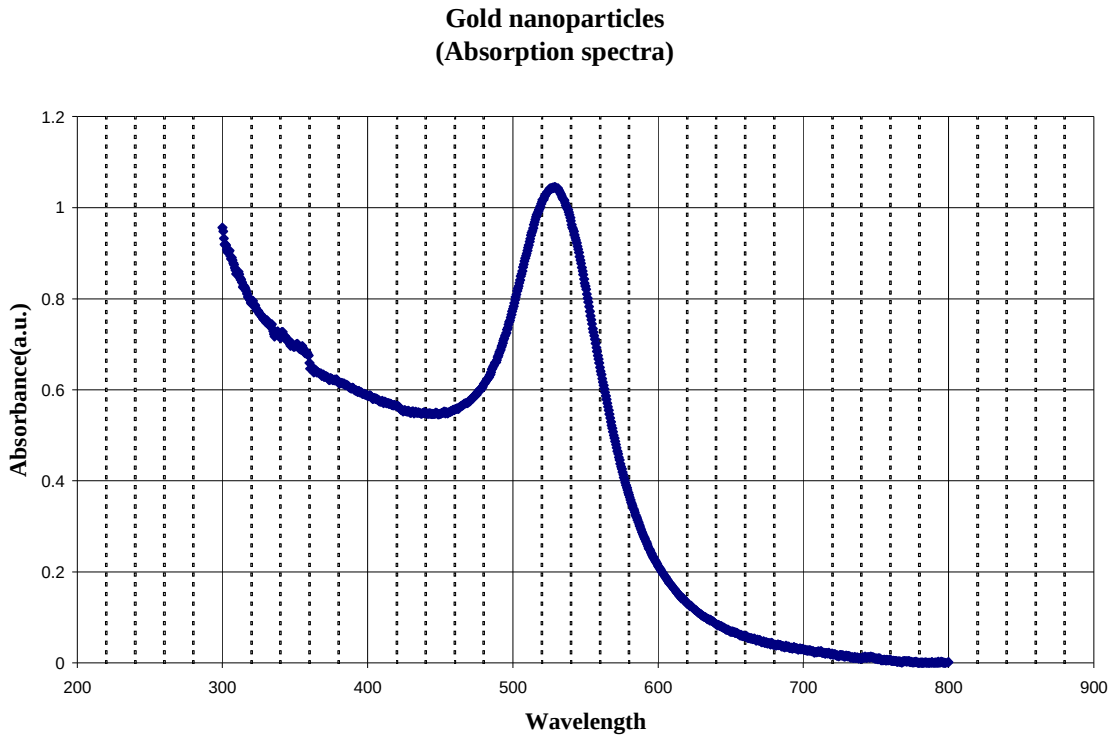

Figure 2.15: UV-Visible Absorbance spectra of gold nanoparticles (35 nm) prepared by reverse micelle technique.

A Surface Plasmon is a collective excitation of the electrons within a metal nanoparticle. When a metal nanoparticle is exposed to a light beam, the free electrons within the particle respond to the electro-magnetic field of the light beam and are separated with respect to the heavy metal ions. This polarization results in a charge

difference near the boundary of the nanoparticle that acts as a restoring force for the electron cloud leading to oscillations. The frequency of oscillation depends on the magnitude of the net charge difference, which in turn depends on the number of free electrons in the conduction band that is a function of the nanoparticle size. Hence, the frequency of oscillation of free electron cloud is a function of nanoparticle dimensions. When a light beam impinges on the nanoparticle with the same frequency at which the electron clouds naturally oscillate within the particle, it results in a resonance leading to energy absorption. This phenomenon is called surface plasmon resonance. This surface plasmon resonance results in maximum absorbance in the surface plasmon absorption spectrum at the wavelength at which resonance occurs. Thus, the wavelength at which maximum absorption occurs, can serve as a tool for the characterization of gold nanoparticles [8]. Figure 2.16 shows a typical UV-visible absorption spectrum of gold nanoparticle solution synthesized by reverse micelle technique. The peak at 530 nm wavelength indicates smaller nanoparticles.

2.4 Atomic Force Microscope (AFM)

The previous characterization techniques such as dynamic light scattering, UV-Visible spectroscopy, are called as non-imaging characterization techniques. Atomic force microscopy is an imaging characterization technique with which the particles on a flat substrate like mica or silicon wafer can be imaged. These images can be processed with the help of special image processing software to obtain the particle size. Atomic force microscopy is an instrument that works based on intermolecular forces. When two molecules are far apart there will be no interaction, as they are approaching together first they experience Van der Waals attraction force. As they are coming very closer they experience repulsion forces due to overlapping of electron clouds. In AFM, a very small tip is fixed at the end of a cantilever to measure the intermolecular forces between the tip and the sample. While a tip is scanning over the surface, the magnitude of intermolecular force changes with the position of the tip on the 2D sample plane, due to the change in the distance between the tip and the sample. This change in force with the position is further processed to yield the topography. A

few attempts were made to characterize nanoparticles on mica and silicon wafer. But the particle size could not be resolved from that image due to some problems regarding the image. Those images are presented in the appendix A6.

2.5 References

[1] Finsy R, “Particle sizing by quasi elastic light scattering”, Adv. in Colloid and Interfac. Sci., **52**, 79-143(1994).

[2] Bruce B W, “Modern methods of particle size analysis”, Wiley-Interscience, New York, 1984, 5, page 163.

[3] Pecora, R, “Dynamic light scattering measurement of nanometer particles in liquids”, Journal of Nanoparticle Research, **2**, 123-131(2000).

[4] Bruce B W, “Operating instructions manual”, BI200SMMAN, Ver. 2.5(1993).

[5] Morrision I D, Grabowski E F, “Improved techniques for particle size determination by quasi elastic light scattering”, Langmuir, **1,** 496-501(1985).

[6] Provencher S W, “A constrained regularization method for inverting data represented by linear algebraic or integral equations”, Comp. Phys. Commn., **27,** 213-227(1982).

[7] Fletcher P D I, Howe A M, Robinson B H, “ The kinetics of solubilisate exchange between water droplets of a water-in-oil microemulsion”, J. Chem. Soc.,Faraday Trans., 1, **83**, 985-1006(1987).

[8] Santhanam V, PhD Thesis, Purdue University (2002).

Chapter 3
METAL NANOPARTICLES

3.1 Introduction

Nanotechnology deals with nanoscale building blocks like nanoparticles, carbon nanotubes and nanowires/nanorods, which have potential applications in a wide variety of disciplines ranging from catalysis to biology. Among these nanoscale building blocks, nanoparticles are attractive because of their size dependent properties and on account of the availability of relatively mature synthesis strategies. Any solid particle in the size range of 1-100 nm can be considered as a nanoparticle. Nanoparticles are mainly classified into three categories namely; organic particles (PS, PMMA), inorganic particles (metals, semiconductors and oxides), and bio-molecules (proteins, DNA, viruses).

Several physico-chemical properties of nanoparticles, such as melting point, specific heat, crystal structure, chemical reactivity, electrical conductivity and optical properties vary as the size of the particle varies in the nanoscale regime. For example melting point decreases with decrease in particle size, and hence smaller particles can be annealed at lower temperatures to form continuous films that have potential applications in plastic electronics [1]. The chemical reactivity increases as the particle size decreases as the crystal structure changes with entity size. The crystal structure changes from simple cubic to polyhedral leading to more corners and edges (higher energy states because of low coordination number) and hence reactivity increases. As the particle size decreases, specific surface area increases. So nanoparticles can be used in catalysis to obtain higher yields [2]. Magnetic properties like coercive force which is the force required to invert the internal magnetic filed is also size dependent. Based on this property magnetic nanoparticles can be used to fabricate high density magnetic memory devices [3]. Optical properties such as surface plasmon resonance, are a function of particle size and its environment. So these nanoparticles can be placed in different environments and based on the surface plasmon resonance peak,

that environment can be detected. This property makes them useful in bio-sensor applications like cancer detection and detection of proteins in a body etc. [4]. These nanoparticles can also be used in drug delivery, gene delivery and cancer therapy [5]. Another promising application of nanoparticles is in the area of developing efficient solar cell arrays [6].

This report deals with the synthesis and characterization of gold nanoparticles. Among the many materials available, gold is particularly interesting because it is a noble metal and it does not readily form oxides even at the nanoscale. The high electrical conductivity of gold makes it an ideal material for electronic components. Gold nanoparticles can be used to fabricate single electron transistors, interconnects, chemo-resistive sensors etc. [7].

3.2 Gold Nanoparticle Synthesis – Literature Review

Colloidal gold nanoparticles were first prepared in solution by Michael Faraday. After that Turkevich and Stevenson succeeded in preparing spherical gold nanoparticles of 20 nm and made an extensive study on nucleation and growth [8]. Presently, there are several techniques available for synthesizing nanoparticles. These can be broadly classified into gas phase aerosol techniques and solution phase techniques. Chemical synthesis methods are very attractive as they do not need sophisticated equipment and have the capability of producing monodispersed spherical gold particles as well as anisotropic particles. A few of these methods are described below.

3.2.1 Gas phase synthesis

The critical requirement for synthesizing nanoparticles with narrow size distribution in the gas phase is to initiate a homogeneous nucleation event followed by a slow growth regime while preventing particle aggregation. To initiate homogeneous nucleation, the gas phase needs to be supersaturated with the metal atoms. There are several ways of attaining the supersaturated condition (physical and chemical) depending upon which, the methods under gas phase synthesis are classified. The

potential advantages of gas phase synthesis are ability to synthesize small particles with control over mean particle size, ability to produce pure metal particles, ability to produce mixed metal particles even though they are immiscible at room temperature, and ability to anneal them thermally. The disadvantage of this method is that it needs sophisticated equipment.

The most common technique is denoted as inert gas condensation. In this method (physical atomization), metal atoms are evaporated from a crucible or from a series of crucibles in an oven to form a vapor source and these vapors are then entrained by an inert gas and flow into a nucleating chamber where it mixes with another stream of inert gas at room temperature to induce homogeneous nucleation. This mixture is then expanded into a growth chamber held at a lower pressure, where growth of the nuclei by addition of free atoms takes place [9]. The mean particle size is controlled by varying the conditions in the crucible and the flow rate of inert gas. The particles can also be thermally annealed by passing them through a tube furnace. These particles are scrubbed from the gaseous phase by contacting with small droplets (mist) of organic solvent containing surfactant molecules and collected as a stable colloidal suspension. The experimental set up of one such gas condensation reactor is shown in figure 3.1.

Some other physical atomization techniques include pulsed laser ablation [10], spark discharge generation [11] and ion sputtering [11]. In the laser ablation method, a pulsed laser is used to vaporize the material and form the vapor source. Laser ablation technique will be useful when the material that is to be vaporized has low thermal evaporation rate. In spark discharge generation method, the material that is to be evaporated is taken in the form of metal rods and used as electrodes. A potential difference is applied between the electrodes in an inert gas environment. When this potential difference reaches the break down voltage of the gas present between the two electrodes, a spark occurs and causes a small amount of metal to evaporate.. Ion sputtering is a method of vaporizing the material by bombarding it with a beam of atoms or ions of an inert gas to form the vapor source.

An alternative method for achieving supersaturation condition is to induce homogeneous nucleation by chemical reaction in the inert gas phase [11]. In this method, the reactants are mixed with an inert gas and this mixture is then passed through a hot-wall reactor which is maintained under proper conditions of nucleation and growth. The reactant source can be a solid or liquid or gas, but they are delivered to the reactor as a vapor.

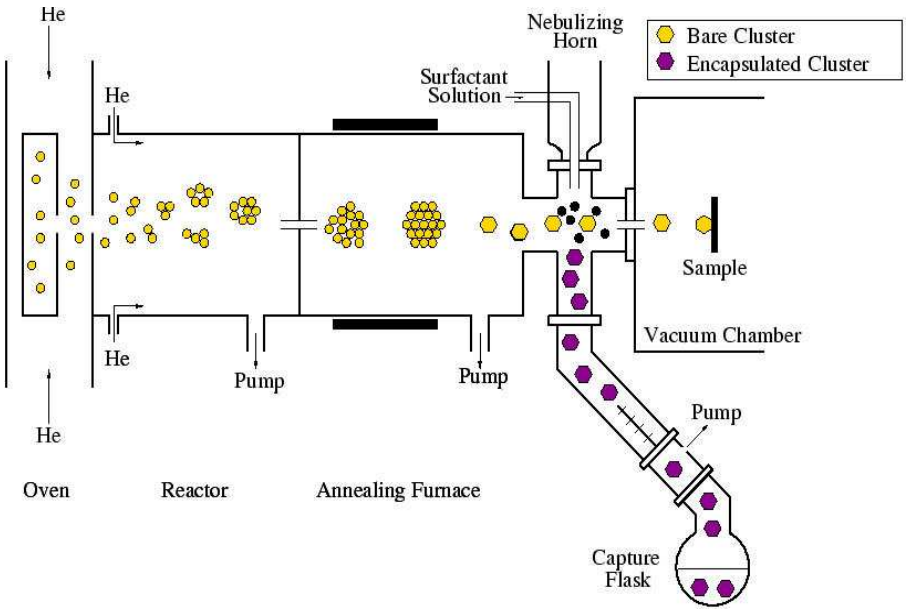

Figure 3.1: Schematic of Multiple Expansion Cluster Source [MECS], a typical gas phase metal nanoparticle synthesis reactor [1]

3.2.2 Solution phase synthesis

In this method, gold salts are reduced to give nanoparticles in solution in the presence of appropriate capping and reducing agents. The main advantage of these methods is their simplicity. The well established methods reported in the literature for producing monodispersed gold nanoparticles are namely, Turkevich [8] method and Brust [12] method. The method of Slot and Geuze [13] is a modified version of that proposed by Turkevich. Apart from these, there are other methods like sonochemical [14], and electrochemical [15] techniques. Some of them are described below.

3.2.2.1 Turkevich method

Turkevich et al. synthesized gold nanoparticles using several reducing agents and characterized their nucleation and growth rates [8]. They found that the law governing the growth in size of a nanoparticle is exponentially dependent on reaction time. The average size and the character of the particle size distribution curve are determined by the amount of gold, the nucleation process, and the growth law. They showed that the use of sodium citrate as a reducing agent method produces spherical nanoparticles. The synthesis method is simple and a typical procedure is as follows. 95 ml of chloroauric acid solution (containing 5 mg of Au) is heated to the boiling point and 5ml of 1% sodium citrate solution is added to this boiling solution with good mechanical stirring until the color becomes deep wine red. Transmission electron microscopy (TEM) images show that this procedure gives reproducible spherical particles in the size range of 20±1.5 nm. The salient features of the study were; at higher temperature, the time required to complete the reaction is small, both the mean particle size and the root mean square deviation decrease slightly with decreasing temperature, and the average particle size increases with decreasing citrate concentration up to a threshold concentration beyond which particles formed are no longer stable in solution. Slot et al. [13] modified this procedure by using tannic acid in addition to citrate and were able to vary the particle size in the range of 2-20 nm depending on tannic acid concentration . They found that the pH of the solution affects average particle diameter to a great extent. Addition of tannic acid results in a lower pH. To produce particles of size less than 4.5 nm, it is required to maintain the pH at 7.5-8 by adding carbonate solution. At lower pH or temperature, larger particles are produced and higher pH or temperature results in polydispersed particles. To produce monodispersed small particles the optimum conditions are $60^{\circ}C$ and a pH of 7.5-8[13]. Giersig and Mulvaney [16] extended this procedure to produce molecularly protected nanoparticles soluble in organic solvents. They used alkanethiol dissolved in tetrahydrofuran to displace the citrate anions and encapsulate the nanoparticle with alkanethiol. The encapsulated nanoparticles were then extracted into the organic phase by using cyclohexane. Then by adding a polar solvent to cyclohexane these particles were precipitated, washed, dried, and re-suspended in a non-polar solvent.

The particles can then be size separated by using a polar/non-polar solvent mixture in conjunction with centrifugation [16].

3.2.2.2 Brust method

The Brust method is a two phase reduction of gold salt by sodium borohydrate in the presence of alkanethiol to produce molecularly protected nanoparticles. The two phases are toluene and water. An aqueous solution of hydrogen tetrachloroaurate is mixed with a solution of tetraoctylammonium bromide in toluene. This mixture is stirred properly to ensure better contact between the phases so that all gold salt ions get transferred from aqueous phase to organic phase. Dodecanethiol is then added to the organic phase after phase separation. To this solution, aqueous solution of sodium borohydrate is slowly added with vigorous stirring. After the completion of reaction, ethanol is added to remove excess thiol. Then the precipitate is separated, dried, washed and re-suspended in a non-polar solvent like toluene, hexane or chloroform. This method is well suited to produce nanoparticles less than 5nm [1]. The general reaction frame work is schematically shown in figure 3.2.

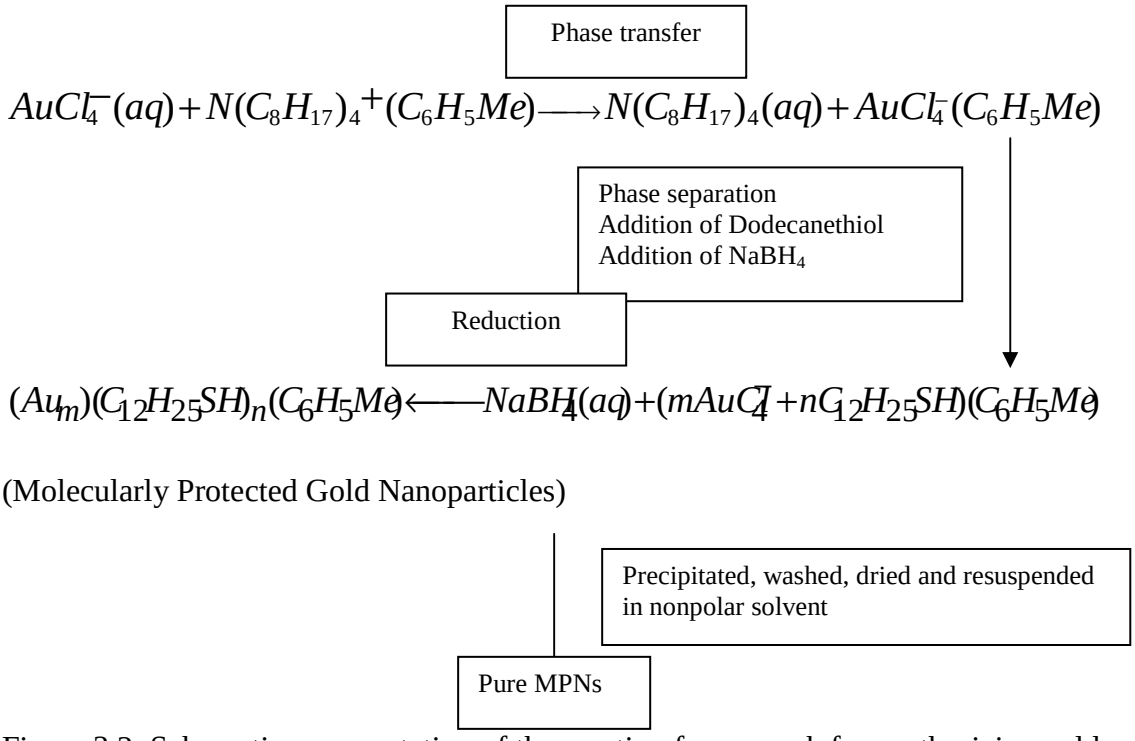

Figure 3.2: Schematic representation of the reaction frame work for synthesizing gold nanoparticles by Brust method.

3.2.2.3 Sonochemical synthesis

In sonochemical synthesis [14], reduction is induced by ultrasonic irradiation which results in the formation, growth and implosive collapse of bubbles in a liquid. During the collapse of such bubbles, local hot spots are created with temperatures up to about 5000 K, which provides an unusual method for the decomposition of water molecules into hydrogen and hydroxyl radicals that can reduce noble metal ions. When dilute alcoholic solutions of gold salt are subjected to ultrasonic irradiation, water decomposes to give H and OH radicals. These radicals react with alcohol to give a reducing radical. This reducing radical reacts with gold salt and gives Au atoms which aggregate to give gold nanoparticles. Here, alcohol also acts as a radical scavenger. The proposed reaction mechanism is given in figure 3.3. In the absence of alcohol only a very small quantity of nanoparticles is formed. A modified version utilizes citric acid (formed from sodium citrate) as the reducing radical instead of alcohol. The corresponding reactions are also shown in the same figure 3.3 [17].

$$H_2O \longrightarrow H\bullet + \bullet OH \quad (1)$$

$$H\bullet[\bullet OH] + (CH_3)_2CHOH \longrightarrow (CH_3)_2C\bullet OH + H_2[H_2O]$$
$$3(CH_3)_2C\bullet OH + AuCl_4^- \longrightarrow Au^\circ + 3(CH_3)_2CO + 4Cl^- + 3H^+ \quad (2)$$
or
$$(CH_2COOH)_2C_2H_2O_3 + H\bullet[\bullet OH] \longrightarrow \bullet C(CH_2COOH)_2COOH + H_2O[H_2O_2]$$
$$3(\bullet C(CH_2COOH)_2COOH) + Au^{3+} \longrightarrow Au^\circ + 3(+C(CH_2COOH)_2COOH) \quad (3)$$

$$nAu^\circ \longrightarrow (Au)_n$$
$$(Au)_n + (Au)_m \longrightarrow (Au)_{m+n} \quad (4)$$

Figure 3.3: Schematic representation of reaction frame work for sonochemical (1, 2, 4) and modified sonochemical (1, 3, 4) techniques.

3.3 Reverse Micellar Synthesis of Gold nanoparticles

As described in the previous section, several methods are available to synthesize gold nanoparticles. The techniques which can provide particles with well-defined size, shape and surface properties are more interesting, as many of the potential applications in various fields of science and technology require monodispersed

particles. In order to synthesize well defined monodispersed particles, control over the nucleation and growth process is essential. It is observed from the literature that synthesis of nanoparticles in reverse micelles is more attractive as this method offers good control over the particle size and shape. The reason for good control in reverse micellar synthesis is that the nucleation and growth of nanoparticles are restricted to the mesoscale level. It is for this reason that this project aims at studying the various factors that can affect nanoparticles synthesized by the reverse micellar technique[18].

3.3.1 Reverse Micelles – An Introduction

Reverse micelles are self-assembled structures of surfactant molecules that consist of polar droplets of small sizes encased by a spherical surfactant monolayer. Surfactants are long chain molecules with a hydrophilic head and a hydrophobic tail. When a surfactant

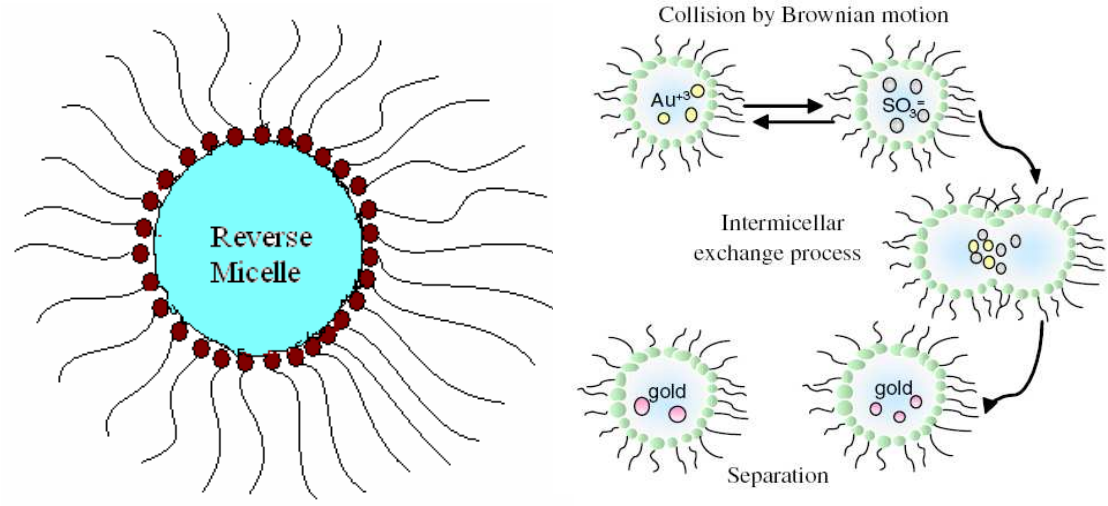

(a) (b)

Figure 3.4: Schematic of (a) reverse micelle, (b) intermicellar exchange process [19]

is added to a polar solvent at a concentration above its critical micellar concentration (CMC), it forms a self assembled structure called a micelle. In a micelle, the hydrophobic tail lies inside and the hydrophilic head is exposed to the polar solvent. A reverse micelle forms when the solvent is non-polar When the surfactant is added to a two phase system of oil and water, where water is dispersed in oil in the form of

small droplets, the surfactant molecules accumulate on the interface in such a way that hydrophobic tails get exposed to oil and form a swollen reverse micelle. This reverse micellar solution is thermodynamically stable and optically transparent. These reverse micelles can exchange their contents during collisions (intermicellar exchange process) between droplets undergoing Brownian motion, and hence can act as a nanoreactor. Figure 3.4 illustrates this intermicellar exchange process [19]. There are four important factors that control this process. They are water to surfactant molar ratio, molar ratio of reducing agent to gold chloride, the injection time of reducing agent into the gold chloride solution and temperature. From a review of the literature [19], it is found that the molar ratio of water to surfactant determines the size of micellar droplet and this is believed to control the particle size. The second factor, the molar ratio of reducing agent to gold chloride determines the number density of nuclei, as higher the ratio of reducing agent to gold chloride higher will be the number of nuclei produced and this leads to the formation of smaller particles. The third factor, injection time is expected to offer good control over the particles size as the extent of nucleation and extent of growth can be controlled by controlling the injection time. The last factor is the reaction temperature, which can offer control over the rate of intermicellar exchange processes. The elucidation of the effects of injection time and temperature on the synthesis of gold nanoparticles in reverse micelles is the main objective of this study.

3.3.2 Experimental Protocol — Materials

The materials used in this study are hydrogen tetrachloro aurate tri-hydrate as gold source ($HAuCl_4.3H_2O$, from Sigma and Kemie Labs), hydrazine hydrate as reducing agent (N_2H_5OH from Sigma), sodium bis-(-2-ethylhexyl) sulfosuccinate (AOT) as surfactant (Sigma-Aldrich Co.), tetra ethylene glycol dodecyl ether (Brij) as a non-ionic surfactant (Sigma-Aldrich Co.), and the organic solvent used was HPLC grade iso-octane (Rankem Co.). De-ionized water from Millipore unit was used in preparing all the aqueous solutions and for rinsing of the cleaned glassware. The additional details regarding chemicals are presented in the appendix A7.

3.3.3 Experimental Protocol — Synthesis of Reverse Micelles

AOT is the most commonly used surfactant in micro-emulsions, as its wedge shaped molecular structure offers high water solubility with a well defined aqueous-organic interface. Tetra-ethylene glycol dodecyl ether (Brij) is the co-surfactant and isooctane is the solvent for this system. The concentrations of various chemicals are based on the work of Chiang [18]. Typically, aqueous solution of gold chloride (0.05 M) and hydrazine hydrate (0.125 M) were prepared by adding 0.1969 grams of gold chloride tri-hydrate to 10 mL of de-ionized water, and 304 µL of hydrazine hydrate to 50 mL of de-ionized water respectively. Mixed reverse micellar solution of AOT/Brij30/Iso-octane was prepared with 0.1 M AOT and 0.2 M Brij30 in HPLC grade iso-octane solvent. Mixed reverse micellar solution of both the reactants were prepared by adding 1 ml of aqueous solution of the reactant of interest to 23.15 ml of mixed reverse micellar solution of AOT/Brij30/Iso-octane, while maintaining a water to surfactant ratio(W_o) of 8.

3.3.3.1 Characterization of Reverse Micelles

It is clear from the literature review that the micellar droplet size determines the final particle size. In order to characterize these reverse micelles dynamic light scattering (using a BI–200 SM DLS Instrument) measurements are utilized. For the unswollen micelles, 0.1 M solution of AOT in iso-octane was used as the sample. The solution viscosity is calculated from the following correlation [20].

$$\eta_r = 1 + 2.5\phi \tag{3.1}$$

where, η_r = relative viscosity(ratio of solution viscosity to water viscosity)

ϕ = volume fraction of spherical droplets in solution.

The size distribution of unswollen reverse micelles is shown in figure 3.5. The average reverse micelle size is 2.3 nm, which gives a radius of 1.15 nm, which corresponds well with the length of an AOT surfactant molecule [20].

Swollen reverse micelles are prepared by adding 1 ml of aqueous solution of gold chloride (or) hydrazine hydrate to 23.15 ml of 0.1 M AOT and 0.1 M of Brij 30 in iso-octane. The results are in good agreement with those predicted by the following correlation [21]

$$\text{hydrodynamic radius (nm)} = 0.175\ W_o + 1.5 \qquad (3.2)$$

The diameter of the reverse micelles predicted by this correlation is 5.8 nm (for W_o of 8), where as the diameter obtained by DLS is 5.63 ± 0.05 nm (based on 3 repetitive measurements). The size distribution of the reverse micelles is shown in figure 3.6.

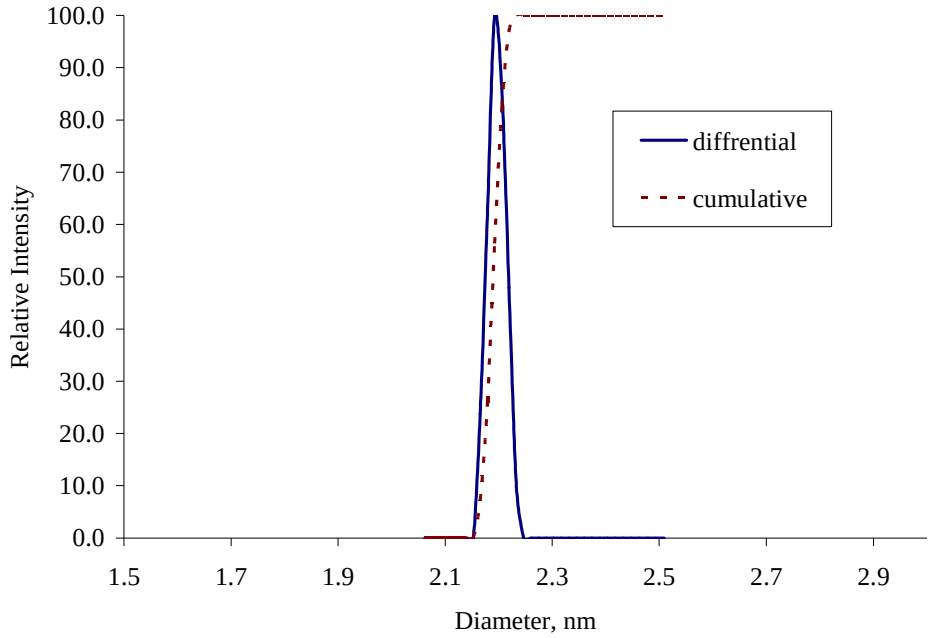

Figure 3.5: Size distribution of unswollen reverse micelles (0.1 M AOT/Iso-octane) using NNLS algorithm.

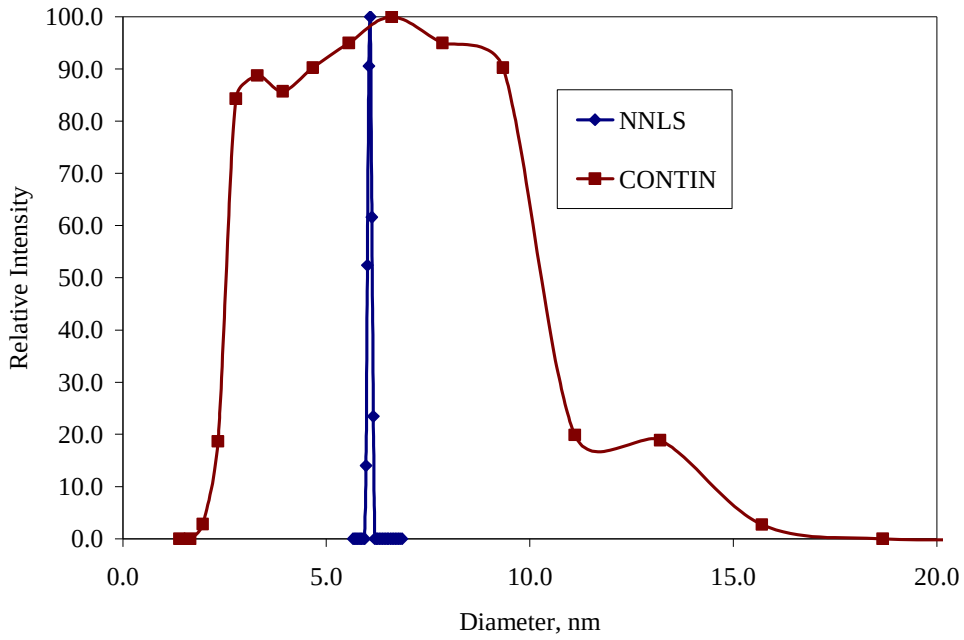

Figure 3.6: Size distribution of swollen reverse micelles (0.1 M AOT/0.1 M Brij30 / Iso-octane) using NNLS & CONTIN algorithms.

NNLS (Non-Negative Least Squares) and CONTIN (Constrained Regularization Algorithm for Inverting Data) are two different numerical algorithms that can be used to calculate particle size distribution based on the available information from the second order auto-correlating function. CONTIN has an additional data smoothening constraint that results in a broad distribution when compared to NNLS. The reverse micellar system consists of trace amounts of individual surfactant molecules and unswollen reverse micelles along with the swollen reverse micelles. Apart from these, larger aggregates of reverse micelles are also present transiently. Figure 3.6 illustrates that NNLS is not as sensitive to the presence of these trace species, whereas CONTIN is quite sensitive to the presence of other species in trace amounts and attempts to provide an equivalent unimodal distribution. The interpretation of PSD results using these algorithms requires a complete understanding and appreciation of the pros and cons of the algorithm used to deconvolute scattering fluctuations to predict particle size, as well as thorough knowledge of the various possible species that can be present in a sample.

3.3.4 Synthesis of Nanoparticles - Mixing of Reactants

In this method, hydrogen tetrachloroaurate ($HAuCl_4$) is reduced with hydrazine hydrate (N_2H_5OH) [18]. A surfactant, sodium di-2-ethylexylsulfoccinate commonly called Na(AOT) and a co-surfactant(which acts as structure modifier and stabilizer for gold nanoparticles) tetraethylene glycol dodecyl ether(C12E4/Brij) are used to form reverse micelles in water/iso-octane system. Two reverse micellar solutions of gold chloride and hydrazine hydrate are prepared as described in section 3.3.3. Gold chloride aqueous solution is aged for 17 days and the reverse micellar solutions of both gold chloride and reducing agent are aged for 4 days. The effect of aging the solutions is discussed in section 3.3.4.2. A 10 ml reverse micellar solution of gold chloride is transferred into a 50 ml round bottomed flask at room temperature, and 10 ml reverse micellar solution of reducing agent is directly added to the flask with rapid mixing. In the flask, the gold solution and hydrazine hydrate solution are exchanged amongst the micelles and react to yield gold nanoparticles by the following reaction [18].

$$4HAuCl_4 + 3N_2H_5OH \xrightarrow{reduction} 4Au + 16HCl + 3N_2 + 3H_2O \qquad (3.3)$$

The solution is vigorously stirred for about 20 minutes to allow the reaction to proceed towards completion. Dynamic light scattering measurements indicate that the mean particle size of the sample is 10.7 ± 0.43 nm and polydispersity is 0.1 ± 0.044 (based on 3 repetitive measurements). The particle size distributions obtained by NNLS & CONTIN are shown in the figure 3.7, and the UV-Visible absorption spectrum that shows a plasmon resonance at 525 nm is presented as figure 3.8. The shoulder seen around 280 nm in the UV-Vis spectrum indicates the presence of unreacted gold chloride solution. As shown in the figure 3.7, the NNLS predicts a narrow size distribution, whereas CONTIN predicts a wider distribution although the mean particles sizes predicted by both the algorithms are similar. This is due to the constraints in the algorithm. Generally, the polydispersity values predicted by DLS are more reliable and in this case, it supports the distribution obtained by NNLS.

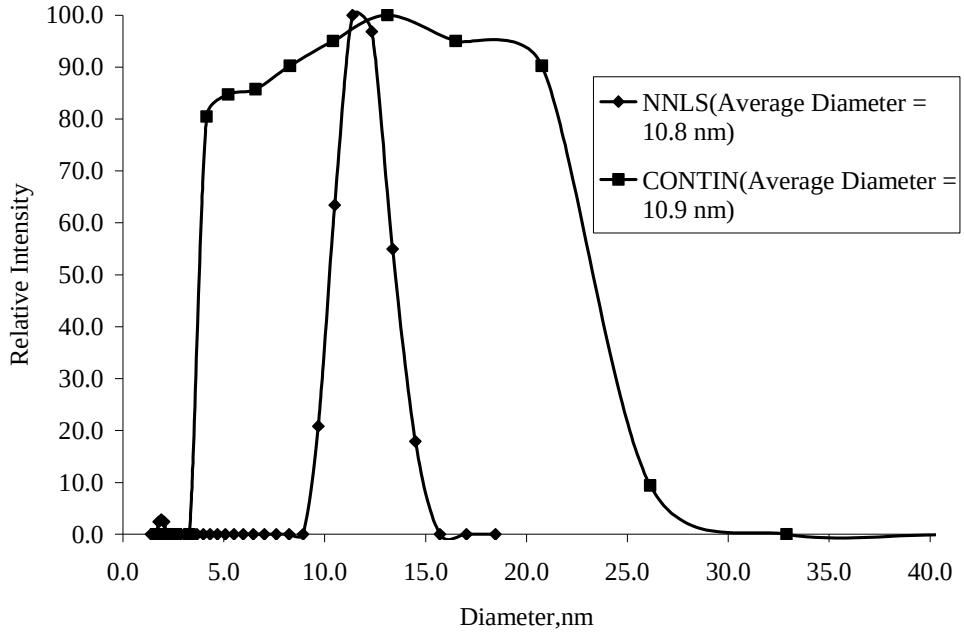

Figure 3.7: Particle size distribution of gold nanoparticles (sample DSP20) prepared by reverse micelle method with NNLS & CONTIN algorithms. [AOT] = 0.1 M, [$C_{12}E_4$] = 0.2 M, W_o = 8, [$HAuCl_4$] = 0.05 M, [N_2H_5OH] = 0.125 M.

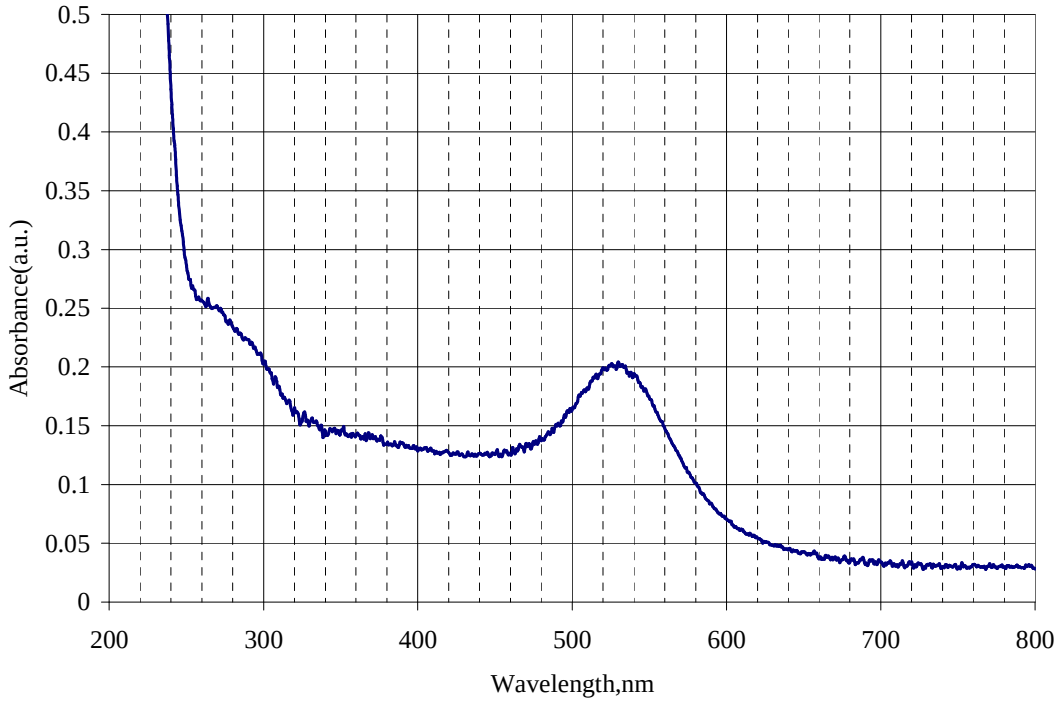

Figure 3.8: UV-Visible absorption spectrum of gold nanoparticles (sample DSP20) synthesized by the reverse micelle method.

Three similar experiments were done by maintaining same experimental conditions and samples(Rep_R_1, Rep_R_2, Rep_R_3) are characterized with DLS and the standard deviation bar is found to be 0.7 nm. As explained in the introduction section 3.3.1, several factors control the particle size and particle size distribution of the sample prepared by this technique. The effect of these factors on nanoparticle size and size distribution were verified experimentally and these experiments are discussed below.

3.3.4.1 Effect of Co-surfactant (Brij 30)

Chiang [18] reports that the co-surfactant $C_{12}E_4$ acts as a structure modifier and stabilizer for the particles to prevent further agglomeration and precipitation. To verify this two experiments were performed; one without the addition of co-surfactant (sample DSP01) and another (sample DSP16) with co-surfactant. The reverse micellar solution of gold chloride was initially taken in the reactor and the reverse micellar solution of reducing agent was injected, using a home-made syringe pump fabricated by Mr. Prakash, in a span of 10 seconds and the solution was stirred for about 20 minutes. DLS characterization of the resultant solutions indicate that for nearly identical conditions of aging, there is a significant difference in the particle sizes as shown in table 3.1. The experiment with co-surfactant gives rise to particles with an average size of 28.2 ± 0.07 nm particles, whereas without the co-surfactant very large particles (203 ± 9 nm) are produced. The UV-Visible absorption spectra of these two solutions are shown in figure 3.9. From these results, it can be concluded that the co-surfactant plays a very significant role in stabilizing the particles.

Co-surfactant concentration	Diameter(DLS)	Aging as aqueous solution (hrs)	Aging as micellar solution (hrs)
0.0 M (DSP01)	203 ± 9.4	240	96
0.2 M (DSP16)	28.2 ± 0.07	96	96

Table 3.1: The effect of co-surfactant concentration on particle size. [AOT] = 0.1 M, W_o = 8, [$HAuCl_4$] = 0.05 M, [N_2H_5OH] = 0.125 M

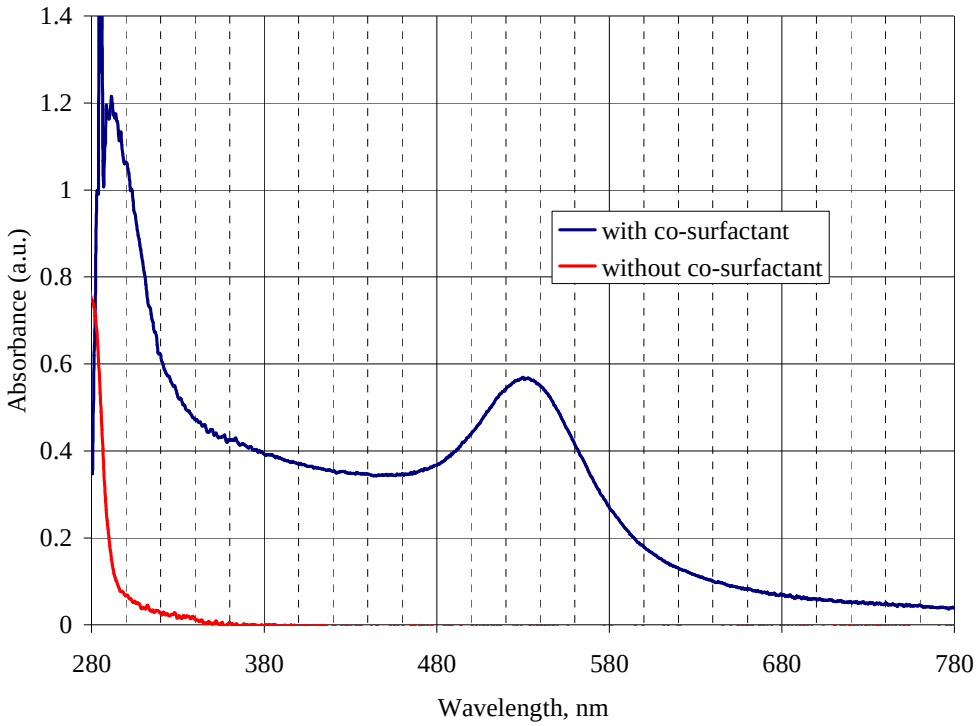

Figure 3.9: UV-Visible absorption spectrums for two different samples showing the effect of co-surfactant. [AOT] = 0.1 M, W_o = 8, [$HAuCl_4$] = 0.05 M, [N_2H_5OH] = 0.125 M The absence of a surface plasmon absorption band around 525 nm for the solution synthesized without co-surfactant indicates the absence of nanoparticles in the solution.

3.3.4.2 Effect of Aging Reagent Solutions

Experimentally, it was found that aging of the solution plays a very important role in determining particle size and yield. There are two kinds of aging namely, aging in aqueous solution and aging as reverse micellar solution. It is found that aging of gold chloride solution in the aqueous phase is essential for obtaining gold nanoparticles and that the minimum aging time required differed for the gold salts supplied by the two different suppliers, sigma (1 day) and Kemie Labs (4 days). This was an unexpected feature and so, the effect on nanoparticle synthesis of aging in aqueous solutions could not be studied systematically. The aging in reverse micellar solution was studied systematically and it is shown that smaller particles are produced for longer aging periods as shown below with experimental evidence. Four different experiments were done with various aging periods of reverse micellar solutions,

ranging from 0-4 days. 10 ml of reverse micellar solution of reducing agent was added to a 10 ml reverse micellar solution of gold chloride (Kemie Labs) within 5 seconds and under vigorous stirring. The DLS characterization results are shown in table 3.2. The UV-Vis absorption spectra for all these samples are plotted in figure 3.10.

Sample	Aging in aqueous solution(hrs)	Aging in micellar solution(hrs)	Diameter (DLS)
DSP13	96	0	112 ± 21
DSP14	96	24	80 ± 9
DSP15	96	48	55 ± 1.63
DSP16	96	72	28.2 ± 0.07

Table 3.2: Variation of particle size with aging of reverse micellar solution. [AOT] = 0.1 M, [$C_{12}E_4$] = 0.2 M, W_o = 8, [$HAuCl_4$] = 0.05 M, [N_2H_5OH] = 0.125 M.

It is clear from the experimental observations that aging of the reagent solutions within the reverse micelles affects the particle size and the yield of the particles. In order to understand the effect of aging in reverse micelles, UV-Visible absorption spectra are obtained as a function of time for both aqueous solution of gold chloride and reverse micellar solution of gold chloride. These are shown in figures 3.11 and 3.12 for aqueous gold chloride solution from Kemie labs and Sigma Co respectively. Figure 3.13 shows the time evolution of absorbance peak of a reverse micellar solution containing gold salt (Sigma). It can be concluded that the wavelength corresponding to the absorbance peak is not a function of time for both aqueous and reverse micellar solutions of gold chloride. It is also found that there is a shift in the wavelength corresponding to absorbance peak from aqueous solution of gold chloride to reverse micellar solution of gold chloride. The aqueous solution has a peak around 295 nm, whereas the reverse micellar solution has a peak at 325 nm. This shift in the wavelength is attributed to the different environment around the water droplet in the micro-emulsion. A similar kind of observation was made by Dutta et al.[22] while synthesizing zeolites in reverse micelles. They report a peak shift of 8 nm from aqueous solution to reverse micellar solution of the reactant species. The aging of

gold chloride within reverse micelles seems to produce smaller particles as shown in table 3.2. The effect of aging as aqueous solution and as reverse micellar solution on the particle size is not well understood yet. It is believed that the aging as aqueous solution somehow influences the solution to yield more nuclei as reported by Ellison et al.[23] in the case of ferric chloride solutions.

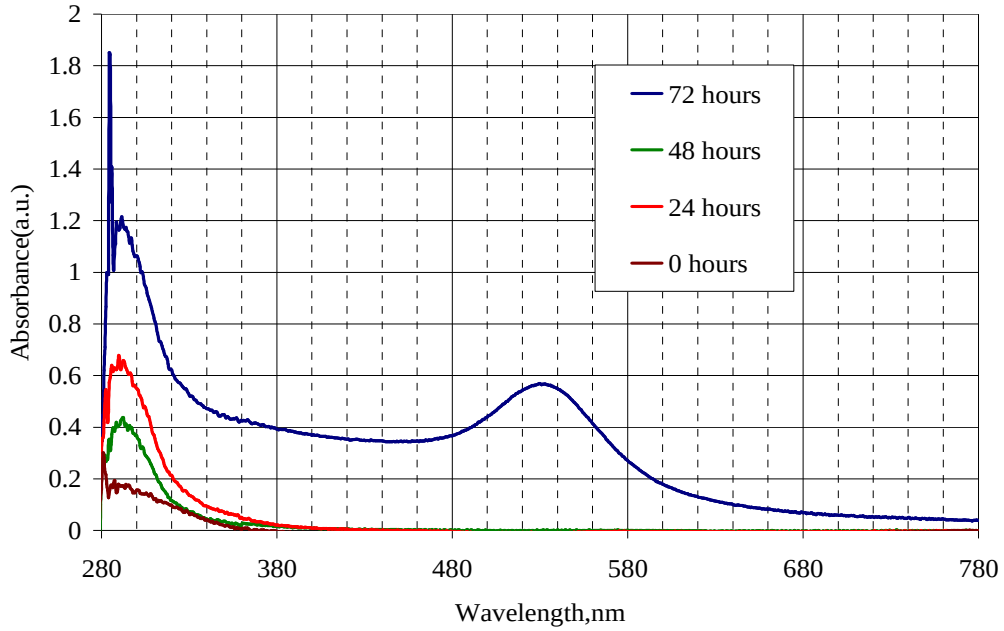

Figure 3.10: UV- Visible absorption spectra of gold nanoparticle solutions as a function of reverse micellar aging time. [AOT] = 0.1 M, [$C_{12}E_4$] = 0.2 M, W_o = 8, [$HAuCl_4$] = 0.05 M (Kemie Labs), [N_2H_5OH] = 0.125 M. The absence of surface plasmon resonance peaks for aging times less than 72 hours indicates the absence of nanoparticles in those solutions.

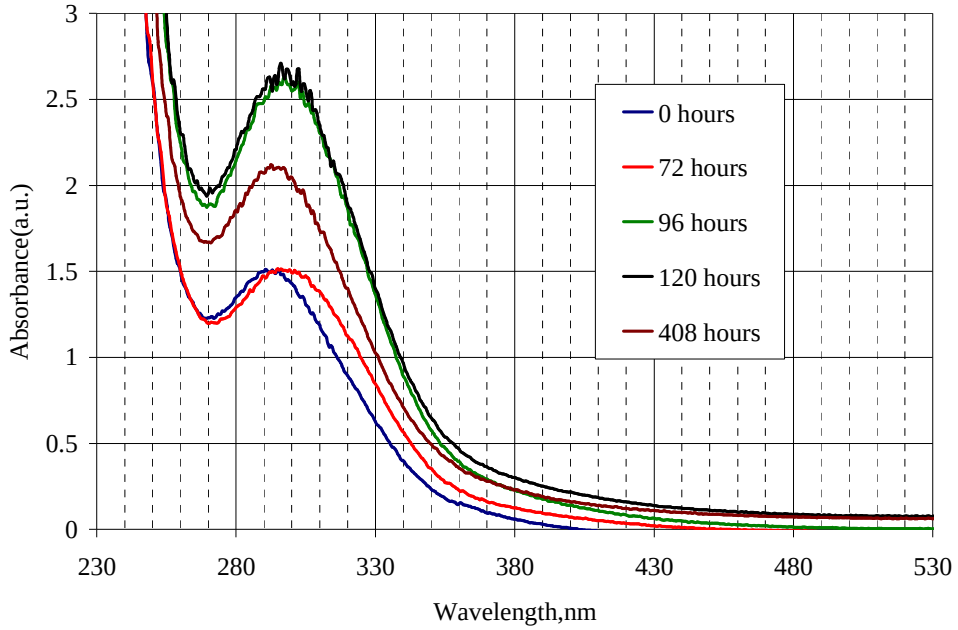

Figure 3.11: UV-Visible absorption spectra for aqueous solution of gold chloride (Kemie Labs) as a function of time. The difference in absorbance values is due to different concentrations used during measurements.

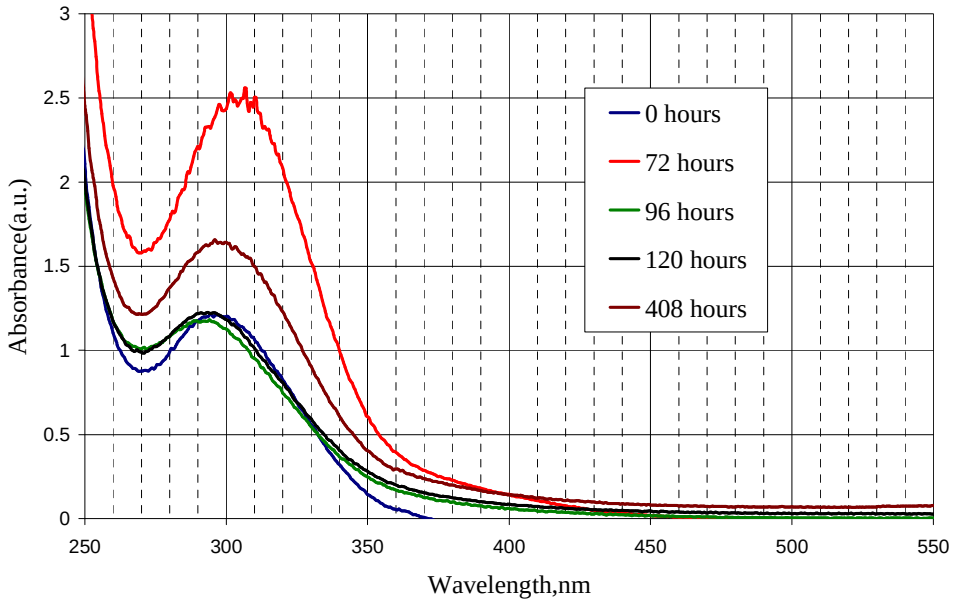

Figure 3.12: UV-Visible absorption spectra for aqueous solution of gold chloride (Sigma) as a function of time. The difference in absorbance values is due to different concentrations used during measurements.

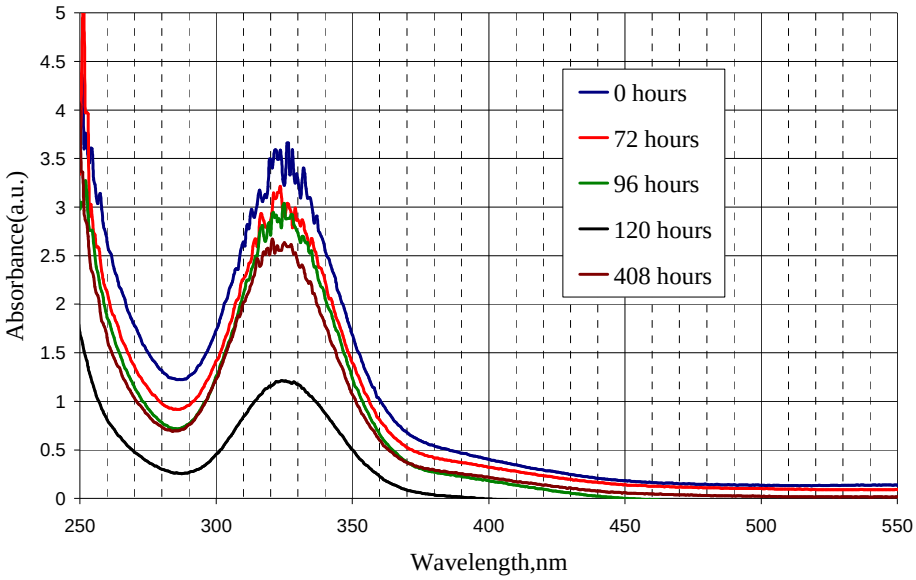

Figure 3.13: UV-Visible absorption spectra for reverse micellar solution of gold chloride(Sigma) as a function of time. The difference in absorbance values is due to different concentrations used during measurements.

3.3.4.3 Effect of Injection Time and Temperature

The effect of injection time on mean particle size is expected to be significant [24]. If the reducing agent is added slowly to the reactor, the nuclei that are generated in the beginning can incorporate the atoms formed at later instances and thus grow into bigger particles. This scenario is valid in the case of the reaction occurring in a continuous phase. However, reverse micelles can behave as individual nano-reactors and in the absence of rapid interactions amongst the micelles containing nanoparticles, one would expect to generate nuclei over the whole duration and thus produce smaller particles. In both cases, it is assumed that the redox reaction is instantaneous, which is a valid assumption for this case.

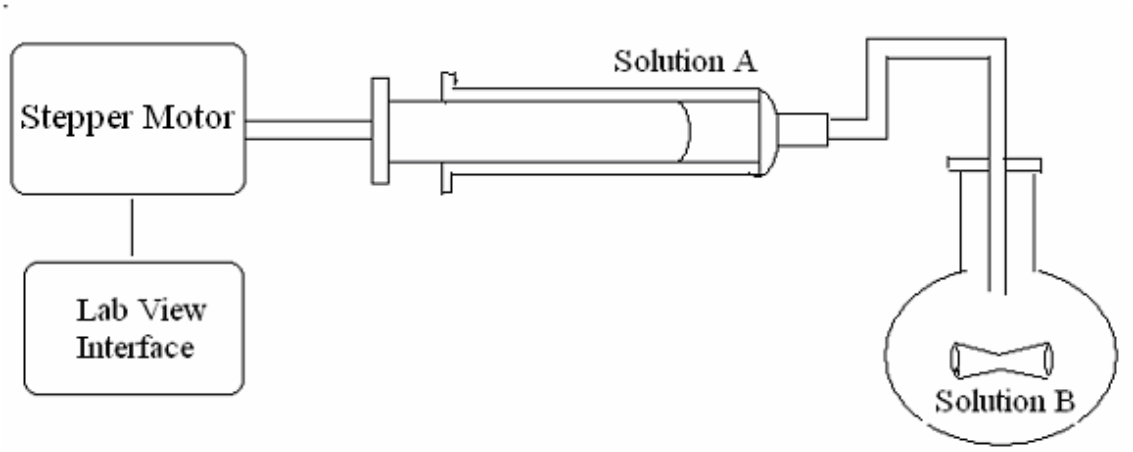

Figure 3.14: Schematic of experimental set-up to synthesize gold nanoparticles by reverse micelle technique [16]

Two reverse micellar solutions containing Gold chloride (solution B) and Hydrazine (solution A) were prepared by adding corresponding aqueous solution into an isooctane solution of AOT/$C_{12}E_4$ as explained before. Then, these two solutions are mixed in a reactor as shown in the figure 3.14. Initially reverse micellar solution of gold salt is taken in the reactor and then a reverse micellar solution of aqueous hydrazine hydrate is injected into it with the help of a stepper motor controlled injection system (developed by Mr. Prakash). Initially, experiments were performed by varying the injection time over a range of 1-70 seconds. The aqueous solution of gold chloride was aged for 24 hours and the micellar solutions of both the reactants were aged for about 7 hours at ambient conditions. DLS characterization results are presented in table 3.3 and UV-Visible absorption spectra are presented in figure 3.15. It is seen that the direct addition of the two reactants under otherwise similar experimental conditions produces bigger particles. Also, there is hardly any change in particle size as the injection time is varied from 10-70 seconds. This leads one to conclude that particle size is independent of injection time and this is inconsistent with an earlier set of experiments performed by Clothilde Depue in November 2005, an intern in Prof. Sanjeev Gupta's lab. It was hypothesized that the range of injection times over which particle size changes is a sensitive function of temperature and that is the cause of this apparent discrepancy. In order to appreciate this aspect, it is necessary to understand the reaction sequence. When two reverse micellar solutions are mixed together, the individual micelles are in random Brownian motion and will

collide with other micelles in their vicinity. Thus, any two micelles can fuse together to form a transient dimer and exchange their contents before breaking apart. If the two micelles are of different kinds then nucleation (gold salt and reducing agent react to give atoms) or growth (if a nuclei is already present from previous collisions) can occur. Thus the fusion of reverse micelles is a critical step in both nucleation and growth of nanoparticles[24]. The fusion efficiency is reported to be a strong function of temperature in the range of 20-30ºC and almost doubles for a change from 25 to 30ºC[21]. To verify this hypothesis, additional sets of experiments were conducted at different temperatures. Apart from this aging of gold solutions was also varied to observe its effect on the results. Four sets of experiments were performed by varying the temperature or particle aging. These conditions are:

1) T= 29ºC, Aging Conditions: Aqueous phase – 17 days, Reverse micelle – 1 day
2) T= 31ºC, Aging Conditions: Aqueous phase – 17 days, Reverse micelle – 1 day
3) T= 27ºC, Aging Conditions: Aqueous phase – 18 days, Reverse micelle – 2 days
4) T= 30ºC, Aging Conditions: Aqueous phase – 18 days, Reverse micelle – 2 days

Apart from these, the concentrations and amounts are all exactly the same as those used for the previous set of experiments (samples DSP23 to DSP 28). Fig 3.16 is a series of spectra taken for condition 3. It shows that there is a red shift of the surface plasmon peaks for injection times greater than 60s and it disappears for an injection time of 120s. This is an indication that large particles are produced after 60s and that particles have settled for sample DSP54 (120s injection time). These results are also corroborated by DLS characterization results. The digital pictures of various gold nanoparticle samples are presented in appendix A8.

Sample	Injection time(sec)	Effective Diameter(nm)	Polydispersity
DSP23	direct addition (~1 s)	51.9 ± 0.70	0.289 ± 0.003
DSP24	10	24.7 ± 0.13	0.200 ± 0.006
DSP25	20	27.0 ± 0.16	0.190 ± 0.006
DSP26	30	27.7 ± 0.05	0.198 ± 0.003
DSP27	50	27.3 ± 0.09	0.138 ± 0.002
DSP28	70	26.9 ± 0.00	0.159 ± 0.002

Table 3.3: The variation of particle size (DLS) with injection time of reducing agent. [AOT] = 0.1 M, [$C_{12}E_4$] = 0.2 M, W_o = 8, [$HAuCl_4$] = 0.05 M, [N_2H_5OH] = 0.125 M. The measurements were repeated thrice.

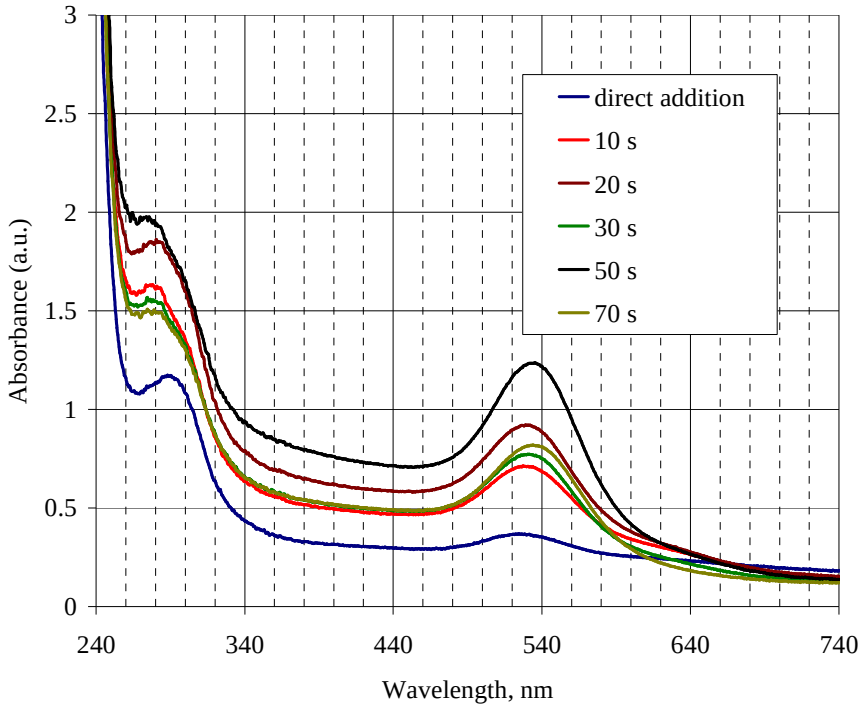

Figure 3.15: UV-Visible absorption spectra of gold nanoparticles as a function of injection time of reducing agent. . [AOT] = 0.1 M, [$C_{12}E_4$] = 0.2 M, W_o = 8, [$HAuCl_4$] = 0.05 M, [N_2H_5OH] = 0.125 M.

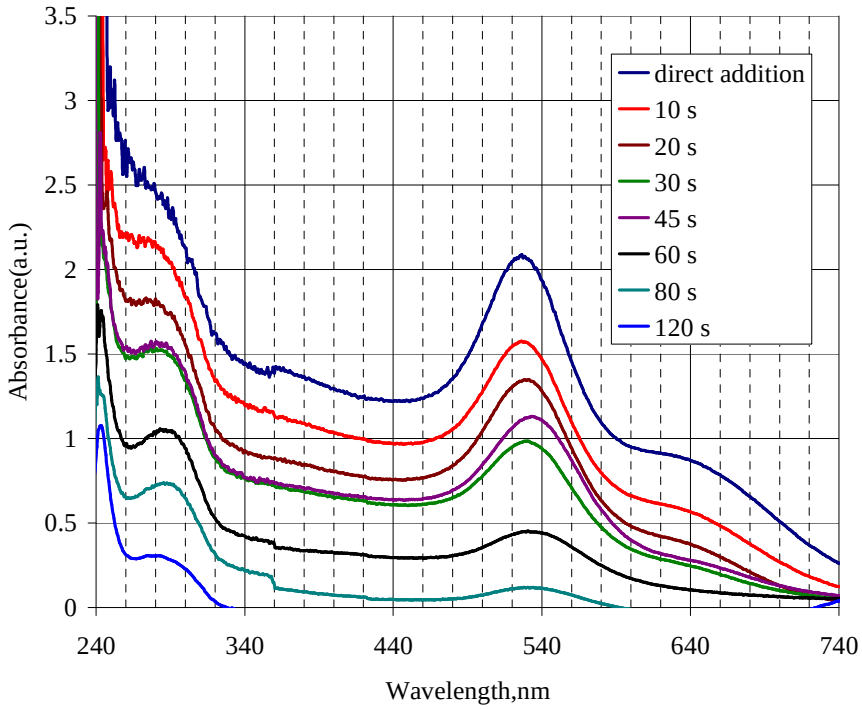

Figure 3.16: UV-Visible absorption spectra of gold nanoparticles as a function of injection time of reducing agent. . [AOT] = 0.1 M, [$C_{12}E_4$] = 0.2 M, W_o = 8, [$HAuCl_4$] = 0.05 M, [N_2H_5OH] = 0.125 M., T = 27 ^oC.

Serial number	Injection time (sec)	Effective diameter(DLS) (nm, T = 29^{o}C)	Effective diameter(DLS) (nm, T = 31^{o}C)
1	direct addition(~1)	64.0 ± 1.60 (DSP43)	37.6 ± 0.08(DSP39)
2	6	40.9 ± 0.37(DSP46)	48.0 ± 0.83(DSP40)
3	10	48.9 ± 0.46(DSP44)	101 ± 4.90(DSP38)
4	20	103 ± 1.70(DSP45)	-

Table 3.4: The effect of injection time and temperature on mean particle size. [AOT] = 0.1 M, [$C_{12}E_4$] = 0.2 M, W_o = 8, [$HAuCl_4$] = 0.05 M, [N_2H_5OH] = 0.125 M, reverse micellar aging 24 hours.

Serial number	Injection time (sec.)	Effective diameter (DLS, nm) 27^{o}C	Effective diameter (DLS, nm) 30^{o}C
1	direct addition	32.0 ± 0.24(DSP47)	30.0 ± 0.14(DSP55)
2	10	23.0 ± 0.08(DSP48)	25.0 ± 0.29(DSP56)
3	20	22.8 ± 0.08(DSP49)	34.0 ± 0.30(DSP57)
4	30	22.6 ± 0.17(DSP50)	32.3 ± 0.37(DSP58)
5	45	22.3 ± 0.08(DSP51)	57.7 ± 0.94(DSP59)
6	60	33.0 ± 0.75(DSP52)	-
7	80	66.0 ± 1.00(DSP53)	-
8	120	89.0 ± 0.19(DSP54)	-

Table 3.5: The effect of injection time and temperature on mean particle size. [AOT] = 0.1 M, [$C_{12}E_4$] = 0.2 M, W_o = 8, [$HAuCl_4$] = 0.05 M, [N_2H_5OH] = 0.125 M, reverse micellar aging 48 hours.

The average size and polydispersity values based on DLS characterization are tabulated for conditions 1) and 2) in table 3.4, and for conditions 3) and 4) in table 3.5. The results for average particle sizes are summarized in figure 3.17. It is clear from the figure 3.17 that as the temperature increases; the mean particle size also increases. It is clear that the change in aging of the reverse micellar solution produces smaller particles as discussed previously.

3.4 Conclusions and Outlook

From the experimental results obtained so far, the following inferences can be made.

1) It is shown that minor changes in temperature play a very significant role in the control of particle size.

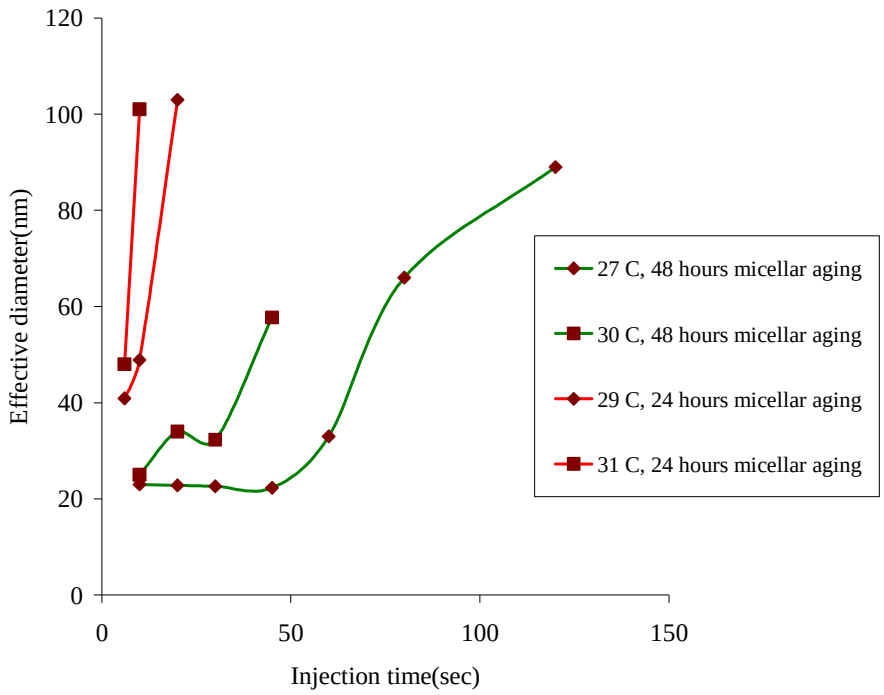

Figure 3.17: The combined effect of injection time, temperature and aging within reverse micelles on mean particle size. [AOT] = 0.1 M, [$C_{12}E_4$] = 0.2 M, W_o = 8, [$HAuCl_4$] = 0.05 M, [N_2H_5OH] = 0.125 M.

2) The threshold injection time needed to produce effects of mixing time on nanoparticle size is representative of the timescales involved in reverse micelle fusion and exchange process. Once the injection time crosses that threshold, growth of previously formed nuclei dominates, whereas below that threshold nucleation dominates. This threshold is affected by the period of aging. The reproducibility of direct addition experiments are not good as we are unable to control the nature and extent off mixing reproducibly.

3) The aging of solutions is found to significantly affect the nanoparticle size formed. This is not well understood presently, and the fact that gold salt procured from different vendors have different aging requirements makes it difficult to analyze. Empirically, it is found that aging in aqueous phase for 17 days and in reverse micellar phase for a minimum of 2 days is required for reproducibility.

4) The gold nanoparticles encapsulated by AOT/Brij30 reverse micelles do not exhibit long term stability (period of weeks) and this aspect needs to be studied more carefully.

The following chapter presents a discussion based on some preliminary attempts at modeling the sensitive temperature and injection time dependence.

3.5 References

[1] Santhanam V, Andres R P, "Metal Nanoparticles and Their Self-Assembly into Electronic Nanostructures", Encyclopedia of Nanoscience and Nanotechnology, Marcell Dekker, 1829-1840.

[2] Naoki T, Jetsu Y, "Bimetallic nanoparticles-novel materials for chemical and physical applications", New J. Chem., **22**, 1179-1201(1998).

[3] Chen Q, Zhang Z J, "Size-dependent super-paramagnetic properties of $MgFe_2O_4$ spinel ferrite nanocrystallites", Applied physics letters, **73**(21), 3156-3158(1998).

[4] El-Sayed I H, Huang X, El-Sayed M A, "Surface Plasmon Resonance Scattering and Absorption of anti-EGFR Antibody Conjugated Gold Nanoparticles in Cancer Diagnostics: Applications in Oral Cancer", Nanoletters, **5**(5), 829 – 834(2005).

[5] Panyam J, Labhasetwar V, "Biodegradable nanoparticles for drug and gene delivery to cells and tissue", Adv Drug Deliv Rev., **55**, 329-347(2003).

[6] Gratzel M, "Photoelectrochemical cells", Nature, **414**, 338-344(2001).

[7] Santhanam V, PhD Thesis, Purdue University, 2002.

[8] Turkevich J, Stevenson P C, "A Study of nucleation and growth processes in synthesis of colloidal gold", Discuss. Faraday Soc., **11**, 55-75(1951).

[9] Wegner K, Walker B, Tsantilis S, Pratsinis S E., " Design of metal nanoparticle synthesis by vapor flow condensation". Chem. Eng. Sci., **57,** 1753 –1762(2002).

[10] Marine W, Patrone L, Luk'yanchuk B, Sentis M., "Strategy of nanocluster and nanostructure synthesis by conventional pulsed laser ablation", Appl. Surf. Sci., **154**, 345 –352(2000).

[11] Swihart M T, "vapour phase synthesis of nanoparticles", Current Opinion in Colloid and Interf. Sci., **8,** 127-133(2003).

[12] Brust M, Walker M, Bethell D, Schiffrin D J., "Synthesis of thiol-derivatised gold nanoparticles in a two phase liquid-liquid system". J.Chem. Soc., Chem. Commun., **7**, 801-803(1994).

[13] Slot W, Geuze H J, "A new method of preparing gold probes for multiple labeling cytochemistry", Journal of Cell Biology, **38,** 87-93(1985).

[14] Chia-Hao S, Pei-Lin W, "Sonochemical synthesis of well dispersed gold nanoparticles at the ice temperature", J.Phys. Chem.B, **107**, 14240-14243(2003).

[15] Liu Y C, Chuang T C, **"**Synthesis and characterization of gold/polypyrrole core- shell nanocomposites and elemental gold nanoparticles based on the gold- containing nanocomplexes prepared by electrochemical methods in aqueous solutions", J.Phys. Chem. B, **107**, 12383-12386(2003).

[16] Giersig M., Mulvaney P, "Preparation of ordered monolayers by electrophoretic deposition", Langmuir, **9**, 3408-3413(1993).

[17] Venugopal S, Jia L, Rajan A, Andres R P, "Self assembly of uniform monolayer arrays of nanoparticles", Langmuir, **19**, 7881-7887(2003).

[18] Chen Li-Chiang, "Controlled growth of gold nanoparticles in AOT/ Iso-octane/$C_{12}E_4$ mixed reverse micelles", J. of Colloid. & Interface,**239,** 334-341(2001).

[19] Herrera A P, Resto O, Briano G J, Rinalde C, " Synthesis and agglomeration of gold nanoparticles in reverse micelles", Nanotechnology, **16**, 618-625(2005).

[20] Bohidar H B, Behboudnia M, " Characterization of reverse micelles by dynamic light scattering", Colloids and Surfaces(A), **178**, 313-323(2001).

[21] Fletcher P D I, Howe A M, Robinson B H, " The kinetics of solubilisate exchange between water droplets of a water-in-oil microemulsion", J. Chem. Soc.,Faraday Trans. 1, 83, 985-1006(1987).

[22] Dutta P K, Robins D, "Synthesis of zeolites A from reactants enclosed in reverse micelles", Langmuir, **7**, 1048-1050(1991).

[23] Ellision H L, Hazel F, "Influence of concentration and age on some colloidal properties of ferric chloride solutions", The J. of Phys. Chem.,**1**, 829-835(1935)

[24] Singh R, Kumar S, "Effect of mixing on nanoparticle formation in micellar route", Chem Eng Sci., **61**, 192-204(2006).

Chapter 4

MODELLING OF GOLD NANOPARTICLE FORMATION

4.1 Introduction

The controlled manufacture of gold nanoparticles using solution-based synthesis methods depends primarily on an understanding of the kinetics of nucleation and growth. In order to optimize the conditions needed to produce monodisperse gold nanoparticles while being able to manipulate the particle size, modeling is essential.

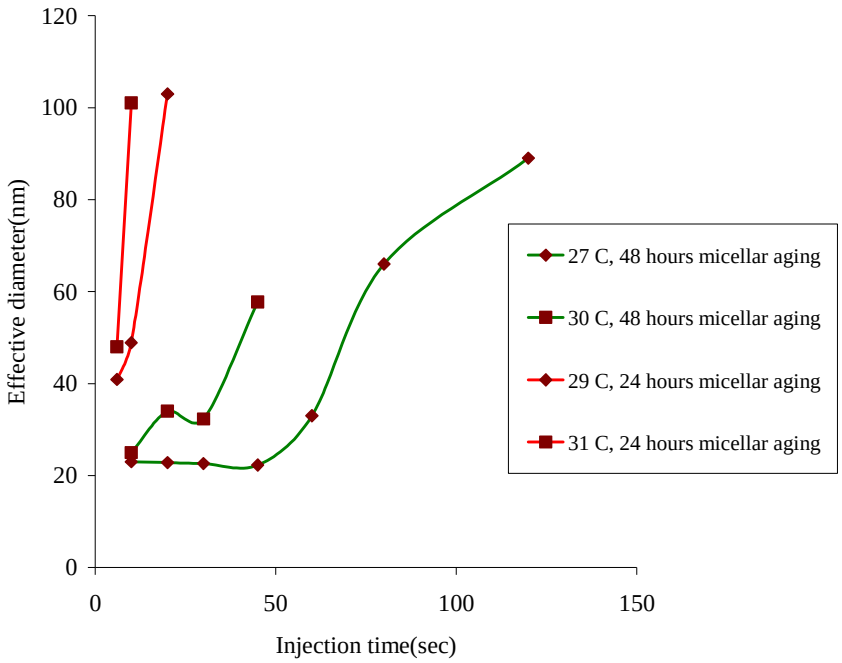

Figure 4.1: The effect of temperature and rate of addition of reducing agent (injection time of reducing agent) on the mean particle size of gold nanoparticles.

As discussed in the previous chapter, there are several factors affecting the mean particle size of the gold nanoparticles synthesized in reverse micelles. These include ratio of gold chloride to reducing agent, mole ratio of water to surfactant, aging of the solutions (both aqueous and micellar aging), rate of addition of reducing agent to the reaction system, and temperature of the system. The experimentally determined effect of temperature and rate of addition of reducing agent (injection time of reducing

agent) are shown in the figure 4.1. In order to explain these trends a very simple qualitative model, to understand the effects of temperature and rate of addition is developed and presented in the following section.

4.2 A Simple Qualitative Model

Consider two extreme situations of the rate of addition of the reducing agent to a gold chloride solution in a continuous phase. If the reducing is added rapidly, it will lead to the formation of a greater number of nuclei and will finally lead to a relatively smaller average particle size, when compared to the case of adding reducing agent over a very large period. In the latter case, nucleation occurs in the beginning only as it is not possible to achieve sufficient super saturation concentration at later times due to the faster kinetics of the growth of existing particles leading to relatively larger size particles.

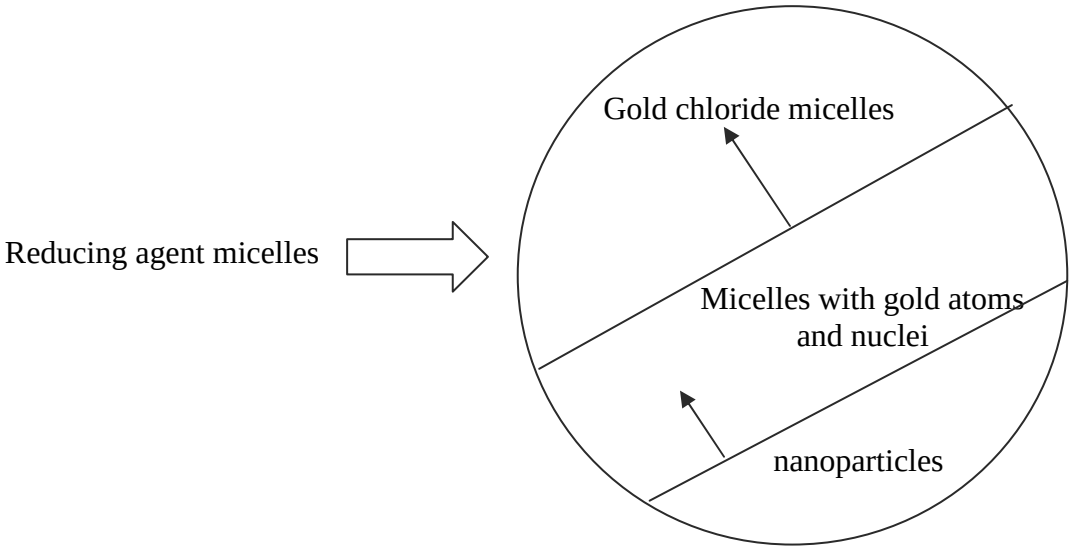

Figure 4.2: Schematic representation of the model when there is no interaction among the reverse micelles. The sphere represents the set of all reverse micelles that contain gold in charged or neutral state. The reducing agent is always present in excess and is not explicitly considered in this case.

In reverse micellar synthesis reaction occurs inside the micelle. These micelles can behave as separate reactors or act as a quasi-continuous phase depending on the rate of inter-micellar interactions that lead to exchange of contents between two micelles.

In the absence of inter-micellar interactions the reaction system can be treated as if it consists of three different compartments as shown in the figure 4.2. These compartments are namely, nanoparticles in reverse micelles, gold chloride containing reverse micelles, and reverse micelles with gold atoms and nuclei. One can imagine two boundaries separating these three different populations. These boundaries are not physical as these regions separated by boundaries represent the magnitude of the three different populations or as subsets of the larger set of all reverse micelles present in the system. Let us consider the scenario, where there are no interactions between these three different populations. When a differential amount of reducing agent is introduced in to the reaction system, it reacts with a differential amount of gold chloride micelles and produces some nuclei and many gold atoms. After this reaction these micelles become members of the second set of micelles (middle compartment). In the second compartment, on an average the ratio of the number of nuclei to gold atoms present within a reverse micelle can be assumed to be similar and hence are assumed to grow to a particular size and then become members of the third set (reverse micelles containing nanoparticles only). As there is no exchange between different kinds of micelles, no more atoms are available for the nanoparticles in third kind of micelles to grow and hence all the particles will be of the same size. These processes can be represented pictorially by assuming that the two boundaries represented in figure 4.2 move in the direction of the arrows until all the reverse micelles become nanoparticle laden. If the rate of addition is faster, it can be accounted for by assuming that the boundaries are moving faster (increase in one population and decrease in another population). But, this cannot alter the particle size as there is same number of atoms available for every nucleus on an average within every reverse micelle. So, in the absence of interaction, particle size is expected to be independent of the rate of addition of reducing agent.

In the presence of inter-micellar interactions, even though micelles are interacting among themselves two different kinds of populations are still expected. They are pure gold chloride micelles and complex micelles containing all kinds of possible species. One hypothetical boundary separating these two populations can be imagined as shown in the figure 4.3. In the present case reaction takes place in both kinds of

micelles. However, as soon as the reaction in pure gold chloride micelles leads to nucleation, they become members of the other set, where predominantly growth occurs within a reverse micelle. The population of pure gold chloride micelles reduces with time due to two types of events that occur in parallel. One is due to reaction and the other is due to interaction. The time available for nucleation is the time required for all the pure gold chloride containing reverse micelles to disappear. As a result increased interaction among the micelles can reduce the time available for nucleation. To make this model a bit quantitative, two different time scales are defined. They are time scale for interaction (τ_{in}) and time scale for all the gold chloride micelles to disappear due to reaction. The second time scale is assumed to be equal to time of injection (τ_{inj}). The harmonic mean (parallel first order events) of these two time scales provides a new time scale which is the time available for nucleation ($\tau_{nucle.}$).

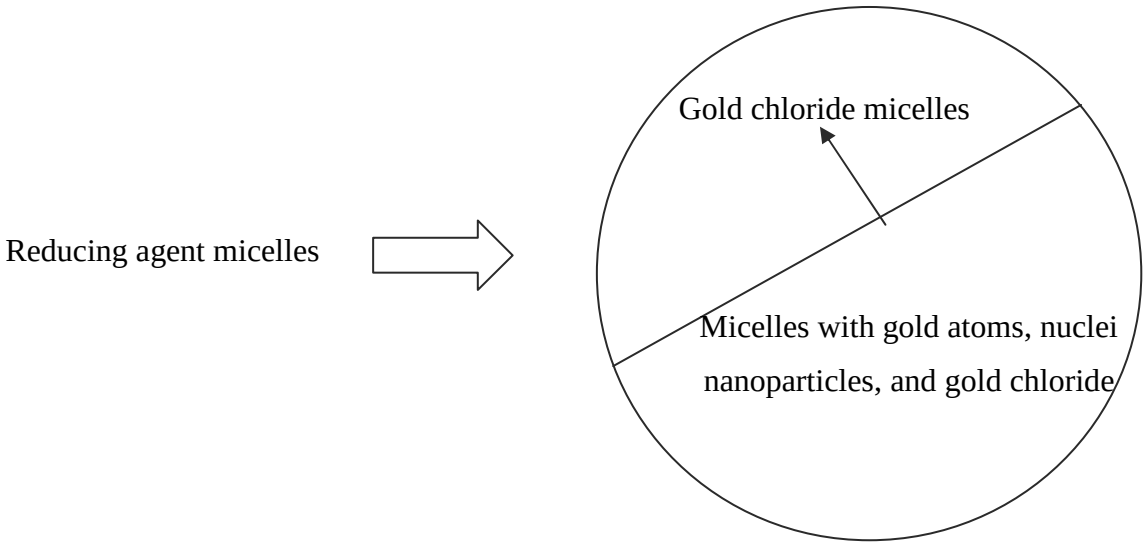

Figure 4.3: Schematic representation of the model when there is interaction among the reverse micelles. The sphere represents the set of all reverse micelles that contain gold in charged or neutral state. The reducing agent is always present in excess and is not explicitly considered in this case.

$$\tau_{nucle.} = \frac{1}{\left(\frac{1}{\tau_{inj.}} + \frac{1}{\tau_{in.}} \right)} \tag{4.1}$$

This equation can be rewritten as

$$N_{nuclei} \propto N_{particles} \propto \frac{1}{d^3} \propto \left(\frac{\tau_{nucle.}}{\tau_{inj.}} \right) = \frac{1}{1 + \frac{\tau_{inj}}{\tau_{in.}}} \tag{4.2}$$

The ratio of nucleation time to injection time represents the fraction of the reducing agent that contributes to nucleation by reaction. So it is proportional to the total number of nuclei present in the system which in turn is proportional to the total number of particles (aggregation and fracture of particles are neglected). For a given initial amount of gold chloride, the number of particles produced is inversely proportional to the cube of the diameter (d^3, i.e. proportional to volume) of an individual particle

$$d \propto \left(1 + \frac{\tau_{inj}}{\tau_{in.}}\right)^{(1/3)} \tag{4.3}$$

The qualitative trends expected based on equation 4.3 is shown in figure 4.4. At a constant temperature (where $\tau_{in.}$ is constant) increase in injection time produces bigger particles. Also, at any injection time increase in temperature reduces the magnitude of time scale of interaction which again results in increase in the particle size. Also, at very low values of the ratio of injection time to interaction time, this model predicts a negligible change in diameter or an almost constant particle size, which is in qualitative agreement with experimentally observed trends that are shown in figure 4.1. The two parameters are proportionality constant and $1/\tau_{int.}$

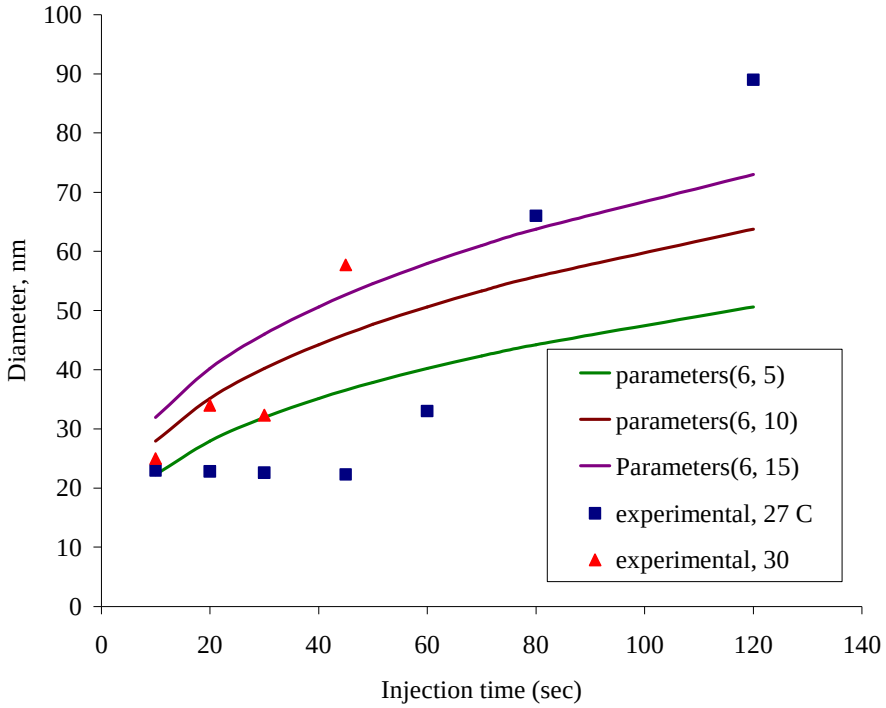

Figure 4.4: This plot shows the effect of temperature (interaction time scale) and the effect of injection time (rate of addition) on the particle size along with experimental data.

4.3 A Quantitative Model

In order to quantitatively explain experimentally observed trends a simple kinetic model is proposed. This model considers only three different micellar populations namely; pure gold chloride reverse micelles (N_g), pure reducing agent reverse micelles (N_r), and reverse micelles containing a single particle inside (N_p). The other possible kinds of reverse micelles are neglected for simplicity.

The following assumptions are made

1. When a pure gold chloride reverse micelle forms a temporary dimer with pure reducing agent reverse micelle with an interaction constant ‘k’, they will exchange their contents and disengage to form two reverse micelles again. These two micelles produce two nuclei and some gold atoms.

2. The micelle containing a particle inside may interact with a pure gold chloride reverse micelle and form a dimer with the same rate constant ‘k’. When this dimer disengages into two reverse micelles the particle may transfer to either reverse micelle with a probability of ‘f’. The same thing can happen in the case of pure reducing agent reverse micelle also.

3. The reverse micelles containing particles inside can interact among themselves and can form aggregates with the same rate constant ‘k’. All the processes are second order.

4. The redox reaction is assumed to be instantaneous and the vessel is assumed to be perfectly mixed.

Based on these assumptions the following equations can be written.

$$\frac{dN_g}{dt} = -kN_gN_r - fkN_gN_p \tag{4.4}$$

$$\frac{dN_r}{dt} = \left(\frac{N_o}{t_{inj}V}\right) - kN_gN_r - fkN_rN_p \tag{4.5}$$

$$\frac{dN_p}{dt} = 2kN_gN_r - kN_p^2 \tag{4.6}$$

$$\frac{dN_e}{dt} = kN_P^2 + fkN_gN_P + fkN_rN_P \tag{4.7}$$

$$\frac{dV}{dt} = \frac{V_R}{t_{inj}} \tag{4.8}$$

where,

N_g is the population of pure gold chloride reverse micelles per unit volume.

N_e is the population of empty(with out particle) reverse micelles per unit volume.

N_r is the population of pure reducing agent reverse micelles per unit volume.

N_P is the population of reverse micelles containing single particle inside per unit volume.

k is the second order rate constant for all the reverse micelle interaction processes.

N_o is the initial population of reverse micelles in either of the reactants.

t_{inj} is the injection time for reducing agent.

V is the volume of the fluid in the reactor at any time t.

V_R is the initial volume of the reactant fluid.

Initial conditions:

$V = V_R = 10$ mL.

$N_o = 4.3\ 10^{18}$ micelles per 10 mL.

$N_g = 4.3\ 10^{17}$ micelles / mL.

$N_P = 0$ micelles / mL.

$N_r = 0$ micelles / mL.

These equations are solved in time domain until $t = t_{inj.}$ for different values of k (same order of magnitude as those reported by Fletcher et al.). At the end N_P gives the total number of particles per unit volume.

The total amount of gold is assumed to be in the form of gold nanoparticles.

$$\frac{\pi}{6} d^3 (N_P V) \rho_{gold} = 4.1 \times 10^{-6} \tag{4.8}$$

The right hand side quantity is calculated from the molar concentration of gold chloride in aqueous solution. From the above expression the average diameter can be calculated based on the number of particles per unit volume. The value of ‘f’ is considered to be 0.5.

4.3.1 Results

Injection time(Sec.)	Diameter, nm for $k = 48.18 * 10^9$ (cm^3/mol.s)	Diameter, nm for 2k	Diameter, nm for 3k
10	25.2	31.8	36.4
20	31.8	40.1	46.0
30	36.4	45.9	52.6
45	41.7	52.6	60.2
60	45.9	57.9	66.3
80	50.6	63.8	73.0
120	57.9	73.0	83.6

Table 4.1: Model predicted values of the mean particle size of the gold nanoparticles synthesized in reverse micelles.

The average particle size of the samples, predicted by the model is tabulated in table 4.1 for three different rate constant values and the comparison between the experiment and the model is shown in figure 4.5. From the figure it can be inferred that increase in injection time produces bigger nanoparticles and also increase in rate constant or increase in temperature forms bigger nanoparticles. It is seen that a larger number of reverse micellar species needs to be included in the model to improve its ability to capture the experimental trend and also the effect of interplay between rate of addition and reverse micellar interaction time has to be incorporated to predict a threshold as explained in the qualitative model.

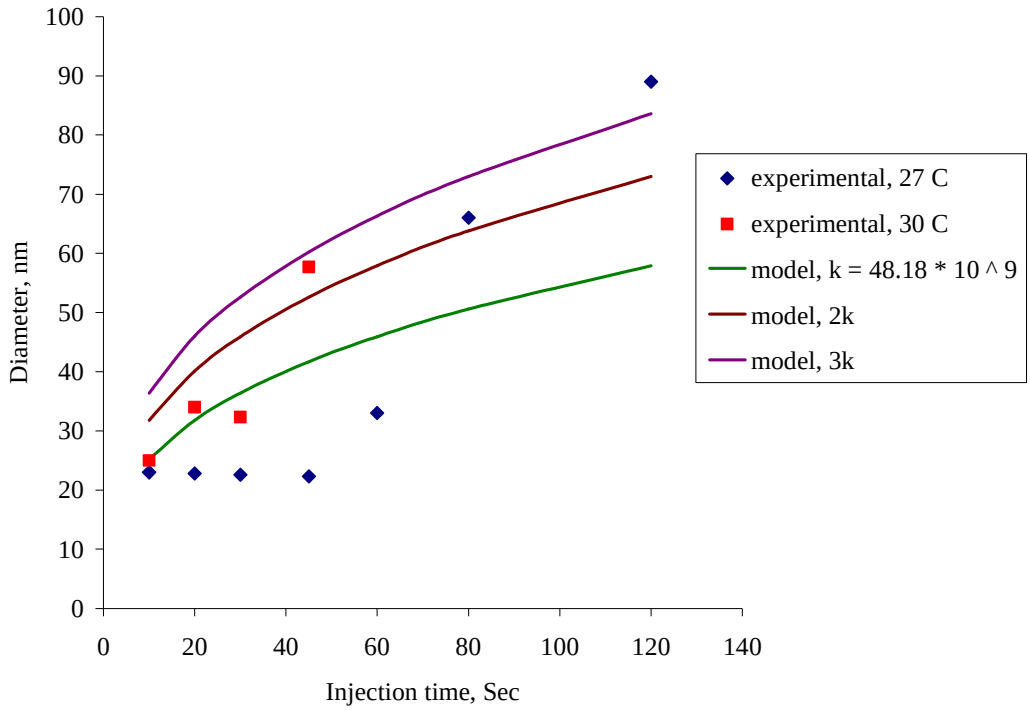

Figure 4.5: A comparison between the model and experimental observations.

4.4 Summary

A qualitative and quantitative model description of the experimental system has been outlined. This initial attempt at modeling needs to be further refined in order to be useful as a predictive model. The assumptions regarding the types of reverse micellar species considered, the types of interactions allowed, and the effect of mixing need to be relaxed in future models of this system.

Chapter 5
CONCLUSIONS AND OUTLOOK

Based on the discussions of the earlier chapters the following conclusions and recommendations for future work are presented:

- The various nuances involved in nanoparticle characterization by DLS have been studied in detail. Based on this study, the importance of choosing an appropriate first delay time, and optimal dilution of the sample to avoid interparticle interactions and multiple scattering have become clear.

- Synthesis of nanoparticle size in reverse micellar technique has been performed and the size of the nanoparticles and reverse micelles as measured by Dynamic light scattering agrees well with those reported in literature.

- The effect of the rate of addition of the reducing agent on the size of the nanoparticles formed has been characterized and it suggests a threshold for the injection time. Below this threshold time the nanoparticle size is not altered drastically and above this threshold the nanoparticle size increases dramatically and is only bounded by particle aggregation and settling.

- A preliminary model and a qualitative explanation of the processes behind these observations have been developed and experimental trends captured.

- The stability of nanoparticle solutions with time is poor and this can be improved by adding more strongly bound surfactants like alkanethiols etc.

- The effect of aging needs to be clarified by systematically studying it over longer periods of time.

- The model needs to be modified to include a larger set of reverse micellar species and mixing effects in order to predict the observed threshold behavior.

APPENDIX

A1 LIGHT SCATTERING

When a laser beam impinges on a particle, the electromagnetic field of the light beam interacts with the electrons within the particle and induces an oscillating polarization of electrons (an oscillating dipole) as shown in the figure A1.1. This oscillating dipole acts as a secondary source of light and radiates light in all directions, which is referred to as scattered light. If the majority of the light scattered by the particle is emitted at the same frequency as the incident light, then it is referred to as elastic light scattering[1].

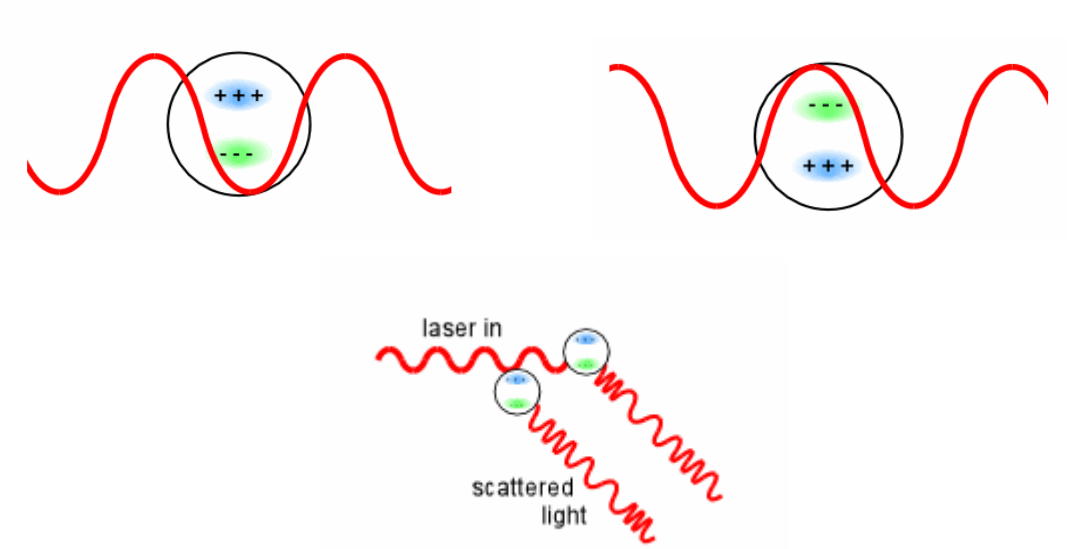

Figure A1.1: Schematic representation of induced fluctuating dipole and light scattering [2].

The theory of scattered light can be classified into Rayleigh scattering theory and Mie scattering theory. Rayleigh scattering theory applies to very small (defined below) and non-absorbing spherical particles, whereas Mie scattering theory is applicable to both absorbing and non-absorbing spherical particles with no restriction on particle size. In general Rayleigh scattering theory, if applicable, is preferred to Mie theory as the latter theory is complex. Rayleigh scattering theory is applicable only when $\alpha << 1$.

where,

$$\alpha = \frac{(2\pi a m_o)}{\lambda_o} \qquad \text{A1.1}$$

m_o → refractive index of the surrounding medium

a → the particle radius

λ_o → the wavelength of the incident beam in vacuum

According to Rayleigh scattering theory the scattered light intensity is related to particle size by the following relation [3]

$$I = I_o \frac{\left(1+\cos^2\theta\right)}{2R^2}\left(\frac{2\pi}{\lambda}\right)^4\left(\frac{n^2-1}{n^2+2}\right)^2\left(\frac{d}{2}\right)^6 \qquad \text{A1.2}$$

where,

n → refractive index of the particle

θ → scattering angle

λ → wavelength of the incident beam

d → diameter of the particle

I → scattered light intensity

I_o → intensity of the incident light beam.

R → distance from the particle to the detector.

A2 BROWNIAN MOTION AND STOKES-EINSTEIN EQUATION

Brownian motion is irregular and random motion of extremely small particles (micro/nano scale). Brownian path is the path followed by the particle in response to a random force. Equipartition theorem states that the energy associated with each degree of freedom of a particle is [4]

$$\left(\frac{1}{2}\right)k_B T = \left(\frac{1}{2}\right)(m\left\langle v_x{}^2 \right\rangle) = \left(\frac{1}{2}\right)(m\left\langle v_y^2 \right\rangle) = \left(\frac{1}{2}\right)(m\left\langle v_z^2 \right\rangle) \qquad \text{A2.1}$$

where, V_i → i^{th} component of velocity

k_B → Boltzman constant

T → Absolute temperature

The force (F_v), necessary to maintain a sphere with radius 'a' moving through a viscous liquid at a constant velocity is given by Stokes equation as [4],

$$F_v = 6\pi a\mu v \qquad \text{A2.2}$$

where, μ is viscosity of the fluid

v is the velocity of the particle in the fluid

The equation of motion for a particle can be written as(x-component),

$$m\frac{d^2x}{dt^2} = F_x(t) - 6\pi a\mu\frac{dx}{dt} \qquad \text{A2.3}$$

where, $F_x(t)$ → x component of random force

t → time

m → mass of the particle

The above force balance can be converted into an energy balance equation by multiplying the equation with x and averaging.

$$m < x\frac{d^2x}{dt^2} >=< xF_x(t) > -6\pi a\mu < x\frac{dx}{dt} > \quad \text{A2.4}$$

In the above equation, the first term on the right hand side reduces to zero because there is no correlation between x and $F_x(t)$. The left hand side term can be rewritten as,

$$m < x\frac{d^2x}{dt^2} >= m\left(\frac{d}{dt} < x\frac{dx}{dt} > - < (\frac{dx}{dt})^2 >\right) \quad \text{A2.5}$$

In the above equation, the first term on right hand side can be written as,

$$m\left(\frac{d}{dt} < x\frac{dx}{dt} >\right) = \left(\tfrac{m}{2}\right)\left(\frac{d}{dt}(\frac{d}{dt} < x^2 >)\right) = \frac{d}{dt}\left(\left(\frac{m}{2}\right)\frac{d}{dt} < x^2 >\right) \quad \text{A2.6}$$

By the definition of diffusion coefficient[5],

$$< x^2 >= 2Dt \quad \text{A2.7}$$

Then, equations A2.6 & A2.7 simplified to,

$$m\left(\frac{d}{dt} < x\frac{dx}{dt} >\right) = \frac{d}{dt}(mD) = 0 \quad \text{A2.8}$$

From equations A2.4, A2.5, and A2.8,

$$m < (\frac{dx}{dt})^2 >= 3\pi a\mu(\frac{d}{dt} < x^2 >) \quad \text{A2.9}$$

By combining equations A2.1 and A2.9, it can be shown that,

$$k_B T = 6\pi a\mu D \quad \text{A2.10}$$

This is the famous Stokes – Einstein equation, which relates the hydrodynamic radius of the particle to diffusion coefficient.

A3 DLS – ALIGNMENT PROCEDURE

Before any DLS measurement, the alignment of the instrument needs to be checked. There are several factors that effects the alignment namely, stability of the laser, stability of the detector electronics, mechanical alignment of all the hardware components, cleanliness of vat liquid, cleanliness of vat surface, scratches on vat surface, and laboratory power fluctuations. DLS instrument (Brookhaven, BI-200 SM, with BI-9000 AT digital correlator) has inbuilt software to check for the alignment. This test consists of two parts namely, stability test and alignment test.

A3.1 Stability test

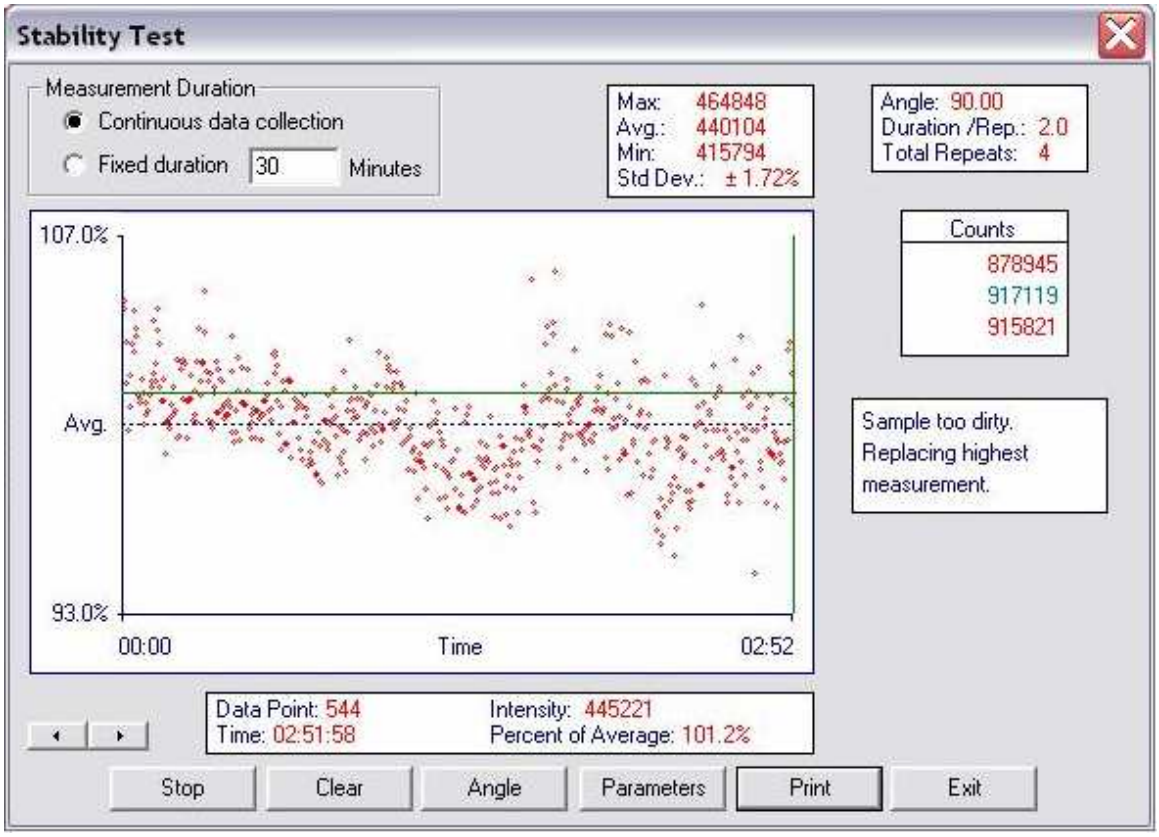

Figure A3.1: A typical snapshot showing a stability test of the laser in progress (from Brookhaven DLS instrument alignment software).

The objective of this test is to check for the stability of the instrument which includes the stability of the laser, stability of detector electronics, laboratory power

fluctuations, cleanliness of vat liquid and vat surface etc. This test is typically done at a scattering angle of 90^{o} but this is not mandatory. In this test, first the photon count must be adjusted to 100,000 and the statistical repeatability should be approximately ±0.32 % [6]. This test can be done for a fixed duration of 30 minutes or in the continuous data collection mode. This test also serves as a warm up for the laser. A typical stability test result is shown in the figure A3.1 From the figure it is clear that this stability test was run for about 3 hours, and the average signal strength is about 4,44,000 counts per second, and the standard deviation of the signal strength is 1.72 %.

A3.2 Alignment test

This test is to ensure that all the hardware components are properly aligned and this too depends on the cleanliness of the vat liquid and vat surface. As a first step, the number of dark counts (number of photons registered at the detector when the laser is off) is to be measured and entered as a parameter in the experimental parameters window. The snap shot of experimental parameters and sample parameters is shown in the figure A3.2.

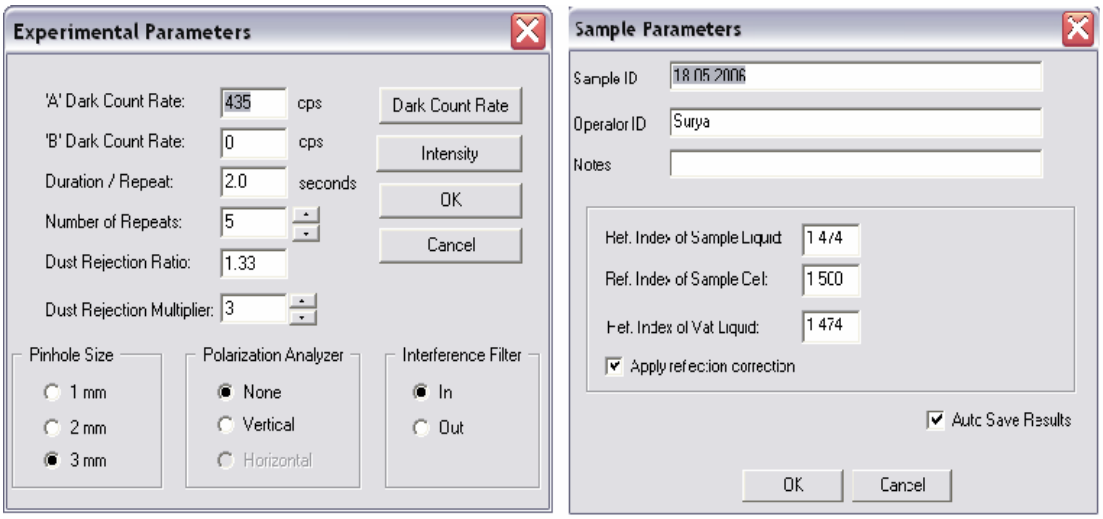

Figure A3.2: A typical snapshot of the parameters window for alignment check from Brookhaven DLS instrument alignment software

During this test, sample cell should not be in the path of the laser. Decalin is the vat liquid and the decalin molecules act as Rayleigh scatterers and scatter light equally in all directions. But, when the detector is placed at different scattering angles, the sampling volume, under observation by the detector, changes with the scattering angle. The correction factor for the different sampling volumes at different scattering angles is sinθ. Hence, I_θ Sinθ must be constant at all scattering angles. A constant I_θ Sinθ at all scattering angles indicates that the instrument is aligned properly in all aspects[6]. The error percentage at each scattering angle is calculated as,

$$Error\% = \left[\frac{I_\theta Sin\theta}{\langle I_\theta Sin\theta \rangle} - 1\right] \times 100 \qquad \text{A.2.4.1}$$

When this error percent is less than 1%, it is treated as excellent alignment and if it is less than 2%, it is treated very good alignment. A typical alignment result is shown in figure A3.3.

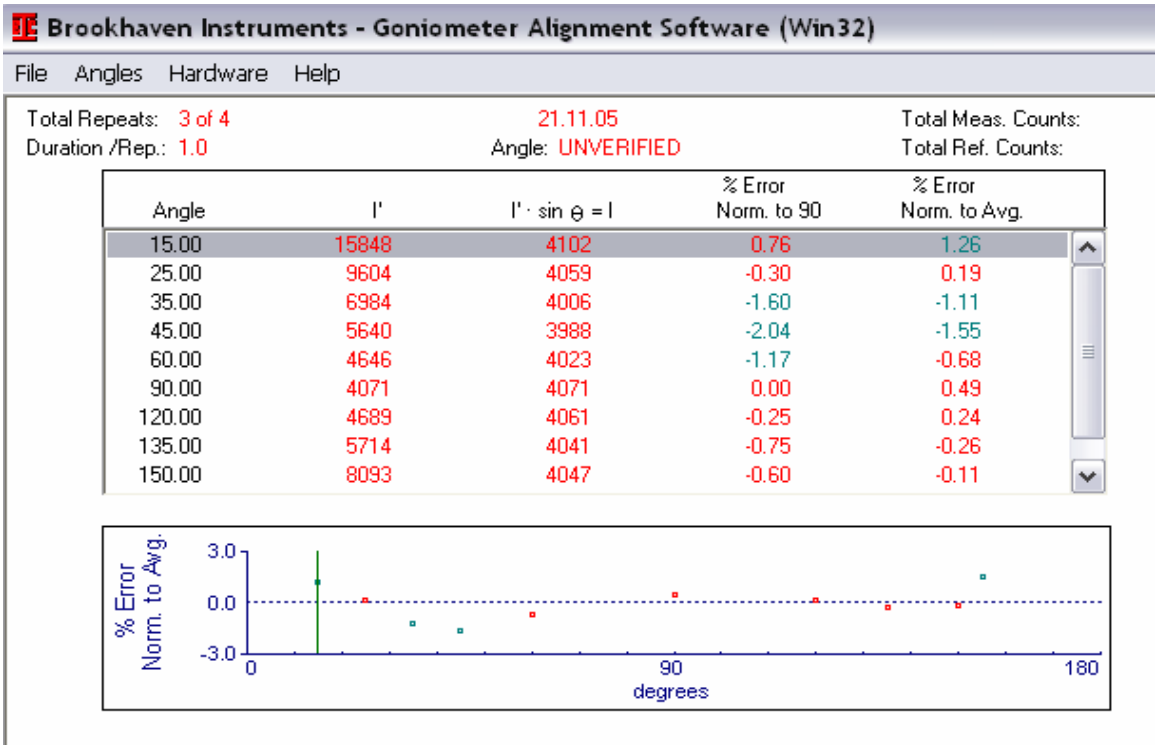

Figure A3.3: An example snapshot of alignment result from Brookhaven DLS instrument alignment software.

A4 OPERATING INSTRUCTIONS FOR DLS

Before operating the DLS instrument, it is important to know about the main components of DLS and their functionality. Careful and accurate operation is needed to get reliable measurements.

The main components are

1. Laser (He/Ne gas laser): It produces a monochromatic, coherent laser beam. Maximum power is 35 mW.
2. Neutral Density filter (ND Filter): It is used to vary the power of the laser beam Power specifications are displayed on the filter set.
3. Steering lens assembly: To focus the beam onto the center of the sample cell.
4. Sample cell assembly: To keep the sample of interest in the path of the Laser beam..
5. Eye-piece: To adjust the beam and to ensure that the beam is traveling towards the detector. If one is able to see the beam through the eyepiece it means that the beam is not reaching the detector, then he/she needs to adjust the eye-piece wheel such that the beam reaches the detector.
6. Pinhole wheel: To change the aperture size through which scattered light travels to the detector.
7. Filter wheel: To only allow beams of desired wavelength to reach the detector and reduce the effects of stray light.
8. Detector optics: To observe the scattered light intensity variations with time and to transfer this information to digital auto-correlator or computer.
9. Digital Auto-correlator: This fits an autocorrelating function and delivers the required information to DLS software for further analysis.
10. DLS software: It manipulates the data received from the auto-correlator to give desired information such as mean particle size, polydispersity etc.

The operating section is mainly divided into four parts, namely

1. Stability check of the Laser
2. Alignment check of the instrument
3. Sample preparation
4. Measurement section

A4.1 Switching on the Instrument

1. Switch on the mains of laser power input and then switch on laser power switch on the first switch board.
2. There is one more laser power input key on a rectangular box which is just before the laser. Keep it in on-position
3. At the front part of the laser there is a laser shutter. Keep it closed until one really needs the beam.
4. Switch on second mains on the other switch board and switch on other power switches and make sure that detector optics, automatic motor, CPU and Monitor all receive power. Switch on the A/C unit also.
5. Then, switch on the Detector power switch present on a small box just before the detector.

This completes the switching on procedure.

A4.2 Stability check of the Laser

Before going to the alignment check one has to ensure the stability of the instrument, i.e.. stability of the laser, stability of detector electronics, laboratory power fluctuations and unsecured arrangement of mechanical parts (If they move with time, it will be a big problem, movement in the sense even very small perturbation in position of mechanical parts is sufficient to obtain bad results). For the laser to deliver a stable beam it needs a minimum warming up period of 30 minutes.

1. Switch on the CPU and System monitor
2. Go to alignment software

3. Go to Hardware → Stability test (one can make it at any desired angle but suggested angle is 90°.)
4. One can use either continuous data collection or fixed duration (one can fix this duration by entering a number). If one uses continuous data collection he/she needs to stop the test whenever he/she desires so. If one selects fixed duration it will automatically stop after the given duration.

Note

1. The statistical repeatability in the count rate must be within ±0.32%
2. Otherwise one needs to work on the stability of the instrument
3. If the stability test provides a satisfactory result then one can go for alignment check of the instrument.

A4.3 Alignment check

1. Go to **Alignment software**
2. Click on **Clear** to clear the already existing data
3. Set detector angle to either 0 or 155 by clicking on **Set Detector Angle. Ensure that the detector arm and cables are free to rotate without any hindrances (books etc)**
4. Go to **Experimental Parameters,** set duration time and total number of repeats
5. Make sure that there are no dirt particles on the surface of the vat. Only use high quality lens tissue paper to swipe the surface. Care must be taken not to rub the surface directly as this may produce scratches by trapping dirt particles between the fingers and the vat surface.
6. Make sure that vat liquid is free of dirt particles and that the decanal (vat liquid) filtration system is switched off during alignment check
7. Set the aperture size to some desired value (say 2mm).
8. Set the laser filter to 633 nm by adjusting the filter wheel present besides the lens and slit assembly just before the detector.
9. Then click on **Start.**

10. Wait until it finishes alignment check at all angles.
11. In the alignment results Isinθ must be constant at all scattering angles. If the deviation is less than 2% then it means that the instrument is well aligned. If it is less than 1% , it means an excellent alignment.

A4.4 Sample preparation

Good sample preparation is an art, needs much patience, practice and intelligence. It is divided into three parts namely solvent purification, cell cleaning, and suspension preparation. The most commonly used solvent is DI water.

A4.4.1 Water purification

1. Distill the water to deionize the water and to remove trace impurities (multiple distillation is required)
2. Filter the distilled water with special water filtration system, with 0.2 micron filters (multiple filtration is required)
3. Filter this water again with sample filtration unit and maintain a best quality water reservoir (To filter very small quantities one can use syringe)
4. For other organic solvents, If the material of filter is compatible with the solvent one can follow the same procedure.

Note: Do not store the distilled water for a long period as Bacteria can easily grow and produces scattered light when it is exposed to the laser beam. Try to prepare fresh solutions daily. Presently, we have a Millipore system that provides clean DI water on demand.

A4.4.2 Cell cleaning

1. Clean the cells with tap water using liquid soaps (or detergents). Do not use any abrasive material. Care must be taken to ensure that there are no scratches on the sample cell. (Scratches and finger prints will produce

additional scattering and seriously affect the results). Wash it thoroughly to remove all the surfactant molecules

2. Clean these cells again with distilled & filtered water thoroughly.
3. Rinse these cells with best quality distilled water prepared as described in the previous section.
4. While drying the cells arrange them in such a way (i.e hang them upside down) that dust particles cannot get inside.
5. If any biological or other similar materials are adsorbed on the surface, to remove them, cells should be cleaned with concentrated sulfuric acid by placing them in a sonicating bath of sulfuric acid for 1 hr and then above mentioned steps 1 to 4 ought to be followed.

A4.4.3 Suspension preparation

Before going to prepare suspensions, it is very important to have all the required apparatus duly cleaned with purified and filtered solvent. The apparatus consists of sample cells, cell caps, diluting bottles, syringes and other useful glassware. Try to avoid long contact with air as the dirt particles can easily get transferred from air into liquid. Violent shaking of the sample produces small air bubbles which scatters light better than the particles of interest, so it is to be avoided.

Preparing a latex suspension

1. Prepare 200 ml of 10 mM KCl solution
2. Filter this solution with sample filtration unit repeatedly
3. Rinse the sample cell with this solution and after that close it with a clean cap
4. Take 4 drops of latex particles in 20 ml of prepared KCl solution and mix gently.
5. Then transfer this sample into sample cell through sample filtration unit(Repetitive filtration gives good results)

6. Then wipe the surface of the sample cell very gently with lens cleaning tissue paper (we can use methanol with the lens cleaning tissue for effective removal of dirt particles from the surface). Again do not rub directly, just wipe with the lens tissue.

A4.5 Measurement section

1. Insert the prepared sample inside the sample cell assembly.
2. Run the Decanal filtration unit for at least 10 minutes to remove dirt particles from the surface of the sample cell and also to remove the dirt particles from vat liquid by filtration. Wait for a while to allow the turbulence inside vat liquid to settle..
3. Open the laser door and switch on the detector optics
4. Observe the laser beam inside the sample cell. If the beam is very weak, then concentrate the sample. If it is fuzzy and thick, dilute the sample. If it gives random bursts, then filter the sample again to remove dirt.
5. Go to **DLS Software**
6. Go to **Motor → Set Detector Angle**
7. Enter the current angle and the destination angle(90° gives the best results)
8. Go to **Correlating functions** and click on **correlator control window**
9. In the **correlator control window** go to **Display** and select the items that you want to display on **correlator control window**.
10. Go to **Parameters** and set the parameters like temperature, refractive index of particles and solvent; operator ID and sample ID, measuring angle, dirt cut off option, viscosity, solvent type etc.
11. Go to **Duration** and set the time period of measurement.
12. Click on **Clear** to clear the existing data, if any.
13. Go to **Graphs** and open **Correlating function** and **Count Rate History.** Snap shots of correlating function and count rate history are shown in figures A4.1 and A4.2 respectively
14. Go to **ISDA** and open either **NNLS** or **CONTIN** to view the particle size distribution

15. Go to **Window** and click on **Smart tile** to view all the windows simultaneously on the screen.
16. Now click on green **Start** button to start the measurement and wait until it finishes.
17. Now one can watch a decaying correlating function in figure A4.1, particle size distribution in figure A4.3, count rate history in figure A4.2, mean particle size and polydispersity on the results window as shown in the figure A4.4..

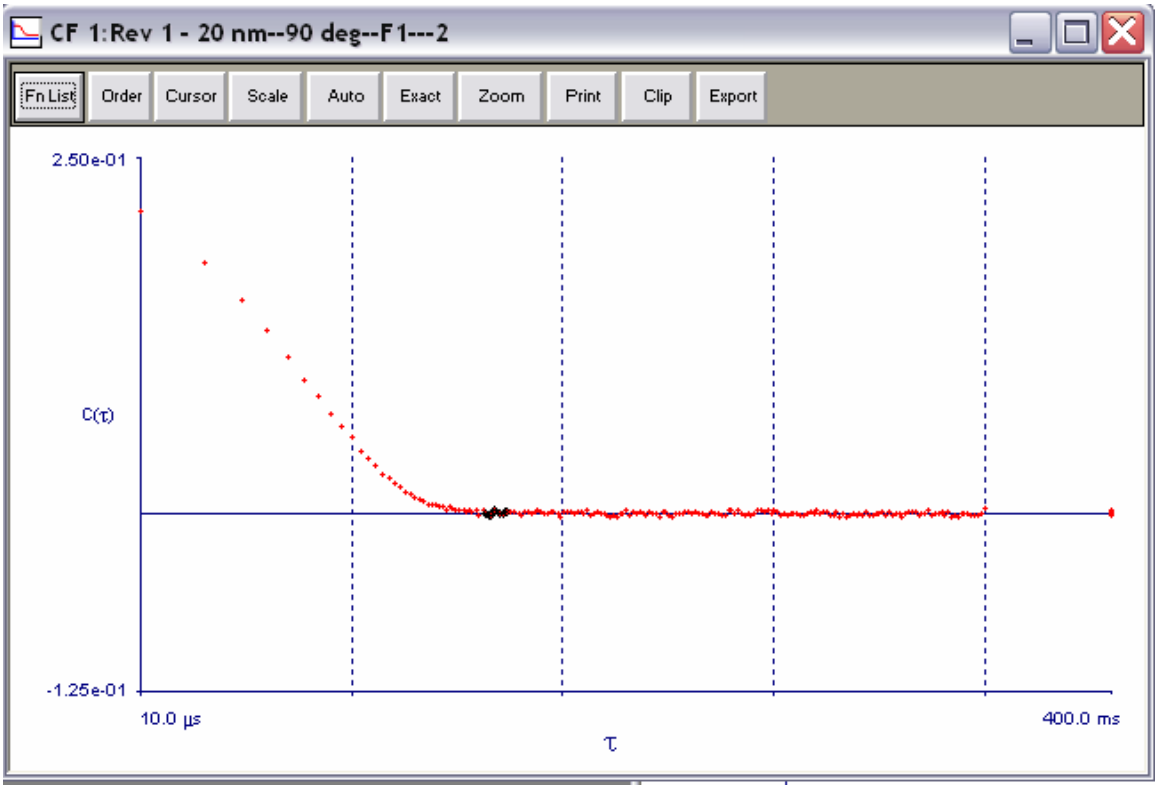

Figure A4.1: Snapshot of decaying second order auto-correlating function from Brookhaven DLS instrument operational software.

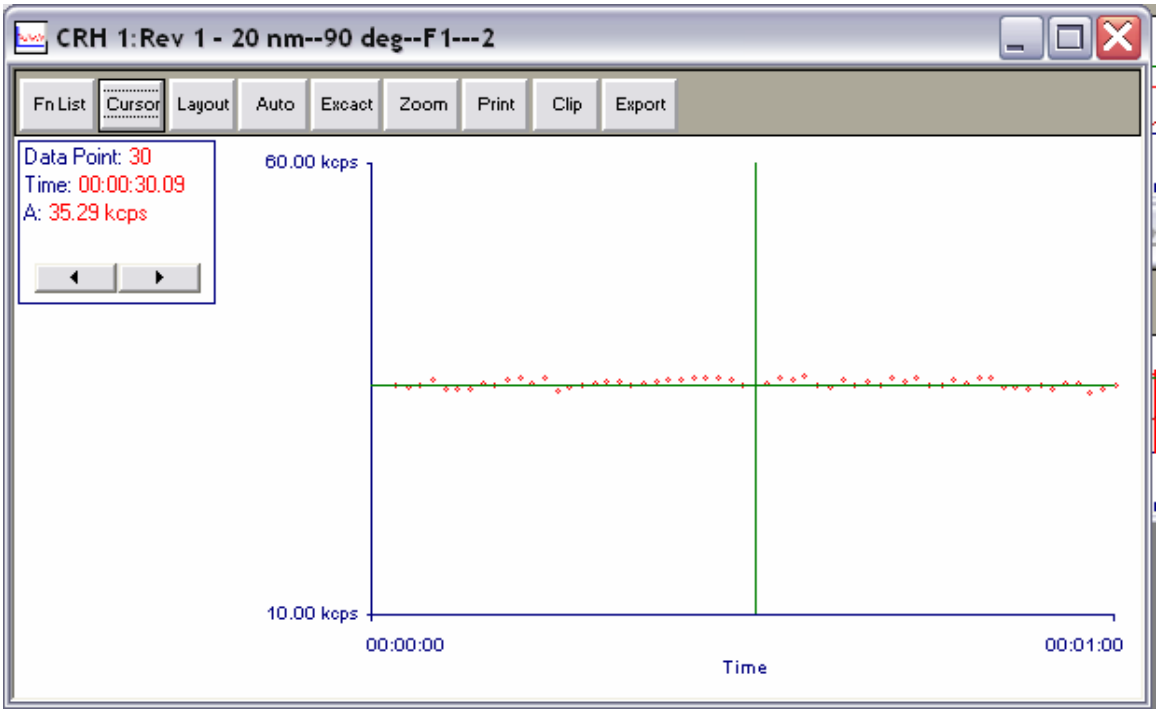

Figure A4.2: Snapshot of count rate history from Brookhaven DLS instrument operational software.

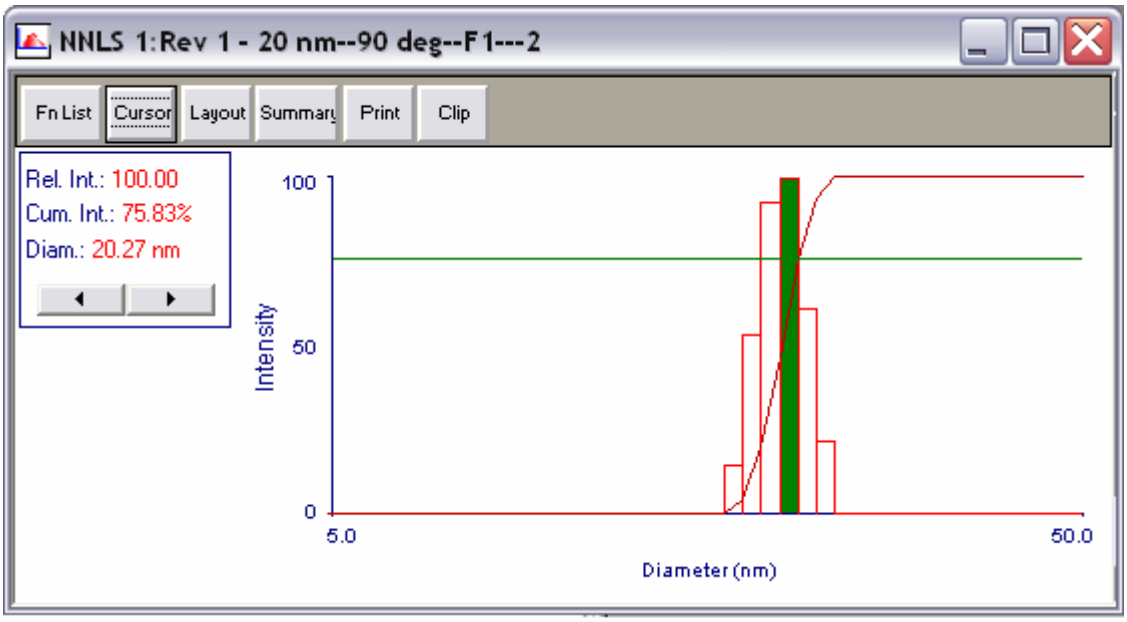

Figure A4.3: Snapshot of particle size distribution from Brookhaven DLS instrument operational software.

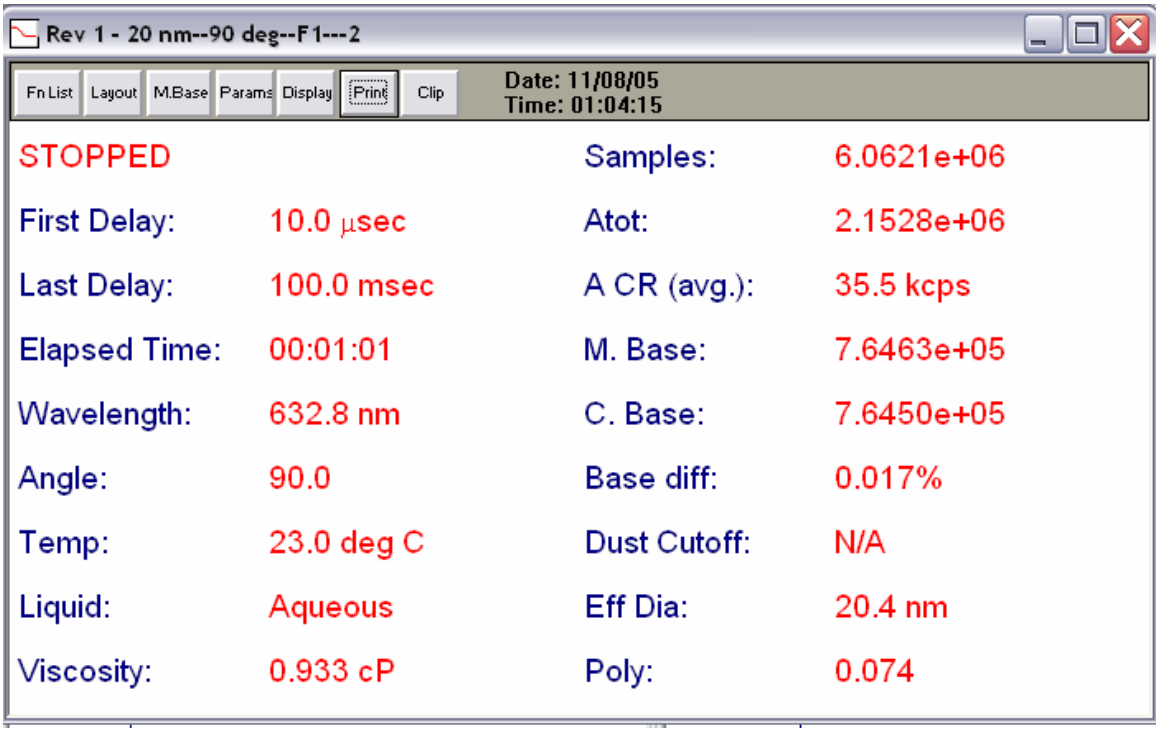

Figure A4.4: Snap shot of overall results window from Brookhaven DLS instrument operational software.

A5 SPECTRAL ANALYSIS – FREQUENCY BROADENED DISTRIBUTION

In dynamic light scattering experiments, the dynamical information about the system can be studied by observing the frequency broadened spectrum of the scattered light [7]. The idea behind this spectrum analysis is explained in detail in a review article on DLS by Finsy [7]. The fundamental idea behind this concept is based on Doppler shift. When a source of light (or sound) is moving towards the observer, the observer experiences a higher frequency than the natural frequency of the source which is called a blue Doppler shift. If the source is going away from the observer, red shift occurs(lower frequency or higher wavelength). This frequency depends on both the scattering wave vector and velocity of the particle as shown in equation A5.1.

$$\Delta\varpi = \bar{q}.\bar{v} \qquad \text{A5.1}$$

where,

$\Delta\omega$ = frequency shift,

$\bar{q}$ = scattering wave vector,

$\bar{v}$ = velocity vector of the particle.

When the system under observation consists of too many sources (particles) which are moving in all directions with respect to the observer, all the corresponding frequency shifts form a continuous Lorentzian spectrum as shown in the figure A5.1.

ω = frequency of the scattered light

$S(\omega)$ = weight for the magnitude of scattered light

The width of the spectrum at half of the maximum height is called line width, which is a characteristic constant that contains dynamical information about the system in it. This characteristic constant is related to the translational diffusion coefficient of the particles by the expression A5.2.

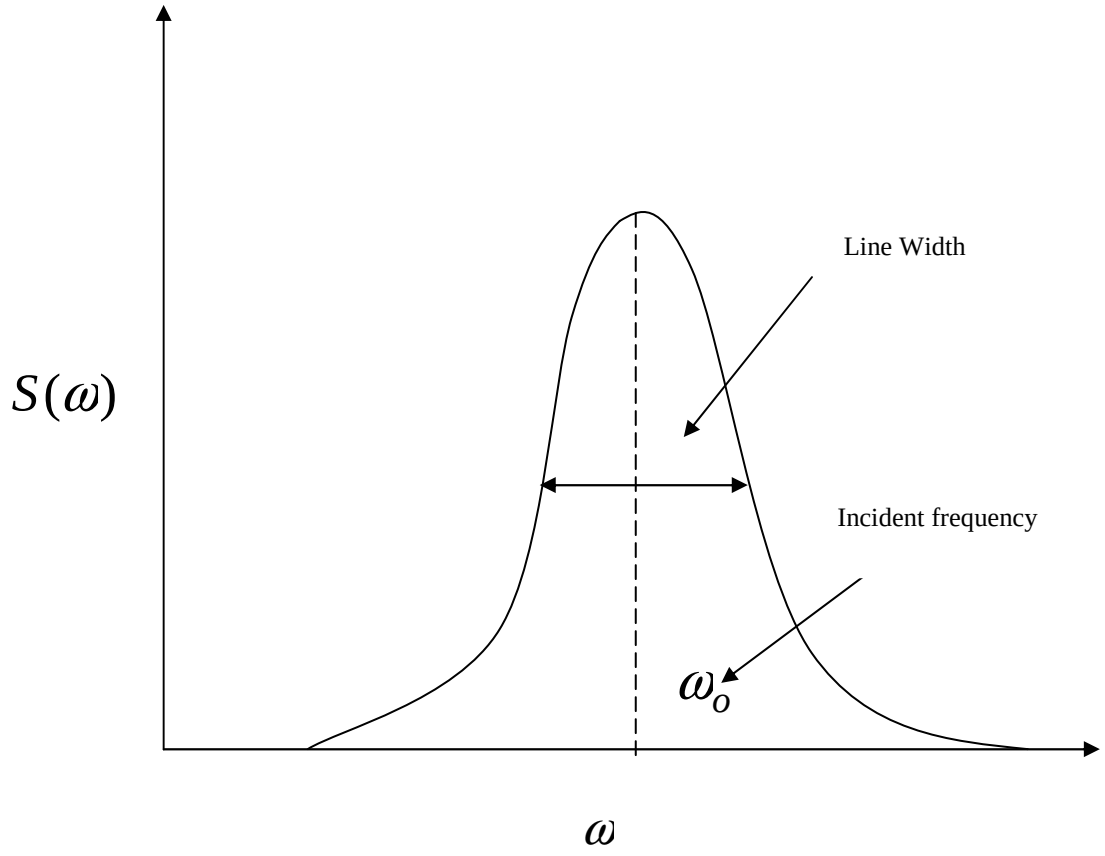

Figure A5.1: Frequency broadened distribution for scattered light[7]

$$\Gamma = D_T q^2 \qquad \text{A5.2}$$

From this translational diffusion coefficient, diameter of particles is calculated using Stokes-Einstein equation. This line width is equalent to the characteristic decay constant of the auto-correlating function calculated from temporal variation in the scattered light intensity. However the accuracy of spectrum analyzers is limited by the band width of the filters. To have high accuracy in frequency on the X – axis, the band width should be small which in turn results in a poor accuracy in the Y – axis value (signal strength) due to weak and noisy signal. Because of this reason, spectrum analyzers are replaced with digital auto-correlators in the modern dynamic light scattering instruments [7].

A6 AFM IMAGES – STANDARD PRACTICE SAMPLES

Some standard samples are imaged with contact mode Atomic Force Microscope. Those images are presented here. The figure A6.1 shows the topography of plain sheet of muscovite mica. From the roughness profile, it is seen that the peak to peak roughness is around 0.7 nm. The figure A6.2 shows the 3D version of same muscovite mica image.

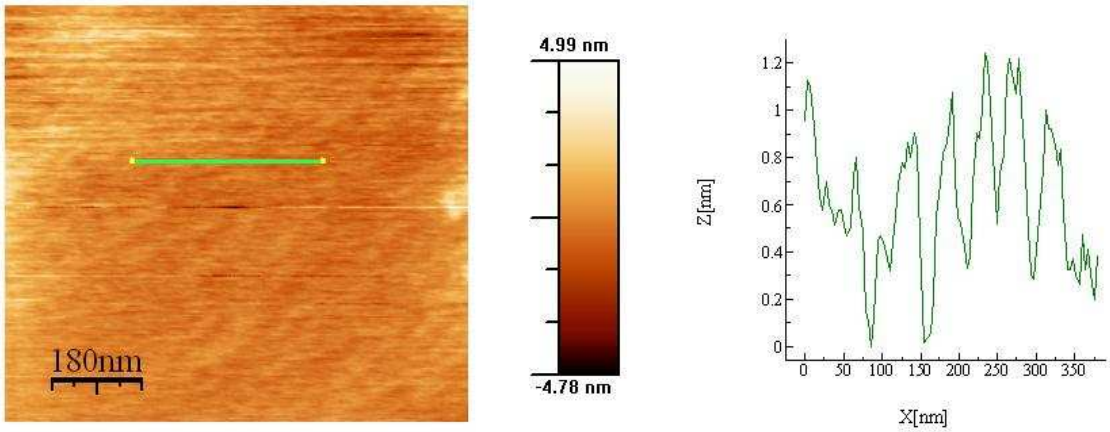

Figure A6.1: Topography of plain muscovite mica with roughness profile.

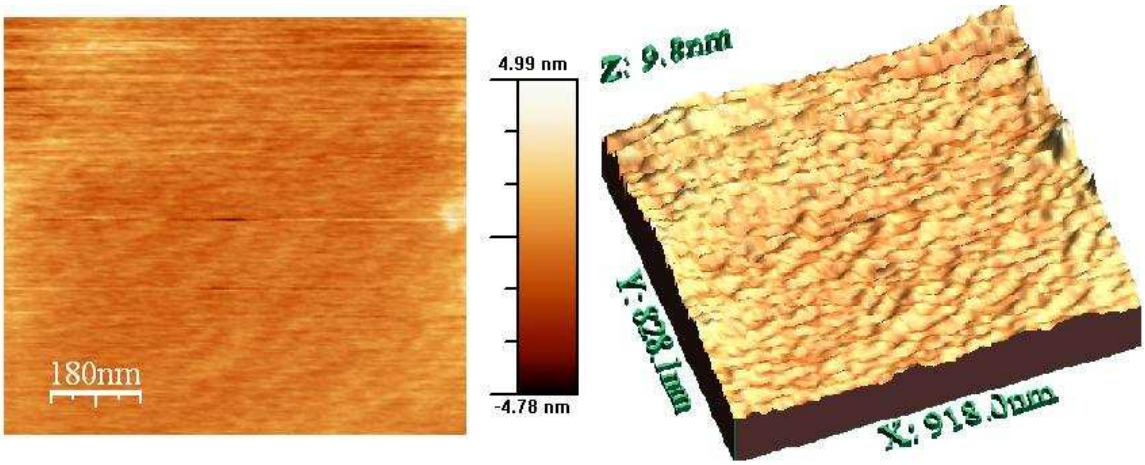

Figure A6.2: Topography of plain muscovite mica and 3D version of the topography.

Figure A6.3 shows the image of 100 micron scanner standard sample. The 2D and 3D topography are presented in this image. The surface profiles corresponding to the lines drawn on the 2D topography image of figure A6.3 are presented in figure A6.4. From the first surface profile it can be concluded that the side of the grid is 5 micro meters. From the second surface profile, it can be concluded that the width of the wall is 3 micro meters and that the height of the grid is 80 nm.

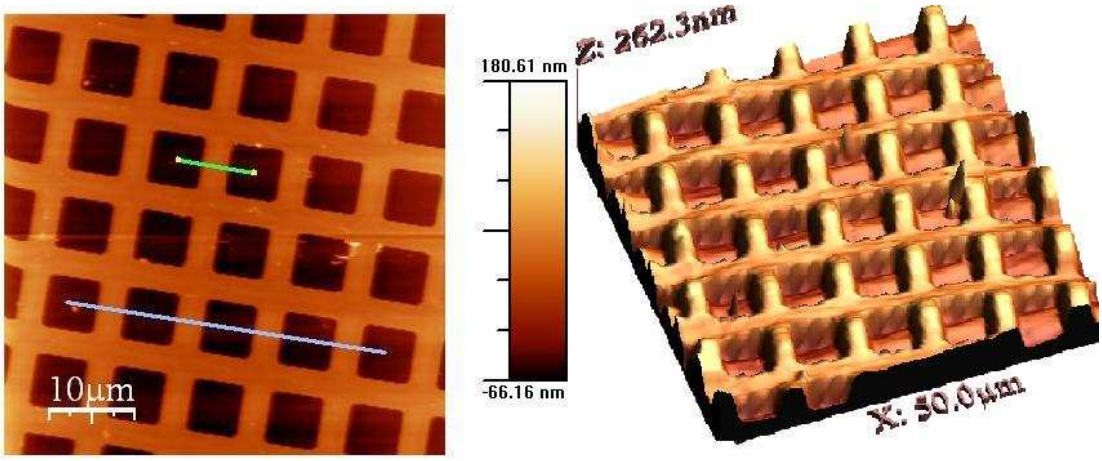

Figure A6.3: Topography of 100 micron scanner standard sample, 2D and 3D versions

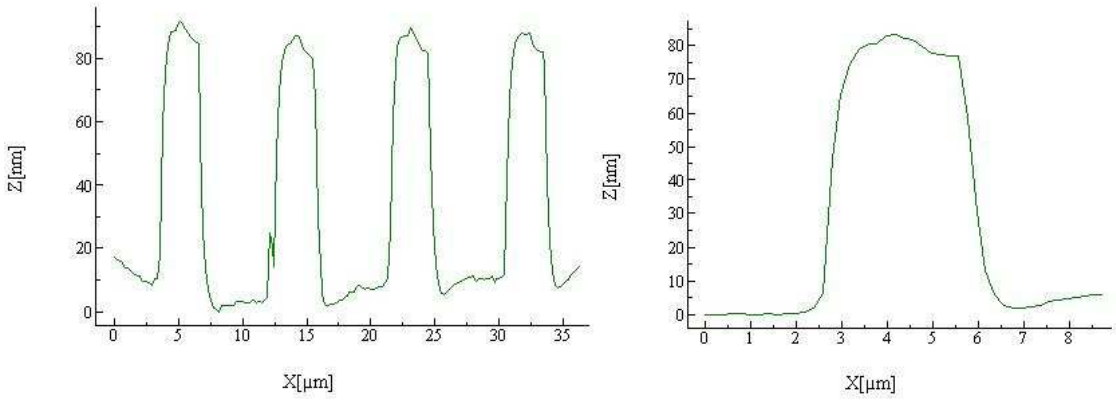

Figure A6.4: The two surface profiles corresponding to the bars shown in figure A6.3.

The AFM image of a 5 micron scanner standard sample is presented in the figure A6.5. The surface profile of the same sample for line drawn in figure A6.5 is shown

in figure A6.6. From figure A6.6, it can be concluded that the height of the first pea is 350 nm and the spacing between two peaks (peak to peak distance) is about 1.1 micrometers (first peak is at 0.6 micro meters and the second one is at 1.7 micro meters.).

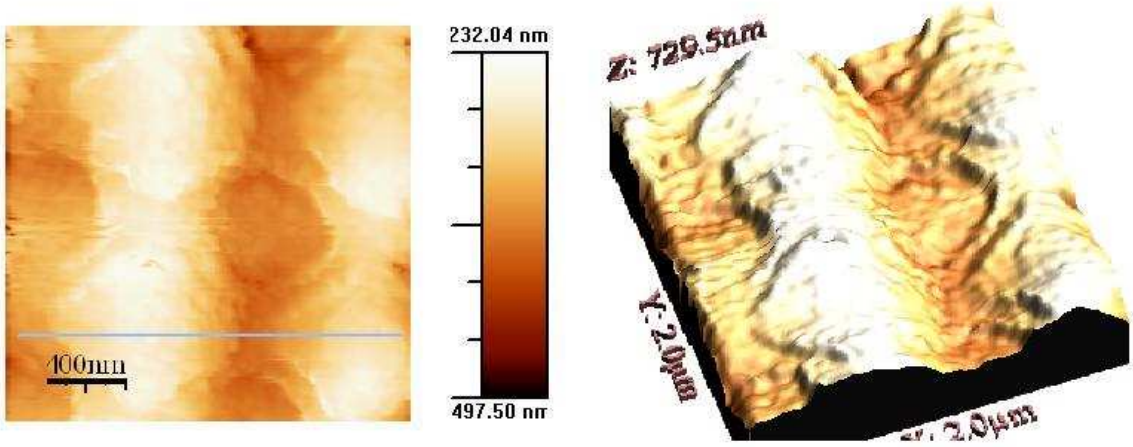

Figure A6.5: Topography of 5 micron scanner standard sample, 2D and 3D versions

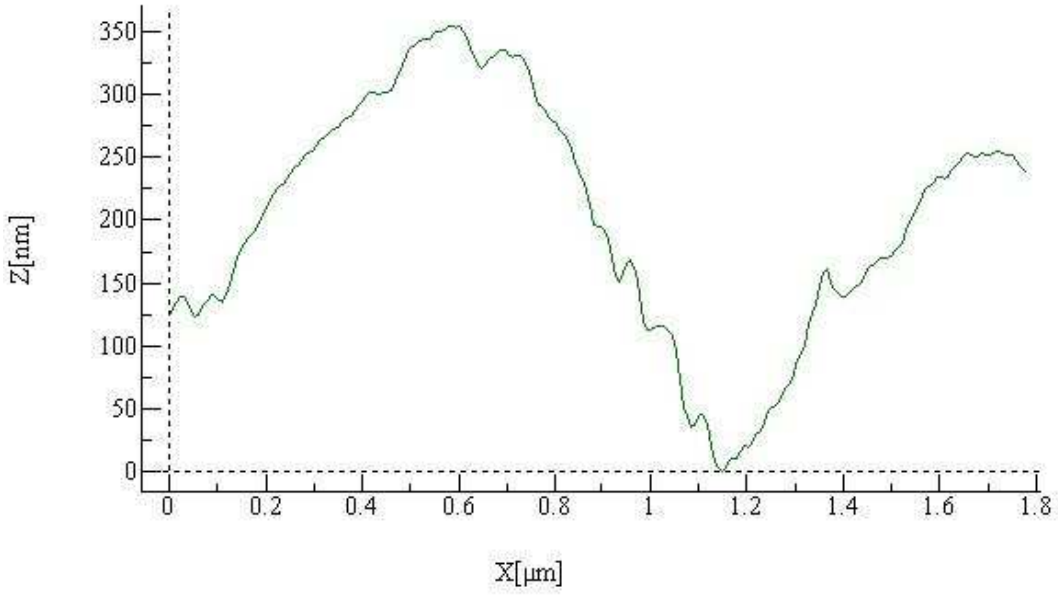

Figure A6.6: The surface profile corresponding to the bar shown in the figure A6.5.

Several attempts are made to characterize the nanoparticles with the help of AFM. Though they are not successful in obtaining a mean particle size from the image, the

topography of a few samples is presented. Samples of gold nanoparticles are prepared on plain silicon wafer and imaged

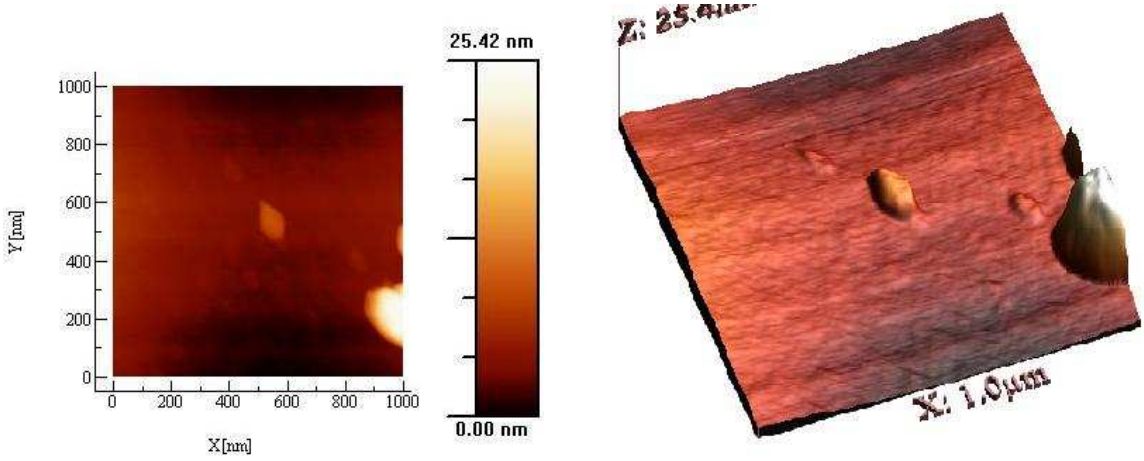

Figure A6.7: AFM images of chemically modified flat silicon substrate.

with contact mode AFM. The images could not show the presence of particles. The reason may be sliding of the particles when forced with AFM tip due to weak binding ability of these particles to the substrate. To enhance the binding ability between the particles and silicon substrate, silicon substrate is chemically modified by forming a layer

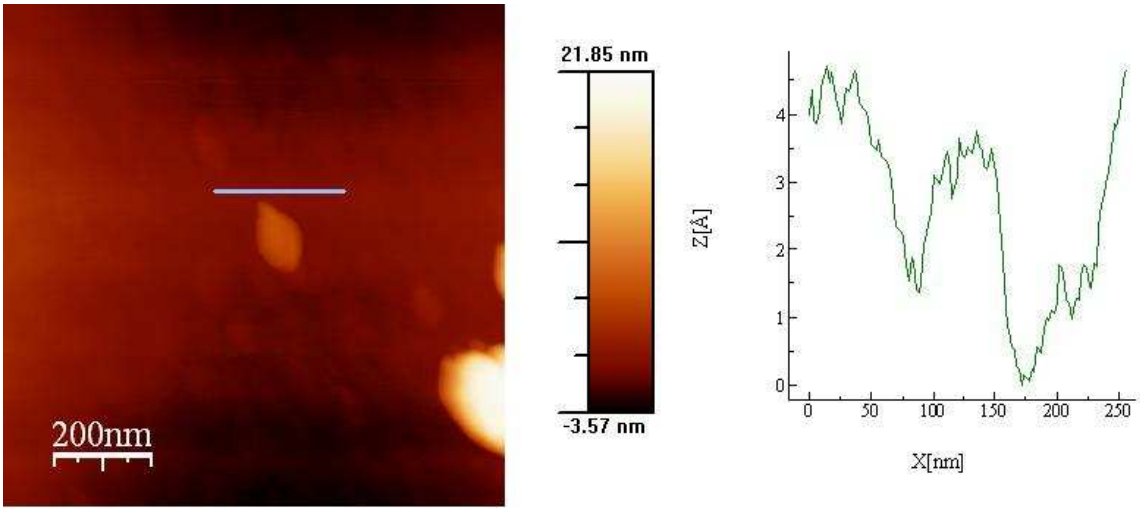

Figure A6.8: This figure shows the roughness profile of chemically modified silicon wafer.

of APTMS molecules on it. These molecules consists of two ends, one of which forms a bond with the substrate and the other forms a bond with gold nanoparticles. Samples are prepared with chemically modified silicon wafer by inserting them in to the solution of gold nanoparticles of interest. Before imaging the particles, chemically modified plain silicon wafer is imaged with non contact mode AFM. These images are shown in the figure A6.7. The roughness profile on the silicon surface is shown in the figure A6.8. It is clear from the figure A6.8 that the average roughness is approximately 2.5 A^{o} and The silicon wafer with 6 nm standard sodium citrate stabilized gold nanoparticles is also imaged with non contact mode AFM. The image is shown in the figure A6.9. From the figure A6.9, it is clear that sample is more concentrated and consists two many particles on it in random fashion. The surface topographic profile of the 6 nm standard gold nanoparticles is shown in the figure A6.10. Finally, particle size could not be resolved from this image.

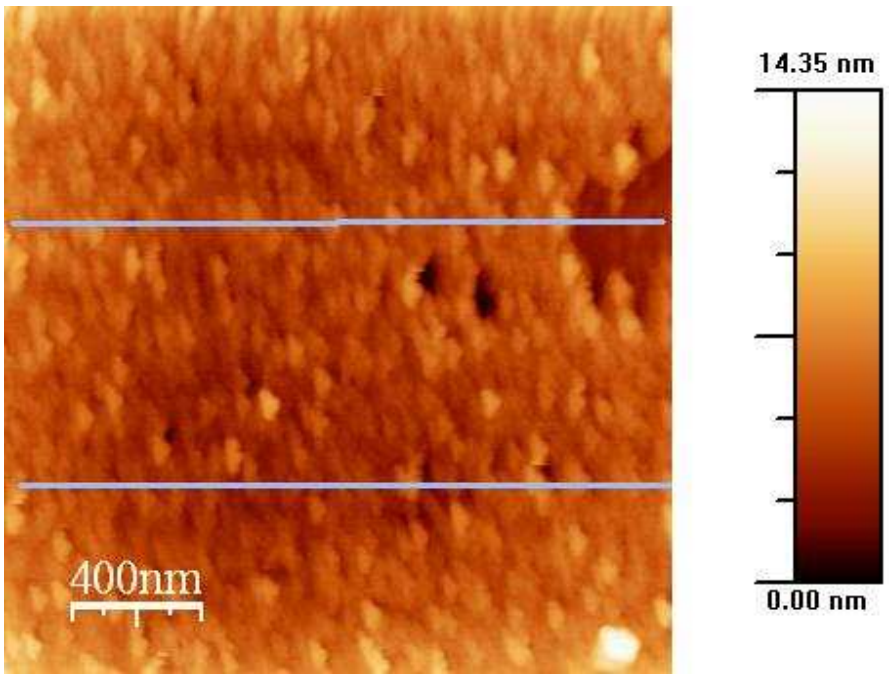

Figure A6.9: AFM image of 6 nm standard gold nanoparticles on chemically modified silicon wafer.

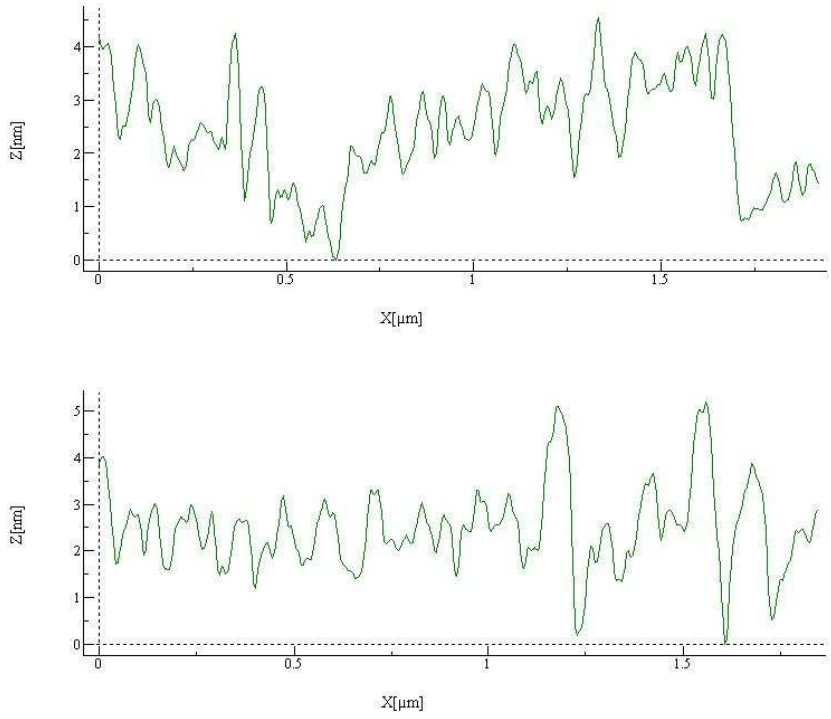

Figure A6.10: Surface topography of the 6nm standard gold nanoparticles on the chemically modified silicon wafer.

A7 CHEMICALS

A7.1 Hydrozen tetrachloroaurate (or) Chloroauric acid

Suppliers : Sigma – Aldrich (99.99%)
Cas Number : 27988 – 77 – 8
Product Number : 254169
Batch Number/Lot Number : 12002BE
(and)
Suppliers : Kemie Labs
Cas Number : 16903 – 35 – 8
Product Number : C2355
Batch Number/Lot Number : 030206

A7.2 Hydrazine hydrate(99%)

Suppliers : SD Fine Chemicals, India
Product Number : 38502
Batch Number/Lot Number : E05A – 1005 – 1404 – 13

A7.3 Sodium – AOT(99%)

Supplier : Sigma – Aldrich
Cas Number : 577 – 11 – 7
Product Number : D – 0885
Lot Number : 116H0067

A7.4 Brij 30

Supplier : Sigma – Aldrich
Cas Number : 9002 – 92 – 0
Product Number : P4391

Lot Number/Batch Number : 093K01091

A7.5 Iso-octane(HPLC)

Supplier : E. Merck (India) Ltd.
Cas Number : 540 – 84 - 1
Batch Number : RD2RF52055

Note :

1. Water for all the experiments is from Millipore Unit, Chemical engineering department, IISc.
2. 100 nm filters from Millipore and 200 nm filters from PAL German Labs are used for various purposes in synthesis and characterization.
3. Brookhaven BI – 200 SM DLS instrument is used for characterization.
4. Lab View interface to control stepper motor drive designed by Mr. Prakash(Project Assistant in Prof. Sanjeev K Gupta’s Lab) is used to inject the reducing agent fluid.

A8 DIGITAL PICTURES OF THE SAMPLES OF GOLD NANOPARTICLES

A8.1 Effect of Injection Time

Temperature : 27 ^{o}C, [AOT] = 0.1 M, [$C_{12}E_4$] = 0.2 M, [$HAuCl_4$] = 0.05 M
[N_2H_5OH] = 0.125 M, W_o = 8.
The aqueous solutions are aged for 17 days and reverse micellar solutions are aged for 2 days. Injection times are written in brackets down the image.

(direct addition ~ 1 S), (10 S), (20 S), (30 S), (45 S), (60 S), (80 S), (120 S)
Figure A8.1: The digital picture of gold nanoparticle samples synthesized at 27 ^{o}C.

Temperature : 30 ^{o}C, all the remaining parameters are same as above.

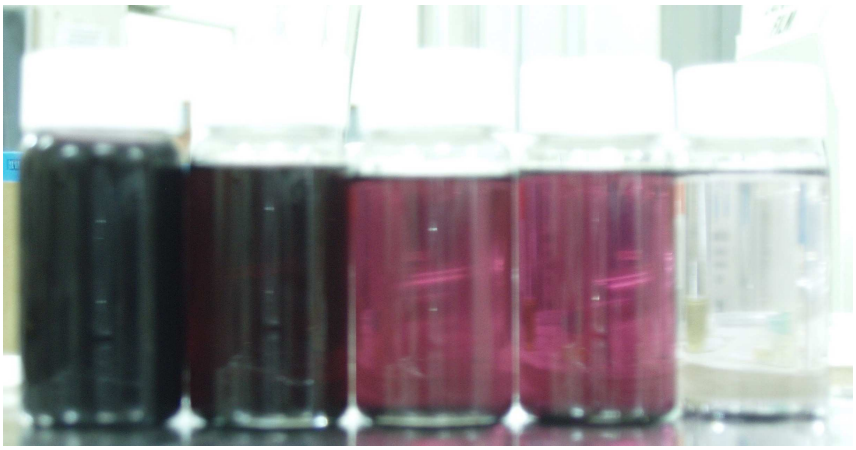

(direct addition ~ 1 S), (10 S), (20 S), (30 S), (45 S)
Figure A8.2: The digital picture of gold nanoparticle samples synthesized at 30 ^{o}C.

Temperature : 29 ^{o}C, [AOT] = 0.1 M, [$C_{12}E_4$] = 0.2 M, [$HAuCl_4$] = 0.05 M

[N_2H_5OH] = 0.125 M, W_o = 8.

The aqueous solutions are aged for 17 days and reverse micellar solutions are aged for 1 days.

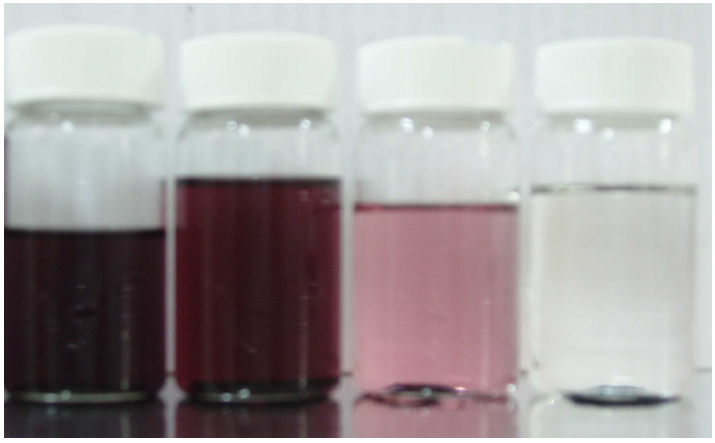

(direct addition ~ 1 S), (10 S), (20 S), (30 S)

Figure A8.3: The digital picture of gold nanoparticle samples synthesized at 29 ^{o}C.

A8.2 Effect of Temperature

[AOT] = 0.1 M, [$C_{12}E_4$] = 0.2 M, [$HAuCl_4$] = 0.05 M

[N_2H_5OH] = 0.125 M, W_o = 8.

The aqueous solutions are aged for 20 days and reverse micellar solutions are aged for 2 days. Injection times are written in brackets down the image.

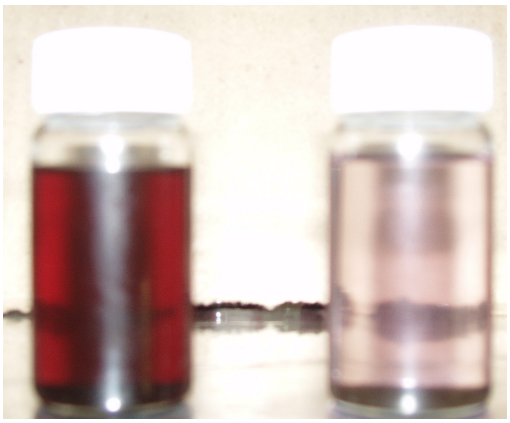

(Ice bath ~ 0^{o}C) (27^{o}C)

Figure A8.4: The digital picture of gold nanoparticle samples synthesized at 27 ^{o}C and 0 ^{o}C.

References

[1] Berne B J, Pecora R, “Dynamic Light Scattering”, Dover Publications (2000).

[2] URL: http://www.ic.sunysb.edu/Stu/zhang4/lightscattering.htm visited on 5.1.2006.

[3] URL: http://en.wikipedia.org/wiki/Rayleigh_scattering visited on 5.1.2006.

[4] Feynman, “Lectures on Physics Volume 1”.

[5] Light scattering by C Schroeder, Modern Physics Laboratory, Carnegie Mellon University.

[6] Bruce B W, “Operating instructions manual”, BI200SMMAN, Ver. 2.5(1993).

[7] Finsy R, “Particle sizing by quasi elastic light scattering”, Adv. in Colloid and Interfac. Sci., **52**, 79-143(1994).